2014-12-05

On the Use of Hybrid Compact Polarimetric SAR for Ship Detection

Atteia Allah, Ghada Emam Mohamed

UNIVERSITY OF CALGARY

On the Use of Hybrid Compact Polarimetric SAR for Ship Detection

by

Ghada Emam Mohamed Atteia Allah

A THESIS

SUBMITTED TO THE FACULTY OF GRADUATE STUDIES

IN PARTIAL FULFILLMENT OF THE REQUIREMENTS FOR

THE INTERDISCIPLINARY DEGREE OF DOCTOR OF PHILOSOPHY

GRADUATE PROGRAM IN GEOMATICS ENGINEERING

and

GRADUATE PROGRAM IN ELECTRICAL AND COMPUTER ENGINEERING

CALGARY, ALBERTA

December, 2014

Abstract

Maritime surveillance is an issue of particular interest and importance for countries bordering on the sea. Monitoring and controlling maritime activities are essential for these countries to assert their sovereignty over their waters. Ship detection is one of the most vital elements of maritime control. Traditional surveillance methods suffer from narrow coverage and high cost to achieve comprehensive surveillance. However, Synthetic Aperture Radar (SAR) with its ability to provide images covering wide geographic areas and acquired with a variety of imaging modes, polarization configurations, incidence angles and resolutions may be considered as a promising alternative/complement for existing methods. Quad-polarimetric SAR data has been used successfully for ship detection. However, narrow swath of quad-polarimetric SAR promotes the urgent need to explore ship detectors for dual-polarimetric systems. Compact polarimetric (CP) SAR has high potential of providing more information than linear dual-polarimetric SAR. Even wider swaths will be provided in many of the CP imaging modes of the upcoming Canadian Radarsat Constellation Mission (RCM) SAR to be launched in 2018.

In this thesis, the use of CP SAR for ship detection is explored. To fulfill this purpose, two novel contributions are introduced. The first is an investigation study of the possibility and benefits of using pseudo-quad data for improved ship detection. This is achieved by comparing the ship detection performance of dual-polarized CP and pseudo-quad data to linear and circular dual-polarized SAR. The pseudo-quad data is generated by a reconstruction algorithm that aims to reconstruct some elements of the quad-pol covariance matrix from CP data specifically for maritime applications. This study is applied on Radarsat-2 scenes with fine resolution and simulated medium and low resolution RCM data . The effect of spatial resolution, ship orientation and incidence angle on the detection performance has been explored.

The second contribution is a new hybrid ship detection algorithm that utilized CP Stokes parameters and some of their derived parameters for ship detection. The pre-screener of the algorithm merges three detection strategies to declare candidate ships and the discriminator uses a CP decomposition technique to discriminate ships from false alarms based on the type of scattering mechanism. The proposed detection algorithm is applied to a number of simulated RCM scenes with medium and low resolutions.

The findings of this thesis suggest the usefulness of CP reconstruction for improved ship detection. For the hybrid ship detection algorithm, a detection rate of 100% is obtained for medium resolution data and about 98% for low resolution data.

Acknowledgments

Dedication

To my beloved family

Hassan, Malak, and Zohair

Table of Contents

List of Tables

List of Figures and Illustrations

List of Symbols, Abbreviations and Nomenclature

Symbol	Definition
A^*	A conjugate
A^H	A Hermitian
A^T	A transpose
A^{-1}	A inverse
$\langle \rangle$	Spatial average
β_o	Beta-naught Radar Backscatter Coefficient
C	Frequency Band for a radar with 4-8 GHz frequency
C	Covariance matrix
Hz	Hertz
GHz	Gigahertz
L	Frequency Band for a radar with 1 to 2 GHz frequency
T	Threshold
t	CFAR detector design parameter
X	Scattering vector
$lship$	Minimum detectable ship length
ρ_{HH-VV}	Co-pol Correlation Coefficient
$\sigma ship$	Minimum detectable ship radar cross section
λ_B	Bragg wavelength
π	3.141516
ψ	Orientation angle
S_{ij}	Complex scattering coefficient

σ^o	Sigma-naught Radar Backscatter Coefficient
χ	Angle of ellipticity
θ	Incidence angle
m	Degree of Polarization
μ_o	Mean of ocean intensity data
μ_t	Mean of target intensity data
μ	Mean value
σ_o	Standard deviation of ocean intensity data
η	Threshold

Abbreviation	Definition
AIC	Akike Information Criteria
AIS	Automatic Identification System
ATD	Adaptive Thresholding Detection/ Detector
Acq. date	Acquisition date
Acq. time	Acquisition time
Adv.	Advantage
B	Beam
BIC	Bayesian Information Criteria
CA-CFAR	Cell Averaging Constant False Alarm Rate
bs	Bragg scattering
CCRS	Canada Centre for Remote Sensing

CFAR	Constant False Alarm Rate
CP	Compact Polarimetry
CPR	Circular Polarization Ratio
CTLR	Circularly polarized transmitted and linearly polarized received
CirP	Circularly polarized transmitted and circularly polarized received
cdf	Cumulative Density Function
DCP	Dual Circular Polarization
DCPL	Degree of Circular Polarization
DN	Digital Number
DODP	Degree of Depolarization
Dual-pol	Dual Polarization
4-D	Four dimensional
Dis.	Disadvantage
db	Double bounce scattering mechanism
G-GLRT	Gaussian Genaralized Likelihood Ratio Test
NLPOP	Number of Lowest PMD Orientation percentage
GMM	Gaussian Mixture Model
GMT	Greenwich Mean Time
EM	Expectation Maximization
ERS	European Remote Sensing
Eqn.	Equation
FQ	Fine Quad polarization beam type
H	Horizontal polarization
HH	Horizontally polarized transmitted and received

HV	Horizontally polarized transmitted and vertically polarized received
H.Pr	Highest performance
Km	Kilometer
Inc.Angle	Incidence Angle
JPL	Jet Propulsion Laboratory
LHS	Left hand side
LPR	Linear Polarization Ratio
LP	Linear polarization
LR	Likelihood Ratio
LRT	Likelihood Ratio Test
N.S.W	Nominal swath width
NWR	Normal Wind Region
ML	Multilook
PD	Probability of Detection
PFA	Probability of False Alarm
PG-GLRT	Polarimetric Gaussian Genaralized Likelihood Ratio Test
PMD	Probability of Missed Detection
PQ	Pseudo Quad
PQHH	Pseudo-quad horizontally polarized transmitted and received
PQHV	Pseudo-quad horizontally polarized transmitted and vertically polarized received
PQVV	Pseudo-quad vertically polarized transmitted and received

PWF	Polarimetric Whitening Filter
2P-CFAR	Two Parameter Constant False Alarm Rate
pdf	Probability Density Function
Quad-pol	Quadrature Polarization
RADAR	RAdio Detection And Ranging
RADARSAT	RADAR SATellite
RCM	Radarsat Constellation Mission
RCS	Radar Cross Section
RMSE	Root Mean Square Error
ROC	Receiver Operating Characteristic
RL	Right circularly polarized transmitted and left circularly polarized received
RHS	Right hand side
RR	Right circularly polarized transmitted and received
RS2	Radarsat-2
Res.	Resolution
SAR	Synthetic Aperture Radar
Sec.	Section
SIR-C	Spaceborne Imaging Radar-C band
SLC	Single Look Complex Product
SPOT	Systme Pour lObservation de la Terre
Sc. No	Scene number
Single-pol	Single Polarization
U of C	University of Calgary

V	Vertical polarization
VH	Vertically polarized transmitted and horizontally polarized received
VMS	Vessel Monitoring System
VDR	Verified Detection Rate
VV	Vertically polarized transmitted and received
vs	Volume scattering mechanism
W.S	Wind speed

Chapter 1

Introduction and Literature Review

It is well known [1, 2, 3] that the economical prosperity of countries overlooking the sea is intimately linked to the maritime activities taking place within their waters. These activities need to be secured against illegal fishing, pollution, piracy, and others [2, 3]. This is particularly important for countries with extended coastlines which may suffer from formidable challenge in their quest for maritime security [1]. Fields of maritime surveillance include: fishery control, pollution control, maritime traffic control and others. Fishing activities should be rigorously monitored because many illegal fishing ships find their ways through oceans far away from coast authorities [4]. Unfortunately, the change in earth climate due to global warming phenomenon has caused considerable volumes of sea ice in the Arctic waters to melt rapidly and many passages become completely opened giving better chance for such illegal ships to go through it away from governmental supervision [4]. Obviously, the situation will become worse as earth climate gets warmer since more Arctic passages will be accessible yielding the need of more effective control on maritime activities taking place at these passages. Moreover, a great threatening agent for oceanic creatures to be controlled is the pollution caused by oil spills from ships. A further important natural problem that should be detected and may cause a catastrophic crisis for ships traveling in near polar waters is icebergs. All these points and others promote the urgent demand for effective maritime surveillance methods.

One of the most vital elements of maritime control is ship detection. Maritime surveillance has relied on patrol boats and aircraft, shore-based radar and cameras. Other surveillance methods which are utilized specifically for monitoring ships are the Vessel Monitoring System (VMS) [5] and the Automatic Identification system (AIS) [6]. VMS is used in com-

mercial fishing to allow environmental and fisheries regulatory organizations to monitor the position, time at a position, course and speed of fishing vessels. The AIS is initially intended to help ships avoid collisions, as well as assisting port authorities to better control sea traffic. However, maritime surveillance with the aforementioned methods faces many challenges [7, 8]. The vast sea area to be monitored, the limitations of the available supervision tools and the high cost of a comprehensive surveillance are considered as major challenges. Furthermore, while the VMS and the AIS are clearly very effective ship control systems [7, 8], some ships which are active without carrying transponders or switching their transponders off cannot be guarded. Therefore, there has been recently growing interest in maritime surveillance in optical and Synthetic Aperture Radar (SAR) imagery as an alternative solution for the problems or as a complementary approach for the limitations of the existent surveillance methods [7, 8].

1.1 Ship Detection from Space

It has been shown in the literature that satellite optical and radar imaging can readily be used for maritime surveillance generally and ship detection specifically [8, 9, 10]. By considering optical imaging first, it has been relatively clear that high resolution optical sensors such as Quick-Bird, IKONOS and SPOT-5 are able to produce images that are detailed enough for ship detection. However, these high resolution sensors suffer from limited swath which makes them less suitable for wide area surveillance [8]; instead, they are suitable for classifying ships within a particular area of interest. Furthermore, optical imaging is affected by cloud covers, haze, fog and sun glint [8]. Optical images are also restricted to be captured at daytime. On the other hand, SAR images are considered more effective to monitor most maritime activities such as ships, oil slicks, natural discharges and icebergs [11, 12, 13]. Imaging with SAR is not restricted by time of day (as an active sensor) or weather for imagery acquisition. The greatest value of using SAR sensors for maritime surveillance is the ability

of these sensors to image hard targets such as ships in background of ocean clutter. The large geographic coverage provided by some imaging modes compared to terrestrial methods along with the ability of providing near real time service and being cost effective and efficient are considered among other appealing advantages of SAR sensors [14, 15].

1.2   SAR Polarization Configurations and Ship Detection

Synthetic aperture radar may offer single polarization (single-pol), dual polarization (dual-pol) and quadrature polarization (quad-pol) imaging modes [14] as shown in Figure 1.1. Transmit and receive channel polarization may be linear or circular. In linear quad-pol radar, polarimetric information is contained in four channels; the return from quad-pol SAR for each pixel can be written as $X = [HH \quad HV \quad HV \quad VV]$, where X is the complex scattering vector with its elements are the scattering components, H denotes horizontal polarization and V denotes the vertical polarization. In each element of X, the first letter represents the transmit polarization and the second letter represents the receive one. If a single polarization is transmitted and two polarizations are received, the radar provides dual-pol data and if one polarization is transmitted and only one polarization is received, the radar provides single-pol data. The information content about the imaged scene is the largest for the quad-pol data as the relative phase between the four channels is preserved which represents a valuable source of information [12]. In contrast, single-pol SAR offers only amplitude or intensity data which contains much less information than quad-pol SAR. In the middle comes the dual-pol SAR which may provide amplitude-only or amplitude and phase data. In the context of maritime surveillance, studies have shown that quad-pol SAR yields higher performance than dual-pol and single-pol data and that dual-pol data performs better than single-pol data [16, 17, 18]. This is intuitively expected since the the amount of information extracted from SAR data gradually decreases by moving from quad-pol through single-pol data and from amplitude and phase to amplitude only data.

SAR Polarization Configurations

Single-pol
- Linear Pol. HH, HV, VH, VV
- Circular Pol. RR, RL, LR, LL
- Hybrid Pol. RH, RV

Dual-pol
- Linear Pol. HH-HV, VH-VV
- Circular Pol. RR-RL, LR-LL
- Hybrid Pol. RH-RV, LH-LV, pi/4

Quad-pol
- Linear Pol. HH-HV-VH-VV
- Circular Pol. RR-RL-LR-LL
- Hybrid quad- Pol. RH-RV-LH-LV
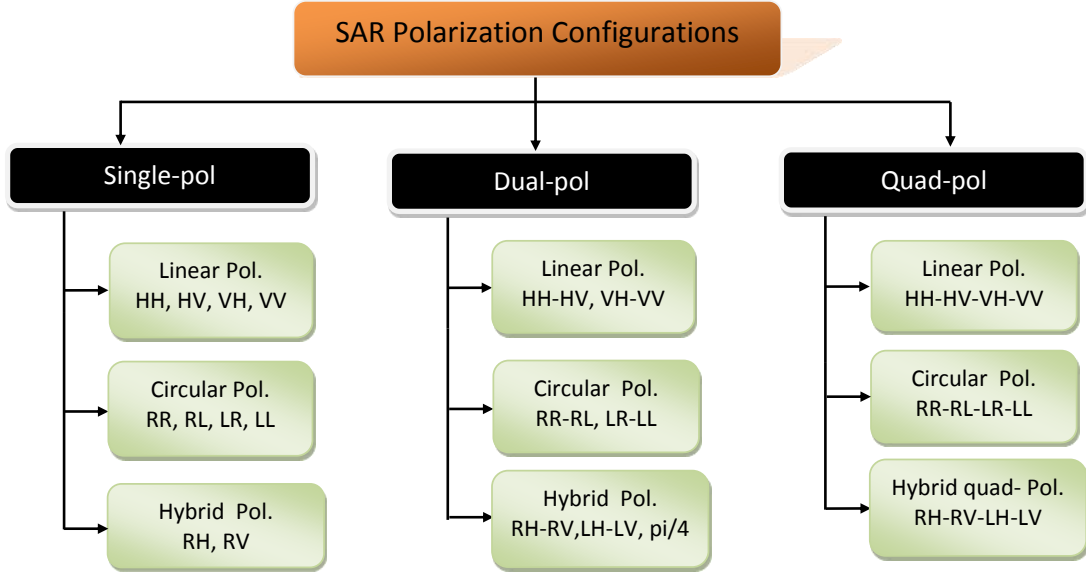
Figure 1.1: SAR polarization configurations. The first letter is the transmit polarization and the second letter is the receive polarization; H stands for horizontal, V for vertical, R for right circular and L for left circular polarization. $pi/4$ represents 45° linear-pol transmission and H and V polarization reception.

In the context of ship detection, one of the studies that compares the ship detection performance using a number of radar systems (single-pol, dual-pol and quad-pol SARs) is that of Liu et.al in [19]. The detection performance of these systems was investigated by estimating the receiver operating characteristic (ROC) plots in terms of the probability of missed detection (PMD) versus the probability of false alarm (PFA). Results of this study showed that quad-pol system has better performance than other systems since it provides the lowest PMD at almost all PFAs over all other single-pol and dual-pol configurations. Moreover, it was found that the amplitude and phase dual-pol data generally provides better performance than the amplitude only dual-pol and single-pol systems. The HH–VV amplitude and phase (again provided only from quad-pol radars) is the best dual-pol performer while the amplitude-only and amplitude and phase HH–HV and VV–VH dual-pol systems have nearly the same weaker performance due to the low correlation between co-pol and cross pol-channels.

The advantage of the quad-pol system in providing the largest information content about

the imaged scene comes at the expense of the limited swath width and the high complexity of the system [20]. In maritime surveillance applications, swath width is of critical importance since one of the objectives of this application is to cover as much area as possible to achieve both reliability and economic efficiency. Dual-pol data offers a balance between swath width and the added accuracy that can often be realized with multiple polarization [20]. In other words, dual-pol SAR provides double the swath width of quad-pol data and at the same time provides much more information than single-pol SAR. Many studies in the literature [12, 17, 19, 21] show that dual-pol systems perform better than single-pol systems in various applications. For example, in the context of ship and iceberg detection, conclusions made from the study by Howell et. al [17] to detect ships and icebergs using dual-pol amplitude and phase and single-pol data show that dual polarization systems offer improved iceberg and ship detection over single polarization systems. They show that HH–HV is recommended for operational ship/iceberg detection since the polarization HH is preferred for detection and the polarization HV is preferred for discrimination between ships and icebergs. In another study, Angelliaume et. al [21] compare target to clutter ratio using amplitude and polarimetric coherence information of HH-HV dual-pol data. They evaluate the target to clutter ratio for each channel separately and then evaluate it for the HH–HV Hermitian product. They found that the HV channel gives better contrast than co-pol data and that the HH–HV Hermitian product gives higher target to clutter ratio which confirms the fact that dual-pol data may be valuable for maritime surveillance.

Dual-pol SAR can be categorized into linear dual-pol (LP) systems and compact polarimetric (CP) systems according to the type of transmitted signal polarization [20]. In conventional linear dual-pol SAR, a linear polarization is transmitted (either H or V) and a co-pol (HH or VV) and a cross-pol (HV or VH) channels are received. Compact polarimetric systems resemble coherent linear dual-pol ones in that they retain the relative phase between the two received channels. On the other, compact polarimetric systems differ from

linear dual-pol radar in that the transmitted polarization is not linear horizontal nor vertical polarization, i.e. it may be circular or inclined linear polarization, while the received polarizations can be either linear or circular. There are currently three CP polarization configurations that have been reported in the earth observation literature [20, 22, 23]. The $\pi/4$ mode transmits a linear polarization that is oriented at 45° to the conventional horizontal and vertical polarizations, and it receives H and V. The dual circular polarization (DCP) transmits right or left circular polarization and receives both right and left circular polarizations. Finally, the circular transmit- linear receive (CTLR and also called the hybrid-polarity configuration), transmits right or left circular polarization and receives H and V. For the CTLR SAR in particular, the diversity between the transmitted and received polarizations offers the potential for CP data to have a greater amount of information than the linear dual-pol data. Therefore, in this thesis, the CTLR CP polarization configuration will be used for ship detection in SAR data. In the next section, the advantages of CP SAR in general and of CTLR CP in particular are compared to linear dual-pol SAR.

1.3 Compact Polarimetric SAR Against Linear Dual-pol SAR

In this section, we expand on the justification for selecting the CP SAR in general and the CTLR CP SAR in particular for ship detection in this research study. Below is a list of some disadvantages of the linear polarization transmission of conventional dual-pol systems over the CP SAR:

1. Linear dual-pol systems are designed such that the receiving polarization basis agrees with the transmitted one. It follows that the signal level in the cross-pol channel is less than the co-pol channel by 7- 10 dB [22, 23] (Dis.1) .

2. Transmitting a linearly polarized signal introduces a rotational selectivity onto the observation [23]. In other words, if the transmitted signal is linearly po-

larized, the received signal is stronger when the object alignment is parallel to the polarization of the incident wave and weaker if the object is rotated with respect to the incoming signal (Dis.2).

3. Linear polarization transmission is highly affected with the Faraday effect in the ionosphere when the frequency of the transmitted signal is low [24] (Dis.3).

The compact polarimetric systems overcome these drawbacks through adopting a diversity between the transmitted and received polarizations. Below, we list how CP configurations help alleviate the problems concerning linear dual-pol disadvantages:

1. The $\pi/4$ and the CTLR configurations offers a solution for Dis.1. In these configurations, the mean signal levels in both receive channels are comparable since there is no co-pol and cross-pol receive channels. As a consequence, less cross talk may occur from the stronger channel on the weaker channel [23, 25].

2. A solution to Dis.2 problem is to transmit a linearly polarized signal in which the orientation of the linear transmission is suitable to the assumed prevalent orientation of features in the imaged scene [23, 25]. This can be achieved by adopting the $\pi/4$ mode since transmitting a wave with polarization at 45° with respect to horizontal is suitable for our world where the mean surface tends to be horizontal and many natural and man-made objects tend to be vertical [23, 25].

3. Another solution for Dis.2 is to use circular polarization in the transmission (as in CTLR and DCP schemes) which leads to rotationally invariant backscatter with respect to the geometric characteristics of the scene [23, 25].

4. Dis.3 can only be alleviated by using circularly transmitted signal which is applicable for the CTLR and DCP configurations.

7

Generally, the three CP configurations are similar in that, in all three, there are advantages over full polarization in the sense of offering double the full polarimetry swath width and reducing the complexity of the radar system. However, the results are less complete than that from a quad-pol system due to the single transmit polarization [20]. Compact polarimetry offers major capabilities above those of single-pol radar [25]. Among the three CP configurations, there are several significant advantages enjoyed by a SAR in the CTLR architecture when compared to the other alternative CP schemes. These advantages are listed as follows:

1. The rotational invariance is guaranteed for the CTLR scheme for any type of backscattering geometry [23, 25] due to the circular transmission. This property may benefit ship detection since ship structure often contains dihedrals (from ship superstructure and sea-hull interface) and the power of their returned signal depends mainly on the orientation of the dihedral axis with respect to the polarization of the incident wave if it is linearly polarized. However, this is not the case if the transmitted signal is circularly polarized.

2. The signal levels in the two receive channels of the CTLR SAR are always comparable. This is clear when we note that both receiving channels include the co-pol and cross-pol returns (Eqn. 2.2). This advantage may be useful for ship detection as well since both channels would carry information about the target or the background unlike the cross-pol channel in the same polarization where the signal level is usually close to the noise floor (contains no information). Also, in this scheme the received channels are correlated and thus the relative phase between them may help in distinguishing ships from the background unlike linear dual-pol systems.

3. The CTLR configuration has been recently adopted in the Mini-RF aboard NASAs Lunar Reconnaissance Orbiter [26] and the Mini-SAR on India's lunar

Chandrayaan-1 satellite [27] to study the lunar surface. This CP configuration will be also adopted in many imaging modes of the upcoming Canadian Radarsat Constellation Mission, which is the extension of the Radarsat spaceborne SAR, for earth observation applications. This may be attributed to that hybrid polarity CP radar has relatively simple architecture than the end-to-end DCP design and has a unique self-calibrating property [23, 25].

Based on these advantages for CP SAR systems over linear dual-pol along with the wider swath width offered by these systems over that of quad-pol SAR, the compact polarimetric systems is utilized in this research rather than the linear dual-pol systems for investigating ship detection in SAR images. In particular and due to its advantages over other CP configurations, the CTLR CP configuration is used in the proposed ship detection study. Approaches used to detect ships in CP data are reviewed in Sec. 1.7. However, in order to maintain consistency for the current chapter, the basics concepts for ship detection operation in SAR data will be first reviewed in Sec. 1.4 to Sec. 1.6.

1.4   Characteristics of Ocean and Ships in SAR Images

From the basics of imaging radars, it is well known that each pixel in a radar image has a value that represents the backscattered energy from its corresponding spot on earth [14]. The characteristics of reflected backscatter are dependent on radar signal characteristics (polarization, incidence angle, frequency) and on the scattering object/surface characteristics such as the dielectric constant, roughness and local slope [14]. Scattering from objects can generally be classified into surface scattering or volume scattering or both. In surface scattering, waves are scattered from the interface between two dissimilar media while volume scattering results from particles within non-homogeneous medium [14] Generally surface scattering may be sorted into specular scattering and rough surface scattering according to the surface roughness. In specular scattering, most of the incident waves are reflected away

from the radar. On the other, in rough surface scattering, the incident waves are scattered in all directions and part of the incident waves is reflected back to the radar antenna. Incident wave may experience a number of reflections/bounces and so, scattering can also be classified according to the number of reflections to single or multiple (double, odd or even) bounce scattering.

In the context of ship surveillance, much of the images contain mainly open ocean dotted with ships and land areas. When land appears, it may be excluded by land masking before applying the detection algorithm. Therefore, in the following discussion, only the nature of backscattering from ocean and ships is discussed.

1.4.1   Backscatter from Ocean Surface

By looking at the type of scattering from the ocean surface, one can conclude that it is due to the high dielectric constant of water [14]. For an operational radar with an incidence angle of 15° - 70°, backscattering from the ocean is predominantly due to Bragg scattering [12, 28]. Under Bragg scattering, incident waves are reflected by wind-generated short waves (called capillary waves) whose wavelengths are given by Eqn. (1.1). This results in strong backscattering due to the coherent addition of the in-phase reflected waves:

$$\lambda_B = \frac{n\lambda}{2\sin\theta} \qquad n = 1, 2, 3, , ... \tag{1.1}$$

where, λ_B is the Bragg wavelength, λ is the radar wavelength and θ is the radar incidence angle between radar line of sight and the normal to the surface.

Generally, backscatter from ocean is a function of many parameters such as the wind speed and its direction relative to the radar look angle as well as polarization and incidence angle. In the absence of wind, the ocean surface is smooth and specular scattering takes place. Waves are then reflected away from the radar and hence the ocean surface appears dark in a SAR image. In contrast, higher wind speeds increase the surface roughness and more
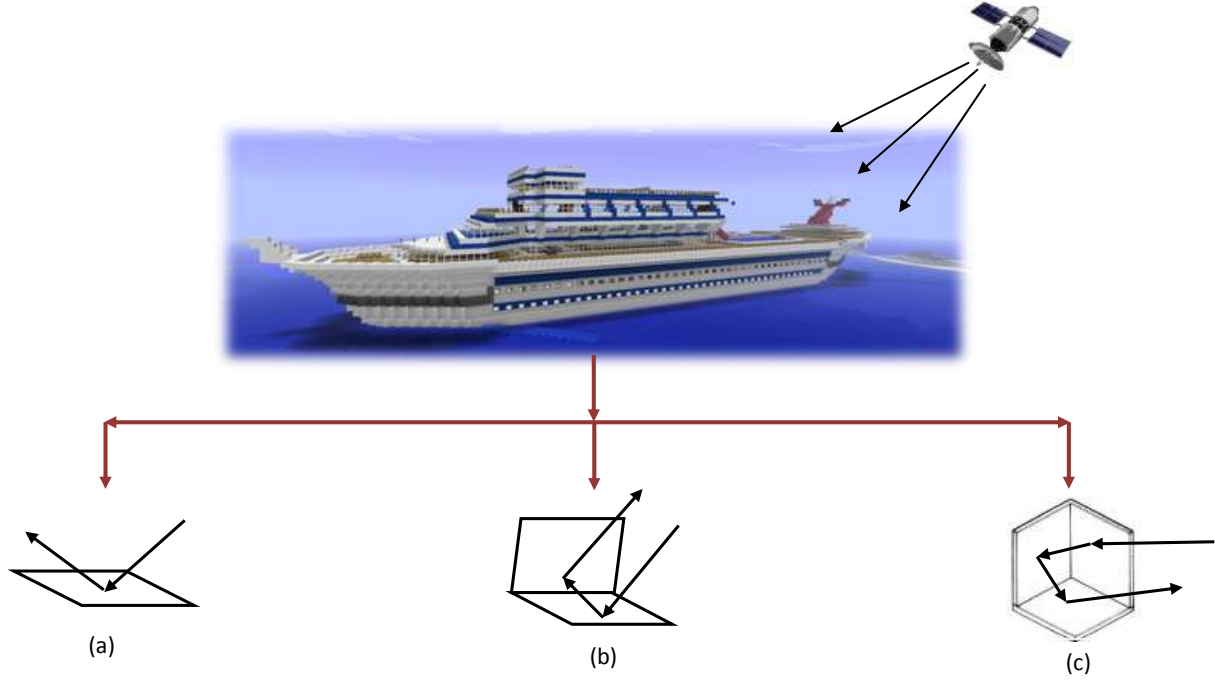
Figure 1.2: Scattering mechanisms of a ship. (a) single bounce (from flat sheets), (b) double bounce (from sea-hull and dihedrals), (c) multiple bounce (from corner reflectors).

energy is reflected back to the radar forming brighter ocean pixels. Wind direction, as well, significantly affects ocean reflections. For instance, an upwind and downwind cause higher backscatter than a cross wind. Backscattering from the ocean decreases as the incidence angle increases [12, 28]. Also backscattering of VV data is higher than HH and HV data [12, 28].

1.4.2 Backscatter from Ships

Most ships are typically constructed from large flat metallic sheets and often contain super-structure or deck configuration on them. Therefore, strong scattering from a ship may result from a variety of scattering types as the direct reflection from surfaces perpendicular to a radar beam (single bounce scattering) or from dihedral reflectors formed by two orthogonal metallic sheets (double bounce scattering) or trihedral corner reflectors (odd bounce scattering). Also, ship hull and ocean together may return significant backscatter to the radar

through the double bounce scattering [12, 28] as shown in Fig. 1.2. Therefore, ships in SAR imagery appear as a bright localized regions and they are usually detectable.

1.5   Ship Detectability in SAR images

There are many factors that come into play and affect the detectability of ships in SAR imagery. The first factor is ship characteristics such as ship superstructure configuration, orientation of a ship with respect to radar beam, ship size, material from which the ship is made and others. It is clear that large size ships fabricated from steel are more likely to be detectable than small size, fiberglass or wooden ships [12].

Another factor is the environmental conditions such as the state of the sea (wind speed), the presence of the sea ice, the proximity to the coastline. As the detectability of ships depends mainly on the contrast between the ship pixels and the ocean pixels, high wind speeds may cause higher backscattering from the ocean which decreases the ship/ocean contrast. Also near shores, ships may not be distinguishable from small islands and similarly near the polar water, ice pieces with a size comparable to ships may be detected falsely as ships due to the high back scatter from land and ice [28]. Other important factors are radar characteristics such as polarization, incidence angle and resolution. It has been reported in the literature that ship backscatter is relatively constant with respect to the incidence angle in contrast with sea clutter which decreases with increasing incidence angle [12, 29]. This means that using high incidence angle beams for ship detection are preferable due to the high ship/sea contrast.

Many papers in the literature have discussed the best polarization for ship detection in polarimetric SAR data [30]- [33]. The study of Touzi et. al [33] show that HH has higher detection performance when the incidence angle is larger than $45°$ while HV has higher performance for lower incidence angles. Similar conclusions were made in the study of Liu et. al [19], which shows the ship detection performance, quantified with the ROC curves for

a LRT detector, of a number of single and dual-pol SAR systems.

The phase information between the four polarimetric channels was also investigated. Hawkins et. al [31] argue that the relative phase between polarimetric channels may be useful for ship detection while Touzi et al [32] show that the co-pol phase difference (phase difference between HH and VV) is more useful for ship detection than the phase difference of the HV and HH or VV. This observation is sensible because the co-pol phase difference is able to distinguish between the single bounce and double bounce scattering mechanisms (presumably the former from ocean and the latter from ships) [34].

Resolution has an important and significant impact on the detectability of ships in radar imagery. Therefore, image resolution and how it affects ship detection is elaborated in Sec. 1.5.1.

1.5.1   Radar Image Spatial Resolution and Ship Detectability

Spatial resolution (or simply resolution) is defined as the minimum distance between two points that can be distinguished as separate by the SAR system [14]. Higher resolution images show more spatial details about the imaged scene and at the meantime, the area covered is relatively small in contrast to low resolution images [15]. Among the various ship characteristics that affect ship detectability is ship size (particularly ship length). In high resolution images, long ships normally occupy many pixels; this makes them more detectable by detection algorithms or even sometimes visually by eye. Conversely, in low resolution images, medium-length or small ships may occupy a single pixel. Such ships may be detectable or may not depending on the amount of their backscatter power.

Space-borne SAR systems offer a variety of beam modes, each with a particular resolution and swath width. So, generally speaking, beam mode selection for a certain application, entails trade-offs between the gain obtained from the high resolution and the reduced areal coverage associated with it. In ship detection applications, as in any other surveillance application, swath width is of critical importance. However, high detection probability (fewer

missed detections) can not be sacrificed. Many studies in the literature focus on assessing ship detectability in various beam modes of ERS and Radarsat-1 SAR system [29, 35]. The measure of ship detection performance (ship detectability) in these studies is taken to be the minimum detectable ship length. The most comprehensive study is that of Vachon et. al [29]; in this study, the minimum detectable ship length (called ship detection figure of merit-FOM in their paper) for the ERS (C-band, VV polarization) and Radarsat-1 (C-band, HH polarization) SARs is calculated under wind speed of 12 m/s. They estimated the minimum detectable ship length (l) from the minimum detectable ship RCS (σ_{ship}) by the empirical relation [29]

$$l_{ship} = \left\{ \frac{\sigma_{ship}}{0.08} \right\}^{3/7} \tag{1.2}$$

The conclusions drawn from this study are [29] :

1. The Radarsat-1 beam mode Standard-1 (Incibence angle = 23.5°) has ship detection performance better than ERS-1 SAR performance due to the decreased ocean backscatter in the HH polarization.

2. The ship detection performance improves for increasing incidence angle due to the reduction in ocean backscatter level for increasing incidence angle.

3. The ship detection performance is best for the fine beam modes due to their large incidence angle and high resolution.

4. For ScanSAR modes, the detection performance is best for large incidence angles, but is worse than the standard beam modes due to the larger resolution cell size.

From the results of this study, Vachon et. al concluded that Radarsat ScanSAR with its 300 Km swath, is a good compromise between ship detectability and swath coverage [29].

Another study was conducted on a smaller scale by Askari et.al [35] for SACLANT Under Sea Research Center, Italy, using Radarsat-1 data only. In this study, Askari et. al used a modified version of Eqn. 1.2 that takes the incidence angle (θ) into account as in Eqn. 1.3.

$$l_{ship} = \left\{ \frac{\sigma_{ship}}{0.08R(\theta)} \right\}^{3/7}, \qquad R(\theta) = 0.78 + 0.11\theta \qquad (1.3)$$

Askari et. al worked with two types of Radarsat-1 images acquired by ScanSAR and Standard beam modes. The wind speed in some of the images was high and in the others was moderate. The results of this study confirms most of Vachon et. al observations on Radarsat data. However, Askari et. al extend their study into the radiometric resolution of the data and its effect on ship detectability. Askari argues that the 8-bit quantization scale of ScanSAR data provides insufficient dynamic range for discriminating between bright targets and sea clutter under high wind speeds. Consequently, he concluded that ScanSAR imagery, in spite of its extended swath width (300 Km), is not the recommended imaging mode for automatic ship detection due to the poor radiometric resolution. On the other, Askari [35] agrees with Vachon [29] that for ScanSAR modes, the detection performance is best for large incidence angles, but is still worse than the standard beam modes.

1.6 The Ship Detection System

Ship detection system is often composed of three stages as depicted in Figure 1.3. These stages are described briefly as follows:

1.6.1 Pre-processing

Pre-processing consists of preparing the data and putting it in a compatible form for the designed detection algorithm. This includes many operations such as extracting calibrated radar cross section (RCS) values from images digital numbers (DNs), generation of amplitude/intensity images from single look complex (SLC) images, speckle filtering, spatial averaging, the conversion of scattering vector to covariance or coherency matrices or Stokes

vector to be used by the detection algorithm and other operations. Specific pre-processing operations depend mainly on the subsequent detection stages.

1.6.2   Land Masking

Land masking is the operation of masking land areas out of the image to be used for ship detection purposes since only ships in the ocean are of interest. Land masking is important because ship detectors usually produce a large number of false alarms when applied to land areas. There are two common approaches that are used for land masking. One approach is to register the SAR image with existing geographic maps and the other approach is to use automatic coastline detection algorithms [12]. The former approach is not perfect due to inaccuracy of the recorded coastline, misregistration of SAR images and tidal variations [12]. In contrast, automatic coastline detection algorithms perform better than the geo-registration method because the former method doesn't depend on geographic maps or satellite orbital data. Instead it depends on either edge detection [36] - [38] or segmentation [39, 40].

1.6.3   The Detection Algorithm

Based on the aforementioned backscattering characteristics of ships, most ship detection algorithms rely on finding image values that are high relative to the local image background [12]. The detection process is usually split into two distinct processing stages: (i) pre-screening and (ii) discrimination, which together forms the main mechanism for distinguishing a ship from the surrounding sea clutter and are often referred to in the literature as the "ship detection algorithm".

The Pre-screening Stage

Pre-screening consists of finding candidate detections in the image [12]. This is done on a pixel-basis using a thresholding process. In pre-screening algorithms, all image pixels are examined with a high probability of false alarm to distinguish all possible targets and
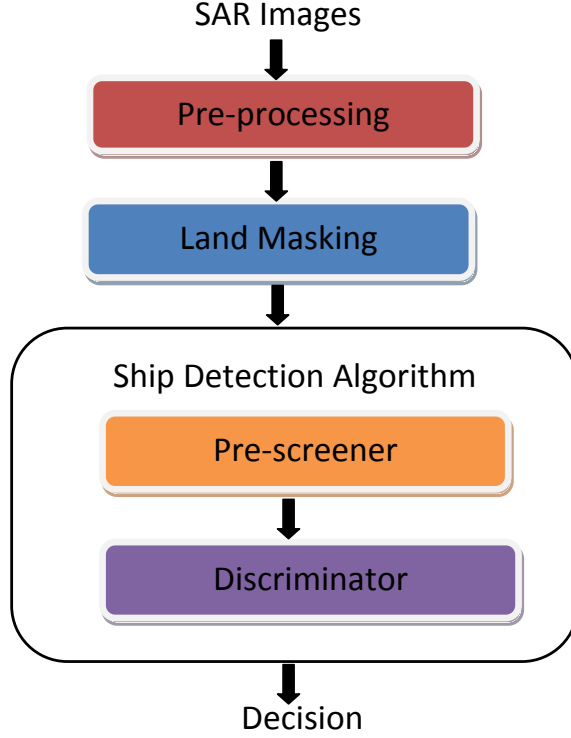
Figure 1.3: Ship detection operation in SAR images.

avoid missing some of them [12]. Thus, pre-screening algorithms should be relatively simple with respect to its computational complexity and run time. In the context of pre-screening algorithms, two types of these algorithms, classified according to the number of received radar channels, can be defined. The first type is the single channel pre-screeners and the second one is the polarimetric pre-screeners [1].

One strategy to pre-screen a single-pol SAR image is to test all image pixels against a fixed threshold value. This strategy is called the global thresholding and was taken by Lin et. al [41]; they identified ships by running a moving window of size 100 by 100 pixel through ERS SAR image. The threshold was set to be 250; the pixel is considered a candidate ship pixel if its value exceeds the threshold. In that paper, no details were provided about how this threshold was determined. However, the authors recognize that large number of false alarms resulted from this step. Another study by Lee et. al [42] aims to address ship target detection

---

[1]For dual-pol data, polarimetric pre-screeners can be usually adjusted to be applied to dual-pol images [19], [43].

in dual-frequency single polarization SAR data by using a global thresholding approach. The corresponding threshold values were determined from the gamma distribution for ocean clutter intensity at a probability of false alarm of 10^{-8}. The parameters of the Gamma distribution are estimated from an ocean block of the scene. Thus, the fixed threshold used is appropriate for this region but not for the entire scene, although no information about the sea state was given in the text. Since the main purpose of this paper [42] was to compare ship detection performance using dual frequency data (C- and L-band data), the authors do not focus or comment on the detection performance of their simple global thresholding detector.

Another single-pol pre-screening strategy is the adaptive thresholding pre-screening. The most common single-pol adaptive thresholding pre-screener is the constant false alarm rate (CFAR) detector [12, 44]. The basic geometry for the CFAR pre-screener consists of three nested sliding windows; the target window which includes the pixel under consideration is surrounded by a guard window and then a background window [44]. The purpose of the guard window is to prevent leakage of target pixels into the background region and hence that the background window represents only the underlying background statistics [12]. At each pixel of the image, the intensity value of the pixel in the center of the sliding window is compared to a local threshold calculated to achieve a specified probability of false alarm (PFA). If the pixel value exceeds the threshold, then the pixel is declared a ship pixel, otherwise, it is a background pixel. The windows move across the image one pixel at a time and a new local threshold is calculated using the background statistics at each placement of the window so the PFA remains constant over the entire image. A suitable ocean clutter model needs to be selected to denote the probability density characteristic of the background echo. After the statistical model of ocean probability density function (pdf) is determined, then the parameters of the pdf are estimated and the threshold is determined at a specified PFA.

Many configurations of CFAR detector have been developed [12, 44, 45, 46], however for ship detection the most common are the two-parameter CFAR (2P-CFAR) and the cell averaging CFAR algorithms [12, 45, 46].

In the two-parameter CFAR algorithm, the threshold value (T) depends on the mean (μ_o) and the standard deviation (σ_o) of the ocean clutter as in Eqn. (1.4). However, in the cell averaging CFAR (CA-CFAR) algorithm, the threshold depends only on the background mean value [12] as in Eqn. (1.5).

$$T = \mu_o + t\sigma_o \tag{1.4}$$

$$T = t\mu_o \tag{1.5}$$

where T is the threshold, t is called the design parameter which controls the PFA [47] and is determined either empirically or by solving Eqn. (1.6) for T; and μ_o and σ_o are estimated from background pixels.

$$\text{PFA} = \int_T^\infty f(x)\, \mathrm{d}x \tag{1.6}$$

where, $f(x)$ is the ocean clutter pdf and PFA is the desired probability of false alarm.

By moving to polarimetric detectors, it has been found that there are three strategies to perform ship detection using fully polarimetric data [12], [48], [49]. These strategies are extensively studied and compared in the work by Sciotti et. al and Lombardo et. al [45] - [49].

One strategy is to apply a single channel detector to each polarimetric channel image separately and then combine the detection results. An example of this detection strategy is given by Sciotti et. al [48] who uses a segmentation-based CFAR detection algorithm developed by Sciotti and Lombardo in [45, 46] as their single channel detector. The aim of Sciotti and Lombardo in developing their single channel CFAR algorithm in [46] is to solve the problem of the large number of false alarms suffered by standard CFAR techniques in non-homogeneous ocean. For this reason, they suggest segmenting the image before applying the detection algorithm to identify the regions with homogeneous characteristics and then

use the pixels in each segment to determine the appropriate threshold of a cell-averaging CFAR detector. They use two sets or imagery for their analysis: a low resolution and a high resolution imagery. For low resolution images, the segmentation is done by setting a hard threshold that splits the image into low wind regions (LWR) and normal wind regions (NWR). However, no details about how this threshold was set is given in the paper. For high resolution images, where the sea surface shows a large non-homogeneity, they use a segmentation technique based on simulated annealing that was especially developed for the analysis of high resolution SAR images by Cook et. al in [50]. Thus, the image can be decomposed into a set of adjacent homogeneous regions. Within each region, the pixels are used to calculate the detection threshold at a specified PFA. Their comparison of the number of false alarms when using the standard CA-CFAR and the proposed segmentation-based scheme shows that their proposed algorithm gives a very high ship detection capability yielding a controlled number of false alarms in the presence of a fluctuating background. Sciotti et. al in [48] address the problem of ship detection against non-homogeneous background in multi-channel SAR images. Due to the non-homogeneity of ocean backsactter in the image, they segment all polarimetric channels in the pre-processing stage. The single-pol detection algorithm is then applied to each polarimetric image (HH, VV, HV) and then the detection target candidates are combined since all the candidates obtained in the three channels separately are considered as detections. Thus, the polarimetric information is exploited in the combination of the detection candidates, while the segmentation stage is separately performed on the single-channel images. No absolute assessment of this work was given in the paper since the authors introduced other strategies for exploiting the polarimetric data and then built their conclusions on the comparison between these strategies.

The second strategy presented in [48] is to fuse all polarimetric channels into a single image and then apply a single channel detection algorithm to it. Sciotti et al. used the polarimetric whitening filter (PWF) [51] and the span technique for the fusion of the po-

larimetric channels. In the span technique [51] the intensity images of the HH, HV. VH and VV channels are generated and then summed together. After the fusion operation, the segmentation and detection procedures are applied to the fused data. The 2P-CFAR, the CA-CFAR and the Gaussian Generalized Likelihood ratio test (G-GLRT) are used as the single channel detectors. The G-GLRT detector belongs to the likelihood ratio test detection category in which the detection decision is made by comparing the likelihood ratio defined in Eqn. (1.7) to a threshold (T) [52].

In the G-GLRT algorithm, two sets of data are considered. The primary data consists of N pixels values obtained from a square target window of N pixels. These pixels values are arranged in a vector x. The other data set is the secondary data which is a background data to be used for the estimation of parameters of the background pdf. Under the hypothesis H_0, clutter echoes are contained in x, while under the hypothesis H_1, target echoes are contained in x. The ocean and target data are all assumed to be extracted from a zero mean Gaussian random distributions. The likelihood ratio is then obtained by dividing the joint probability density function (pdf) of primary and secondary data under the H_1 to that under the H_0.

$$\frac{P(x|w_t)}{P(x|w_c)} > T \tag{1.7}$$

where x is the data under test, $P(x|w_t)$ is the pdf of x given that a target is present (under hypothesis H$_1$), $P(x|w_c)$ is the pdf of x given that only background clutter is present (under hypothesis H$_0$) and T is a fixed threshold determined at a specified PFA.

Before discussing the results of these two strategies, a third strategy of exploiting the polarimetric information in SAR data is pointed. Sciotti et. al in [49] have introduced a multi-channel detection algorithm inspired by the G-GLRT algorithm and called it the Polarimetric G-LRT or PG-LRT. Sciotti et. al extend the G-GLRT to the multivariate case since each pixel in the polarimetric data has four complex values instead of one for the single channel data. They assume also that target and clutter are extracted from a zero mean Gaussian random distribution with polarimetric correlation properties common to all the

21

pixels and given by the covariance matrices of the target and clutter. The likelihood ratio was formed similarly as in the G-GLRT but for the multivariate case.

The results of comparing the detection performance of the three strategies show that the PG-GLRT algorithm outperforms the two other detection strategies [48, 49]. For the other two strategies, the 2P-CFAR detector outperforms the G-GLRT which performs better than the CA-CFAR for non-segmented images. However, the G-GLRT outperforms both CFAR detectors when the segmentation step is applied before detection. They also reported that polarimetric fusion using span-filtered and PWF-filtered data yields equivalent ship detection results so far [48, 49].

The multi-channel strategy was also adopted by Liu et. al in [16, 19]. Liu et. al used a LRT based algorithm. They substituted in the numerator of the likelihood ratio (Eqn. 1.7) by the joint pdf of the four polarimetric channels of the ocean pixels and that of the target pixels in the denominator. They assumed that the elements HH, HV, VH and VV of the scattering vector X to be jointly Gaussian for both ocean and target pixels. Therefore X has a pdf of the form

$$P(X) = \frac{1}{(2\pi)^{n/2}|C|^{1/2}} \exp^{-1/2(X-\mu)^H C^{-1}(X-\mu)} \tag{1.8}$$

where n is the number of polarimetric channels, μ is the mean vector, $C = E\{XX^H\}$ is the covariance of the polarimetric feature vector X and H denotes the complex conjugate transpose. Note that this detector requires a priori knowledge of the target mean vector and covariance matrix; Thus the detection criterion can be written as

$$(X - \mu_o)^H (C_o)^{-1} (X - \mu_o) - (X - \mu_t)^H (C_t)^{-1} (X - \mu_t) > T \Longrightarrow \text{target} \tag{1.9}$$

where C_o is the covariance matrix of the ocean clutter, C_t is the covariance matrix of the target (ship) backscatter and T is the threshold.

Liu et. al [16, 19] assumed that both ship targets and ocean backscatter have zero mean. They also assumed that the elements of the covariance matrix of ship samples are much larger in magnitude than those of ocean samples. Therefore, μ_o and μ_t are set to zero and

C_t is neglected in Eqn. 1.9 resulting in a detector that assumes that the ocean backscatter is Gaussian in relatively high resolution SLC data (airborne data) and doesn't take ship statistics into consideration in the decision criterion as shown in Eqn. 1.10.

$$X^H C_o^{-1} X > T \Longrightarrow \text{target} \tag{1.10}$$

Liu et. al did not compare their detection algorithm with other detectors since the aim of their work was to quantify the extent to which additional polarimetric data channels can aid in ship detection by comparing the detection performance of quad-pol data to that of various combinations of dual-pol and single-pol data [16, 19]. These results are discussed later on in this document.

It is worth mentioning that a large number of false alarms result from the pre-screening stage. Therefore, pre-screening algorithms are usually followed by a discrimination stage to eliminate the majority of false alarms while at the same time maintaining a high probability of detection.

The Discrimination Stage

In the discrimination stage, the candidate trgets from the pre-screening algorithms are processed to make more discerning decisions about the likelihood of a candidate being a target of interest at certain probability of false alarm. Usually the design of the discrimination algorithm depends on the pre-screener output, image pixel spacing and the target measurements such as the ship size [12]. This in turn usually makes it valid for specific data types and not applicable for other types. One approach for discrimination is to reject clusters with sizes less than a real ship size. This approach is taken by Lin et. al [41] since they reject detected clusters with size less than 25 pixels in ERS image of 62.5 m pixel spacing. Also, in the fishing vessel detection study of Kourti et. al [53] using SAR images of 50 to 70 meter resolution, detections with more than 5 pixels in a row or column are separated out. This discrimination approach can be implemented using a moving window in which the pixel of interest is placed in the centre of a sliding window, and then a rule is set on the neighboring

pixels [54]. For instance, Jiang et. al [55] use a 7×7 moving window and set the rule: if 7 out of the 48 window pixels are ship pixels (detected by a CFAR detector), then the center pixel belongs to a ship otherwise it is not. Lin et. al [41] use also a 3×3 window and examine the 8 neighboring pixels. If more than 3 neighboring pixels are possible ship pixels, the centre pixel is considered as a true ship pixel. Another discrimination approach depends on the supervised discrimination of ships in which the the decision about rejecting false alarms is specified by the user [12].

1.7   Use of Compact Polarimetry For Ship Detection

At the present time, there is a shortage in the CP data provided by operational spaceborne CP SAR for earth observation. This is because there is only one satellite with CP SAR on board that has been recently launched in 2012 (Risat-1) [56]. However, CP data can be simulated using quad-pol data [23, 57]. The advantages of CP data over that of linear dual-pol and its usefulness over quad-pol data in terms of swath width and system complexity, promote several earth observation studies to be investigated using CP data [22, 57, 58]. The majority of applications of CP SAR data have been terrestrial including crop classification [22, 59], soil moisture estimation [60], vegetation characterization [61, 62] and land cover mapping [57, 59]. The preliminary results obtained from these studies by using CP data are found to be comparable to those from quad-pol data.

In order to analyze CP data, there are two possible approaches [20]. These approaches are described as follows:

1.7.1   First Approach : Reconstruction of Quad-pol data

In this approach the 2×2 covariance matrix of compact polarimetric dual-pol data is expanded to a 3×3 pseudo-covariance matrix under certain symmetry assumptions. In other words, the CP data are to be used to estimate components of the quad-polarized covariance

matrix to use these reconstructed quad-pol data (termed pseudo-quad, or PQ, data) in existing quad-pol algorithms. This has been the approach taken by Souyris et. al [22] and Nord et. al [57] in two papers presenting quad-pol reconstruction algorithms. These algorithms have been developed in the context of terrestrial imaging. In order to estimate the quad-pol 3×3 covariance matrix, one must estimate nine unknowns: the amplitude of all three channels and the three Hermitian product of the received channels which are complex quantities. The CP data provide only four equations from the CP mode covariance matrix. An assumption is made to reduce the number of unknowns. This assumption is the reflection symmetry which is consistent with many terrestrial imaging scenarios [63, 64]. Under this assumption, there is complete decorrelation of the co-polarized and cross-polarized backscattering coefficients, $\langle S_{HH} \cdot S_{HV}^* \rangle = \langle S_{VV} \cdot S_{HV}^* \rangle = 0$; where S_{ij} is the complex backscatter coefficient with i transmit and j receive polarization. Thus, there are now only five unknowns: $|S_{HH}|$, $|S_{VV}|$, and $|S_{HV}|$ which are real, and $S_{HH}S_{VV}^*$ which is complex. Thus, another assumption is required to bring the number of unknowns down to four or to increase the number of equations to five.

Souyris et. al [22] proposed the following model that relates the ratio of the cross-pol intensity to the mean of the co-pol intensity to the magnitude of the co-pol coherence :

$$\frac{< |S_{HV}|^2 >}{< |S_{HH}|^2 > + < |S_{VV}|^2 >} = \frac{(1 - |\rho|)}{N} \tag{1.11}$$

where, $|\rho|$ is the co-pol coherence magnitude defined as

$$|\rho| \equiv \frac{|S_{HH} \cdot S_{VV}^*|}{\sqrt{|S_{HH}|^2 |S_{VV}|^2}} \tag{1.12}$$

Souyris et. al substituted by 4 into N in 1.11. This value is derived assuming dominant volume scattering from vegetation in the scene they used. Equation 1.11 is modified by Nord et. al in [57] to compensate for the double bounce backscatter dominated from the buildings of the urban area in the image they use for analysis. Nord et. al plot the right-hand side (RHS) of 1.11 against the left-hand side (LHS) and observe that the value of 4 in the

denominator of 1.11 is a lower limit. Their data suggests that this constant of proportionality should generally have higher values. They then replaced the proportionality constant N with the ratio of double bounce backscatter ($|S_{HH} - S_{VV}|^2$) to volume backscatter ($|S_{HV}|^2$) [57, 65] as in 1.13.

$$N = \frac{|S_{HH} - S_{VV}|^2}{|S_{HV}|^2} \tag{1.13}$$

In both the Souyris and Nord models, equations 1.11 and 1.12 are iteratively solved to estimate $|S_{HV}|^2$ and the linear co-pol coherence (ρ). The other pseudo co-pol components (S_{HH}, S_{VV}) intensities and their relative phase ($S_{HH}.S_{VV}^*$) are estimated directly from the covariance matrix elements of the CP mode and the estimated $|S_{HV}|^2$ value as will be shown in Chapter 2.

The use of the reconstruction of CP data approach for ship detection purpose is reported by Yin et. al [66]. Yin refines the Souyris reconstruction algorithm by considering the helix scattering component in the reconstruction procedures to deal with the case when reflection symmetry does not hold. He tests his reconstruction algorithm by comparing the ship detection performance of the original quad-pol data, PQ data using the original Souyris algorithm and his own algorithm and the raw CTLR dual-pol data. Yin et al. [66] present two ROC curves, for two different data sources: JPL AIRSAR and SIR-C, presumably based on two individual ships (this information was not indicated). His ROC curves show the detection performance of the original quad-pol data, PQ data based on his refined algorithm, PQ data based on the original Souyris algorithm and the compact polarimetry data (in his case he simulated $\pi/4$ data). His results for the two ships he used show that the raw CP data outperforms the reconstructed data generated by their proposed algorithm and the latter outperforms the pseudo-quad data generated using the original Souyris algorithm. He concludes that the compact polarimetry is a reasonable choice when fully polarimetric data is not available [66]. Nevertheless, this work could be criticized from two perspectives. The first is that, although their interest is the reconstruction of

CP data for ship detection which means that they mainly deal with open ocean images, they didn't test the reflection symmetry assumption to refuse it nor validate their helical scattering assumption for ocean pixels. However, since the surface scattering dominates from the ocean surface, the helical scattering assumption might be violated for ocean pixels. The other perspective is that they did not provide any reconstruction performance assessment in which the reconstructed data is compared to the original quad-pol one to prove the validity of their proposed algorithm. Therefore, it is essential to develop a reconstruction algorithm specific for maritime applications which provides high reconstruction performance for ocean data. In order to fulfill this purpose, a new reconstruction algorithm specific for maritime applications is developed in a collaboration with a research team at the U of C and published in [65]. This algorithm is called hereafter as Collins reconstruction algorithm.

Collins et. al [65] developed a new model to reconstruct quad-pol data from CP data for ocean pixels to be used for maritime applications. This reconstruction algorithm uses the four elements of the CTLR CP covariance matrix to generate the amplitude of the two co-pol components ($|S_{HH}|, |S_{VV}|$), their relative phase and the cross-pol amplitude ($|S_{HV}|$). In order to do that, reflection symmetry was assumed after it was verified and demonstrated as valid for ocean data [65]. Another assumption that was incorporated is the polarization state interpolation originally developed by Souyris et al. [22] and then modified by Nord [57] as defined in Eqn. 1.11. This assumption was demonstrated as invalid for ocean data [65]. This means that neither Souyris model nor Nord model are valid to reconstruct the C-band ocean data. Therefore, a new experimentally-based model is developed to estimate the constant of proportionality in the Souyris assumption (Eqn. 1.11) which is required to reconstruct ocean quad-pol data. Incidence angle of imaging mode beam is taken into consideration in this model to improve reconstruction performance [65]. More details are presented about this algorithm in Chapter 3. The reconstruction performance of Collins algorithm is assessed by reporting the median and standard deviation of the differences between the reconstructed

and the observed quantities as a function of incidence angle. The algorithm performance is compared to that of the Souyris and Nord algorithms. Moreover, the significance between Collins algorithm and these algorithms is tested. Results of this study show that the accuracy of the Collins algorithm stays approximately constant with the incidence angle and yields the most accurate reconstruction results for ocean data and the lowest variability [65]. In contrast, both Souyris model and Nord model accuracy deteriorate as the incidence angle increases. Moreover, the significance test suggests that the difference between the Collins algorithm and the other algorithms is significant for all reconstructed components.

1.7.2 Second Approach : Stokes and Child Parameters

In a dual-pol radar system, the received signals take the form of the the two-element scattering vector $X = [S_{tr_1} \quad S_{tr_2}]$ where S is the scattering component, t denotes the transmitted polarization and r_1, r_2 denote the receiving polarizations in the first and second channels respectively. These scattering components are complex in the SLC images. A useful representation of the information carried by coherent dual-pol systems is the Stokes vector as in Eqns.(1.14–1.17). The four-real parameters of the Stokes vector capture all of the information inherent to the dual-polarized backscattered signals [58]. Stokes parameters are real quantities composed from the intensity images (powers) and the cross product between the SLC images of the two receive channels [58]. The right-hand set of equations corresponds to linear polarization basis while the left-hand set corresponds to the circular polarization basis. The equality between the Stokes parameters of both polarization bases holds only when the transmitted polarization is the same in both cases [58].

$$S_0 = \quad \langle |S_{tH}|^2 + |S_{tV}|^2 \rangle \quad = \langle |S_{tL}|^2 + |S_{tR}|^2 \rangle \tag{1.14}$$

$$S_1 = \quad \langle |S_{tH}|^2 - |S_{tV}|^2 \rangle \quad = \langle 2\mathcal{R}(S_{tL}S_{tR}^*) \rangle \tag{1.15}$$

$$S_2 = \quad \langle 2\mathcal{R}(S_{tH}S_{tV}^*) \rangle \quad = \langle 2\mathcal{I}(S_{tL}S_{tR}^*) \rangle \tag{1.16}$$

$$S_3 = \quad \langle 2\mathcal{I}(S_{tH}S_{tV}^*) \rangle \quad = (\langle |S_{tL}|^2 - |S_{tR}|^2 \rangle) \tag{1.17}$$

where S_{ti} is the complex backscattering coefficient and i is the receive polarization which can be H for linear horizontal, V for linear vertical, R for right-handed circular or L for left-handed circular polarization while the subscript t is the transmitted polarization which is R for the current study. $\mathcal{R}$ and $\mathcal{I}$ are the real and imaginary parts of the complex quantity respectively, $*$ is the complex conjugate and the triangular brackets are the spatial averaging operator.

Although these parameters have real values, the phase information between the receive channels is retained in them. This property makes them very useful in enhancing the detectability of targets in dual-pol images. Another advantage of the Stokes parameters is that several useful "child parameters" can be derived from them such as the degree of polarization $(m = \frac{(S_1^2+S_2^2+S_2^2)^{1/2}}{S_0})$, degree of depolarization(DODP $= 1 - $m), linear polarization ratio (LPR $= \frac{S_0-S(1)}{S_0+S(1)})$, circular polarization ratio (CPR $= \frac{S_0-S(3)}{S_0+S(3)})$, degree of circular polarization (DCP $= \frac{S(3)}{S_0})$, and other parameters [58]. The importance of these "derived parameters" emerges from their relation to the type of scattering mechanisms of the scattering medium. Put differently, these parameters convey information according to the characteristics of the scene, primarily its geometric shape, roughness, dielectric properties, density, or electromagnetic penetrability [67]. Thus, the Stokes parameter values provide invaluable insight into the geophysical properties of the surface. This in turn aids in better interpretation of the imaged scene. A third advantage of using the Stokes vector is that, unlike the reconstruction approach, there is no need to make any assumptions throughout the analysis about the data, e.g. reflection symmetry assumption.

The Stokes vector and the derived parameters have been used with CP data for planetary imaging applications [20, 67, 68]. This is attributed to the available CP data from operational CP SAR systems that have been used in planetary imaging for some time. Most recently, the miniSAR on board Chandrayaan-1 collects CP SAR images of the moon [27].

In the field of earth observation, most published research has been based on the recon-

struction of quad-pol data from dual-pol data and then the reconstructed data are subjected to various classification techniques on different study areas such as crop classification [22, 59], soil moisture estimation [60] and vegetation characterization [61, 62]. There has been little work reporting the use of the CP Stokes and/or child parameters. One example is the use of Stokes parameters for crop classification [20]. Another is the use of the relative phase between the RH-RV received channels (δ) for the discrimination between wind turbines and their wakes in ocean [69]. In the context of ship detection, only a single paper [70] is found that uses the degree of polarization for the purpose of ship detection. Shirvany et. al in [70] estimate the the degree of polarization (m) in the $\pi/4$ and CTLR CP modes and the HH-HV and VV-VH linear dual-pol SAR modes and compare the contrast between the targets and the ocean of these modes using Radarsat-2 data. They do not use a particular detection algorithm nor assessment measure. They map the degree of polarization for quad-pol and linear and compact dual-pol modes and compare visually the visibility of ships in all images. Their results show that compact dual-pol modes deliver better ship detection performance compared with linear dual-pol modes. Their results, although encouraging, are purely qualitative. It is noticed in the m maps that some parts of the ocean have similar m characteristics as potential ships (and thus can be falsely interpreted as ship candidates). However, this notice does not appear in their conclusions.

For completeness, the work of Liu et. al [71] in using CP data for ship detection should be cited. They do not reconstruct PQ data nor use the Stokes and child parameters for the purpose of ship detection. However, they use the raw CTLR CP data simulated from Radarsat-2 quad-pol data to compare the detection performance of the ship detection LRT algorithm they developed in [19] with quad-pol, $|HH/HV|$ and HH. They use a single Radarsat-2 Fine Quad (FQ4) scene of the Strait of Gibraltar. The detection performance analysis is carried out on eight ships by plotting the ROC curves for these ships. All results clearly show that HH has the worst performance while the quad-pol detector has the strongest per-

formance. Results also show that dual-pol systems provide much better performance than the single-pol system. For five of eight cases studied, the simulated CTLR system provides better performance than $|HH/HV|$ system. For the other three cases, the $|HH/HV|$ system provides slightly better performance than the CTLR system. The major conclusion of this study is that a CTLR radar system provides better ship detection performance than a single-pol radar system. They also point out that more investigation is required to judge if the CTLR CP mode provides better detection performance than a conventional dual-pol system or not.

1.8 Problem Statement

In this section, the problems and the shortcomings in the literature that is associated with ship detection using compact polariemtric SAR data topic are addressed.

1.8.1 The Use of CP Data for Ship Detection Purposes

Quad-pol SAR has been widely used in ship surveillance because it offers information not only about intensity but also about the coherent phase between the four received channels. This additional information improve ship detection performance. However, this huge amount of information comes at the expense of swath width, which is essential to maximize the area coverage for ship detection application. Dual-pol data is found to offer wider swath but with a reduced amount of information. However, the construction of the compact polarimetric SAR as a dual-pol system may increase its opportunity to provide a better accuracy than linear dual-pol systems while at the same time covers double the swath width of quad-pol SAR. Recently, investigating the capabilities of CP data in earth observation applications has become an active topic of research. However, there are few published studies on the use of CP data for ship detection. A review of the existing literature shows that only two recent papers address the niche of ship detection in CP data using the two CP analysis approaches (one

paper in each direction). Considering the work done in the reconstruction of quad-pol data approach, it has been shown that the reconstruction algorithm implies two assumptions. Souyris et. al [22] and Nord et. al [57] both adopt the reflection symmetry as the first assumption while differ in the second assumption. Souyris develops a relation between the co-pol coherence and the cross polarized ratio depending on the volume scattering model that dominated from vegetation. On the other, Nord et. al modify this relation to compensate for the double bounce scattering that is caused by buildings. Recalling that the ocean surface exhibits single bounce scattering, it is anticipated that neither the original reconstruction algorithm proposed by Souyris et. al nor the modified one of Nord et. al are consistent with the backscattering from ocean. From the study of Yin et. al [66], it is concluded that they did not assume reflection symmetry assumption and instead they derived an equation depending on the helical scattering mechanism. However, this work lacks the validation of this assumption for ocean data and the performance assessment of their proposed algorithm.

Collins et. al introduces an empirically-based model to reconstruct ocean data from CP data for maritime applications [65]. In this model, the proportionality constant in the polarization state interpolation equation is evaluated at the incidence angle of the scene under study. The accuracy of Collins reconstruction algorithm is shown to be approximately constant with the incidence angle and to yield the most accurate reconstruction results for ocean data and the lowest variability [65] among other reconstruction algorithms. Therefore, this model is used in this thesis to reconstruct quad-pol data from the CTLR CP data for the purpose of ship detection. In this study, the ship detection performance of the pseudo-quad data generated using this model is to be assessed and compared to that of linear, circular and compact polarimetric dual-pol SAR data.

Like the reconstruction approach, only a single paper is found which adopts the second approach of analyzing CP data (Stokes/child parameters). The paper of Shirvany et. al [70] uses the degree of polarization to recognize ships from ocean background. As mentioned in

the review section, no detection algorithm is used. In addition, the detection performance is assessed visually depending on the contrast between ships and the ocean. We claim that the degree of polarization cannot be used alone for reliable ship detection. This is inferred from the existence of low degree of polarization regions in the ocean, which need a thresholding algorithm to reject such pixels and enhance the detection performance. The results from this study can be considered preliminary and more work need to be done to direct the use of the degree of polarization to benefit the ship detection performance. We suggest that other child parameters can be employed individually or jointly to help in improving the detection performance. Finally and most importantly, no study has been found that uses the valuable information provided by Stokes parameters which is considered to be a gap in this research area.

1.8.2   The Ship Detection Algorithms

In light of what has been reviewed in the literature about the widely used ship detection pre-screeners (CFAR and LRT detectors), one may conclude that one category of existing pre-screeners (such as CFAR detectors) ignores the ship backscatter statistical model and uses only ocean backscatter model. This is often modeled parametrically by pre-assuming a pdf for the data, estimating the parameters of the pdf using the real data and then testing the goodness of fit for the assumed pdf. In order to estimate the best fit to the data, one may try to fit many pdfs to the data and then select the most suitable one which is time consuming process. Otherwise to save time, an approximate parametric pdf may be used and this may lead to an increased number of false alarms. At present, several distribution models of ocean clutter have been adopted by CFAR algorithms. The reason is that ocean clutter under differing sea states varies through several classes of distributions such as the Gaussian distribution [72], lognormal distribution [73], K distribution [55] and others.

These CFAR detectors require extensive computations due to the need to estimate ocean backscatter pdf parameters at each pixel in the image and consequently, may take consider-

able time which is not preferred for near-real time applications such as maritime surveillance.

The other category of pre-screeners, the LRT, are optimal as they maximize the probability of detection at a given PFA [74]. However, the manner in which they are utilized for ship detection in the literature leads to a deteriorated detection performance. This is attributed to either ignoring ship statistics (which is a requirement in forming the likelihood ratio) or assuming an inappropriate pdf model for ocean and/or ship backscatter [17, 19, 49]. Liu et. al [16, 19] argue that the elements of ship covariance matrix are much larger than those of the ocean. This assumption does not always hold, especially for wooden ships or those made from fiberglass in low resolution data. From the review presented about the existing LRT detectors, it is seen that the developers of ship detection LRT algorithms always assume Gaussian pdfs for ocean and ship (if taken into consideration) backscatter in order to simplify their algorithms and reduce its computational burden. The Gaussian pdf is not the perfect fit for ocean backscatter especially in single look imagery and relatively high resolution data [75] due to the heavy tail of the the ocean backscatter distribution [19]. It is noteworthy that actual false alarm rates of a ship detection algorithm vary tremendously depending on which distribution model is appropriate for the background clutter [75]. Therefore, existing LRT algorithms sacrifice the improvement in the detection performance that could be obtained when using a more accurate pdf models and give high number of false alarms which leads to deteriorated detection performance.

In order to avoid assuming inaccurate pdfs for ship and ocean backscatter which yields to a deteriorated detection performance, an alternative approach to estimate accurate pdf for random data is recalled; that is the mixture density model [76]. In this approach the data pdf is assumed as a mixture of a number of components belonging to the same parametric family of distributions (e.g Gaussian distribution)[76]. This method has the advantages of expressing complex densities in terms of simpler densities (the mixture components) and the ability to form smooth approximations to arbitrarily shaped pdfs [76]. Another advantage

is that it provides a good model for certain data sets where different subsets of the data exhibit different characteristics and can best be modeled separately [76]. This advantage in particular is useful for maritime applications since ocean backscatter differ at different sea states from one image to another and even from location to location in the same image in which assuming a specific pdf for it is inappropriate. Thus the density function for any image can be estimated directly without assuming the pdf. Accordingly, it is anticipated that using mixture models will yield more accurate pdf estimation for ocean and ship returns and hence improve detection performance.

From the literature review of the ship detection algorithms, it is noticed that all CFAR and LRT detectors employ either the complex scattering vector or the intensity SAR data for detecting ships. However, no thresholding pre-screeners have been reported that utilize the Stokes vector or any of its derived parameters for ship detection. It is anticipated that the valuable information content of the Stokes vector and its derived parameters may benefit ship detection. Therefore in this thesis, one of the objectives is to merge all types of pre-screeners (global thresholding, CFAR and LRT) to develop new robust pre-screener that utilize the observed Stokes parameters individually and jointly. This pre-screener is designed to take the advantages of each existent pre-screening detector and discard its disadvantages. The pdfs required by the adaptive thresholding detectors (CFAR and LRT) are estimated using the Gaussian Mixture Model (GMM) method to take local sea state into consideration.

By looking at the discrimination algorithms, we find that most existing ones depend on removing individual false alarm pixels and groups of contiguous false alarm pixels with an overall size which is less than a real ship size. Such discriminators can be described to be local for a specified image since they are highly dependent on the ship sizes and image resolution. Therefore, it may not be valid for other images. However, discriminators that distinguish pixels depending on the dominant scattering mechanism over those pixels may give better discrimination between real targets and ocean pixels. Existing discriminators that exploit the

physics of ocean and ship backscattering into discriminating ships from ocean false alarms usually use polarimetric decomposition techniques [77] or classification [78]. These physics are related to many parameters that can be extracted from multi-polarization SAR data such as degree of polarization, coherence and phase shift between received channels and other parameters. The use of such parameters may increase the robustness of the discriminator and provide more reliable discrimination in comparison to ship-size related discriminators.

1.9   Objectives and Organization of the Thesis

Based on the literature survey and according to the current problems and research gaps discussed in Sec. (1.8), the major objectives of this thesis are as follows :

1. The investigation of the possibility and benefits of using CP SAR generally and the pseudo-quad data generated by Collins algorithm specifically for ship detection. This investigation includes the assessment of the relative ship detection performance of the reconstructed data, raw CP and other linear and circular dual-pol SAR data. Moreover, it is intended to investigate the possibility of using lower resolution data, which provides wider swath width, effectively for ship detection.

2. The investigation of the effect of spatial resolution, ship orientation and imaging mode incidence angle on the ship detection performance of a number of SAR systems.

3. The development of a new hybrid ship detection algorithm for hybrid CP data. In this algorithm, CP Stokes parameters and some of their derived parameters are used for ship detection. In this algorithm, four detection strategies are utilized together to improve detection performance.

4. The application of the proposed detection algorithm to a number of RS2 scenes with medium and low resolution and the assessment of the detection performance of the proposed algorithm.

This thesis has two parts. The first part is composed of Chapters 2 and 3 and investigates

the possibility and benefits of using CP SAR generally, and the PQ data generated by Collins reconstruction algorithm specifically, for ship detection. This is done by comparing ship detection performance of compact polarimetric SAR systems to linear dual polarimetric (LP) and circular transmit/circular receive polarimetric (CirP) SAR systems. This ship detection investigation study is conducted on two sets of SAR data. The first set has a relatively fine resolution acquired by the RS2 Fine Quad (FQ) mode beams. The second set has a lower resolution simulated data. Both sets of data are then fed to a Likelihood Ratio Test detection algorithm for the ship detection performance investigation. The impact of spatial resolution, ship orientation with respect to the radar beam and the effect of the imaging mode incidence angle on the ship detection performance are all investigated in this part.

Chapter 2 reviews the CP reconstruction algorithm that is used in this research study, i.e. Collins reconstruction algorithm and the LRT detection algorithm. Moreover, it introduces the experiment performed to investigate the ship detection performance. Chapter 3 shows the results of this part and provides the corresponding conclusion remarks and suggested future research work.

The second part of the thesis is composed of Chapters 4 and 5 and it introduces the proposed Stokes parameters hybrid ship detection algorithm. In Chapter 4, the theoretical concepts and related basics of each part of the proposed CP hybrid detection algorithm is presented along with a detailed description of the proposed algorithm.

In Chapter 5, the data used and the results of applying the proposed ship detection algorithm to a number of Radarsat-2 scenes with medium and low resolution are discussed and concluded. Finally, Chapter 6 outlines the main conclusions of the work done.

Chapter 2

Ship Detection Performance Analysis of Compact Polarimetric Data Methods and Theoretical Concepts

In this chapter, the possibility and benefits of using compact polarimetry SAR generally and the pseudo-quad data specifically for ship detection are investigated. This is done by comparing the ship detection performance of compact polarimetric SAR systems to conventional linear dual polarimetric (LP) and circular transmit- circular receive polarimetric (CirP) SAR systems. This ship detection investigation study is conducted on two sets of SAR data. The first set has fine resolution of about 6 m. This data is acquired with the RS2 Fine Quad (FQ) mode beams. The second set has a lower resolution. It is obtained by simulating the FQ data into RCM data in three modes: the Low Resolution, the Medium Resolution and the Ship Detection modes. Another purpose of this study is to investigate the possibility of using lower resolution data, which provides wider swath width, effectively for ship detection. Consequently, the analysis herein has two parts; the first part covers the ship detection analysis using the FQ data while the second part covers the ship detection analysis using RCM data. The CP data used in this study has two forms: one form is the raw CTLR data (RH-RV) and the other form is the pseudo-quad data generated by reconstructing quad-pol data using Collins reconstruction algorithm [65] which was developed in a collaboration work with a research team at U of C. The linear dual-pol systems tested in this study are the HH-HV, VV-VH and the amplitude-only HH-VV. Both sets of data are then fed to a Likelihood Ratio Test detection algorithm for ship detection performance investigation. The detection performance is assessed for each SAR system using ROC curves and the median probability of missed detection at a specific probability of false alarm. In this study, the impact of spatial resolution, ship orientation with respect to the radar beam

and the effect of the incidence angle on the ship detection performance is investigated.

This chapter is organized as follows. Section 2.1 provides a description of the original RS-2 and the simulated RCM data used in this study. Section 2.2 exhibits the experimental methods employed in this work. This section contains a review of the reconstruction algorithm used and the Likelihood Ratio Test ship detection algorithm. Finally Section 2.3 concludes the chapter.

2.1 Data and Study Site

The polarimetric data set used in this chapter is shown in Table 2.1. It is composed of 14 Fine Quad (FQ) scenes of the Strait of Gibraltar acquired by several Radarsat-2 beams. The scenes are located around $(35°– 37°)$ N, and $(5°– 6°)$ W. The scenes are numbered in Table 2.1 and the radar backscatter coefficient (σ^o) values were used for the calibration of the data.

The "Sc. No" column in the table lists the scene numbers by which each scene is referred to in the upcoming analysis. The "Beam" column lists the Fine Quad beam position, with lower positions having lower incidence angles, and vice versa. The "Inc. Angle" column lists incidence angle range of each radar beam. The "Acq. date" and time "Acq. time" refer to the acquisition date and time of each scene respectively. "W.S. (m/s)" lists the mean wind speed of each scene, in meters per second, as calculated using the mean value of the HV $\sigma°$, according to the equation developed in [79]. "No. Sh." is the the number of ships used in each scene. All scenes have a range sample spacing of 4.73 m and azimuthal sample spacing varying from 4.8 to 5 m according to beam position. Nominal Radarsat-2 Fine Quad mode resolution is approximately 5.2 m in range by 7.6 m in azimuth. Automatic identification System (AIS) data is available to validate the imaged ships in all scenes.

In this work, the RCM data is simulated as single look complex (SLC) images in three imaging modes: the Medium Resolution, the Low Resolution and the Ship Detection modes [80]. The simulated data had a noise floor of approximately -22 dB (according to the RCM

Table 2.1: An overview of the Fine Quad Radarsat-2 data of the Strait of Gibraltar used in this study. Sc. No. is the Scene number, Beam is beam number, Inc. Angle is the incidence angle range covered by each beam, Acq. date is the scene acquisition date , Acq. time is the scene acquisition time, W.S is the wind speed in m/s and No. Sh. is the number of ships per scene used in the current study.

Sc. No.	Beam	Inc. Angle	Acq. time	Acq. date	W.S (m/s)	No. Sh.
1	2	$19.77° - 21.78°$	18:11:03	2008-11-26	7.1	7
2	2	$19.77° - 21.78°$	18:11:05	2008-11-26	6.7	4
3	2	$19.77° - 21.78°$	06:35:01	2008-10-20	3.6	12
4	4	$22.16° - 24.08°$	18:11:01	2008-12-20	5.8	7
5	4	$22.16° - 24.08°$	18:11:04	2008-12-20	5.7	12
6	4	$22.16° - 24.08°$	18:10:54	2008-07-29	6.0	12
7	8	$26.88° - 28.71°$	06:30:56	2008-11-20	11.3	11
8	8	$26.88° - 28.71°$	06:30:54	2008-11-20	11.8	11
9	12	$31.34 ° - 33.03°$	06:26:46	2008-11-27	11.9	8
10	12	$31.34° - 33.03°$	06:26:48	2008-11-27	13.8	3
11	21	$40.17° - 41.61°$	06:22:40	2009-02-14	13.3	8
12	21	$40.17° - 41.61°$	06:22:38	2009-02-14	12.1	7
13	21	$40.17° - 41.61°$	18:23:32	2009-02-09	6.2	12
14	21	$40.17° - 41.61°$	18:23:29	2009-02-09	5.5	11

Table 2.2: An overview of the simulated RCM data in the three imaging modes used in this study. This Table shows the incidence angle (Inc. Ang.) in degrees for each of the modes, the multilook resolution (ML Res.) and the simulated SLC resolution (SLC. Res.) in the (range x azimuth) directions and the nominal swath width (N.S.W) in Km.

RCM Beam Mode	ML Res.	Inc. Ang.	. SLC. Res.	N.S.W
Medium Resolution	50 m	$19° - 58°$	7.9 x 49.7	350 Km
Low Resolution	100 m	$19° - 54°$	8.3 x 98.8	500 Km
Ship Detection	variable	$36° - 51°$	2.7 x 48	350 Km

classifications) while the original Radarsat-2 data has noise floors of approximately -30 dB. The signal levels for the S_{HH},S_{VV} and S_{HV} of the ocean data were compared to the noise floor values provided in the RS-2 meta data for each scene. The S_{HH} and S_{VV} are well above the noise while the S_{HV} is close to the noise floor but still above it. The incidence angle range "Inc. Ang.", the multilook resolution "ML Res.", the simulated SLC resolution "Sim. Res." and the nominal swath width "N.S.W" of the simulated RCM data are indicated in Table 2.2. It is noteworthy to mention that the simulated SLC resolution for the ship Detection mode varies with the incidence angle. The resolutions shown in the table are for Scene 11

acquired by FQ 21 beam. As indicated in Table 2.2, the RCM Ship Detection mode covers the incidence angle range ($36°$ – $51°$). Therefore, in this study, the Ship Detection mode is only simulated for the scenes acquired by the FQ21 beam ($40.17°$–$41.61°$). The RCM data is simulated using software developed and provided by Dr. Francois Charbonneau at Canada Centre for Remote Sensing (CCRS).

2.2   Methods

In this section, the methodology followed to investigate the ship detection performance for CP SAR is presented. In the beginning, Collins reconstruction algoritm used to generate the pseudo-quad data from the CTLR CP data is briefly presented. This is followed by an explanation of the procedures of the experiment performed to analyze the ship detection performance. This section is ended by a review of the LRT ship detection algorithm employed in the current work.

2.2.1   The Reconstruction Algorithm

The reconstruction of quad-pol data is the process of regenerating some elements of the quad-pol covariance matrix from compact polarimetric data under some assumptions. The purpose of quad-pol reconstruction is to be able to use existing quad-pol methods of analysis while maintaining the double quad-pol swath width provided by dual-pol SAR. In this research, the quad-pol reconstruction is performed using simulated CTLR data. The reconstruction process has two steps. The first step is to simulate the CTLR data from linearly polarized quad-pol data and second, to reconstruct the elements of the quad-pol covariance matrix. The resultant reconstructed quad-pol data is called the pseudo-quad data or the PQ data. In this study, Collins reconstruction algorithm [65] is used to generate the PQ data. This reconstruction algorithm is presented in brief in this section.

Quad-pol data scattering vector is composed of four elements as mentioned in Chapter

1. However, under the scattering reciprocity assumption $(S_{HV} = S_{VH})$, it can be written as

$$\mathbf{X}_{\text{quad-pol}} = \begin{bmatrix} S_{HH} & \sqrt{2}S_{HV} & S_{VV} \end{bmatrix}^T \tag{2.1}$$

The CTLR CP SAR scattering vector is given as Eqn. 2.2 and the CTLR covariance matrix may be written as a sum of three components [22, 57] as in Eqn. 2.3.

$$\mathbf{X}_{\text{CTLR}} = \frac{1}{\sqrt{2}} \begin{bmatrix} S_{HH} - jS_{HV} & S_{HV} - jS_{VV} \end{bmatrix}^T \tag{2.2}$$

$$\mathbf{C}_{\text{CTLR}} = \frac{1}{2} \Bigg\langle \begin{bmatrix} |S_{HH}|^2 & i(S_{HH} \cdot S_{VV}^*) \\ -i(S_{VV} \cdot S_{HH}^*) & |S_{VV}|^2 \end{bmatrix} + \begin{bmatrix} |S_{HV}|^2 & -i|S_{HV}|^2 \\ i|S_{HV}|^2 & |S_{HV}|^2 \end{bmatrix} + \\ \begin{bmatrix} -2\mathcal{I}(S_{HH} \cdot S_{HV}^*) & S_{HH} \cdot S_{HV}^* + S_{VV}^* \cdot S_{HV} \\ S_{HH}^* \cdot S_{HV} + S_{VV} \cdot S_{HV}^* & 2\mathcal{I}(S_{VV} \cdot S_{HV}^*) \end{bmatrix} \Bigg\rangle \tag{2.3}$$

where T is the transpose operator, the angle brackets represent spatial averaging and $\mathcal{I}$ is the imaginary part of a complex number.

In order to estimate the quad-pol 3×3 covariance matrix, it is required to estimate nine unknowns; three unknowns are real: $(|S_{HH}|^2, |S_{VV}|^2, |S_{HV}|^2$ and three unknowns are complex: $S_{HH}.S_{HV}^*$, $S_{VV}.S_{HV}^*$ and $S_{HH}.S_{VV}^*$). However only four equations are available from the CP mode covariance matrix; C_{11}, C_{22} and C_{12} which is complex. Thus, some assumptions need to be made to constrain the solution space and reduce the number of unknowns or increase the number of equations. Collins et. al [65] make the following assumptions:

1) Reflection Symmetry:

Reflection symmetry refers to the media that is symmetric with respect to the incidence plane [22]. Under this assumption, there is a complete decorrelation of the co-polarized and the cross-polarized backscattering coefficients, i.e.

$$\langle S_{HH} \cdot S_{HV}^* \rangle = \langle S_{VV} \cdot S_{HV}^* \rangle = 0 \tag{2.4}$$

42

This assumption simplifies the CTLR covariance matrix (Eqn. 2.3), by removing the third component, hence reducing the number of unknowns to five: $|S_{HH}|$, $|S_{HV}|$, $|S_{VV}|$ which are real, and $(S_{HH}.S_{VV}^*)$ which is complex.

The reflection symmetry assumption is consistent with many terrestrial imaging scenarios [63, 64]. However, Collins et. al demonstrated that the reflection symmetry assumption is valid for ocean backscatter at C-band [65]. After applying the reflection symmetry relation, the quad-pol covariance matrix simplifies to

$$
\mathbf{C_{PQ}} = \left\langle \begin{bmatrix} |S_{HH}|^2 & 0 & S_{HH}S_{VV}^* \\ 0 & |S_{HV}|^2 & 0 \\ S_{VV}S_{HH}^* & 0 & |S_{VV}|^2 \end{bmatrix} \right\rangle
\tag{2.5}
$$

Thus, there are now only five unknowns: $|S_{HH}|$, $|S_{VV}|$, and $|S_{HV}|$ which are real, and $S_{HH}S_{VV}^*$ which is complex.

2) Polarization State Interpolation:

Collins et. al adopts the polarization state interpolation assumption developed by Souyris et. al [22] as in Eqn. 1.11 and recalled herein for convenience

$$
\frac{< |S_{HV}|^2 >}{< |S_{HH}|^2 > + < |S_{VV}|^2 >} = \frac{(1 - |\rho|)}{N}
\tag{2.6}
$$

Souyris et al. [22] developed this relation (2.6) based on the scattering behaviour of fully polarized and fully depolarized backscattered waves. For a fully polarized scattered wave, a very small amount of cross-pol energy is scattered, i.e., $|S_{HV}|^2 = 0$. In addition, the HH and VV backscattered waves will be almost perfectly correlated; thus, the magnitude of the copolarized coherence is nearly one: $|\rho_{HHVV}| = 1$ [22, 65]. On the other hand, for fully depolarized backscattered waves, the average backscattered power does not depend on the polarization state of the scattered wave. Hence, there is no correlation between the co-pol scattered waves, i.e. $|\rho_{HHVV}| = 0$, and the intensity of all scattered energy is about the same, i.e. $|S_{HH}|^2 = |S_{VV}|^2 = 2|S_{HV}|^2$. The situation for backscattering from natural materials

will be somewhere between these two extremes [65]. The proportionality constant N, in 2.6, depends mainly on the dominant scattering mechanism [81].

Collins et.al [65] test the validity of both Souyris (with $N = 4$) and Nord (using N as in Eqn. 1.13) models for ocean data. Their results show that neither the approximation of N to be "4" nor the form 1.13 appear to be valid for ocean data, i.e. neither Souyris model nor Nord model is valid to reconstruct the C-band ocean data. Therefore, Collins et. al decided to retain the form of Souyris original model however, estimate the value of N for each scene based on the incidence angle [65]. They use the following equation, which follows directly from rearranging equation 2.6, for N calculation of each pixel [65]:

$$N = (1 - |\rho|)\frac{< |S_{HH}|^2 > + < |S_{VV}|^2 >}{< |S_{HV}|^2 >} \tag{2.7}$$

In order to construct their model, they calculate N for each pixel in a 1000×1000 pixel sub-image of a number of scenes with moderate wind speeds [65]. A mean N $(\overline{N})$ for each image is calculated and used to investigate its dependence on image geometry, i.e., the incidence angle, and wind speed. They observed an increase in $\overline{N}$, with a decreasing incidence angle [65]. However, they found that the dependence of $\overline{N}$ on wind speed is much weaker than that on the incidence angle. Therefore, they did not model $\overline{N}$ as a function of wind speed. So, they developed a simple empirical model to estimate $\overline{N}$ from the incidence angle [65] as in 2.8. This model is then used to estimate $\overline{N}$ to perform the reconstruction.

$$\overline{N} = 6.52 + 18305.73 \exp^{\{-\theta^{0.60}\}} \tag{2.8}$$

where $\overline{N}$ is the constant of proportionality (N) of Eqn. 2.6 and θ is the mean incidence angle of the studied scene.

2.2.2 Reconstruction Iterative Equations

In this study, equations 1.12 and 1.13 are iteratively solved to estimate $|S_{HV}|^2$ and the linear coherence (ρ). The iterative equations of 1.12 and 1.13 for Collins model is given as Eqns.

2.9 and 2.10. $\overline{N}$ in 2.10 is estimated using the model 2.8 at the scene mean incidence angle.

$$|\rho|_{(i+1)} = \frac{-iC_{12} + |S_{HV}|^2_{(i)}}{\sqrt{(C_{11} - |S_{HV}|^2_{(i)})(C_{22} - |S_{HV}|^2_{(i)})}} \qquad (2.9)$$

$$|S_{HV}|_{(i+1)} = \frac{C_{11} + C_{22}}{2}\left(\frac{1 - |\rho_{(i+1)}|}{\overline{N} + 2(1 - |\rho_{(i+1)}|)}\right) \qquad (2.10)$$

The starting estimate of $|S_{HV}|^2$ is set to be zero, then the first estimate of $|\rho|$ is calculated using 2.9. The $|S_{HV}|^2$ is updated using 2.10, then the process alternates between 2.9 and 2.10 until reaching convergence. In this study, convergence is considered reached when $|S_{HV}|^2$ be within 1% of its previous estimate. For each pixel, iterations continue until convergence or till reaching 100 iterations, whichever came first. It is worthy to mention that for some pixels, the magnitude of ρ converges to a value greater than one, which is impossible. When that happen, the iterations are halted and the $|S_{HV}|^2$ is set to zero for that pixel.

The other pseudo co-pol components (S_{HH}, S_{VV}) intensities and their relative phase $(S_{HH}.S^*_{VV})$ are estimated directly from the covariance matrix elements of the CP mode and the estimated $|S_{HV}|^2$ value as follows :

$$|S_{HH}|^2 = C_{11} - |S_{HV}|^2 \qquad (2.11)$$

$$|S_{VV}|^2 = C_{22} - |S_{HV}|^2 \qquad (2.12)$$

$$S_{HH} \cdot S^*_{VV} = -iC_{12} + |S_{HV}|^2 \qquad (2.13)$$

Thus the covariance matrix of the pseudo-quad data derived from the CTLR CP SAR data can be written as,

$$\mathbf{C}_{PQ} = \begin{bmatrix} C_{11} - |S_{HV}|^2 & 0 & -iC_{12} + |S_{HV}|^2 \\ 0 & 2|S_{HV}|^2 & 0 \\ (-iC_{12} + |S_{HV}|^2)^* & 0 & C_{22} - |S_{HV}|^2 \end{bmatrix} \qquad (2.14)$$

where C_{11}, C_{12} and C_{22} are the elements of the CTLR covariance matrix.

The main purpose in reconstructing the linear quad-pol covariance matrix is to detect maritime targets such as ships. To perform ship detection, the Likelihood Ratio Test method developed in [16, 19] is used.

2.2.3   The Experiment

Figures 2.1 and 2.2 show strategy flowcharts of the work presented in Chapters 2 and 3. Figure 2.1 shows the flowchart of the FQ analysis part of the ship detection investigation study. In this part, the FQ data is used to generate the LP data and to simulate the CirP and CTLR CP data by combining the fully polarimetric channels. The RR-RL data is simulated as in the CirP scattering vector defined in 2.15 while the RH-RV is simulated as in 2.2 [57]. After that, the pseudo-quad CP data is generated using Collins reconstruction algorithm. Then, all LP, CirP and CP SAR systems (also called detectors through the thesis) are passed to the LRT detector to distinguish between ship and ocean. The LRT detection algorithm is presented in Sec. 2.2.4.

$$\mathbf{X}_{\text{CirP}} = \frac{1}{2} \left[\; S_{HH} - S_{VV} + j2S_{HV} \qquad j(S_{HH} + S_{VV}) \; \right]^{T} \qquad (2.15)$$

Figure 2.2 shows the strategy of assessing the ship detection performance of the RCM analysis part of this work. In this part, first, the RCM data is simulated using the FQ data in three modes: the Low resolution, Medium Resolution and the Ship Detection modes. Next, the CirP and CTLR data are simulated from the simulated RCM quad-pol data similarly as in the FQ analysis part. Then, the pseudo-quad CP data is generated as in the FQ case. After that, all these SAR systems are passed to the LRT detection algorithm.

Now we have the following systems to be analyzed for the ship detection performance assessment in both FQ and RCM parts of the analysis:
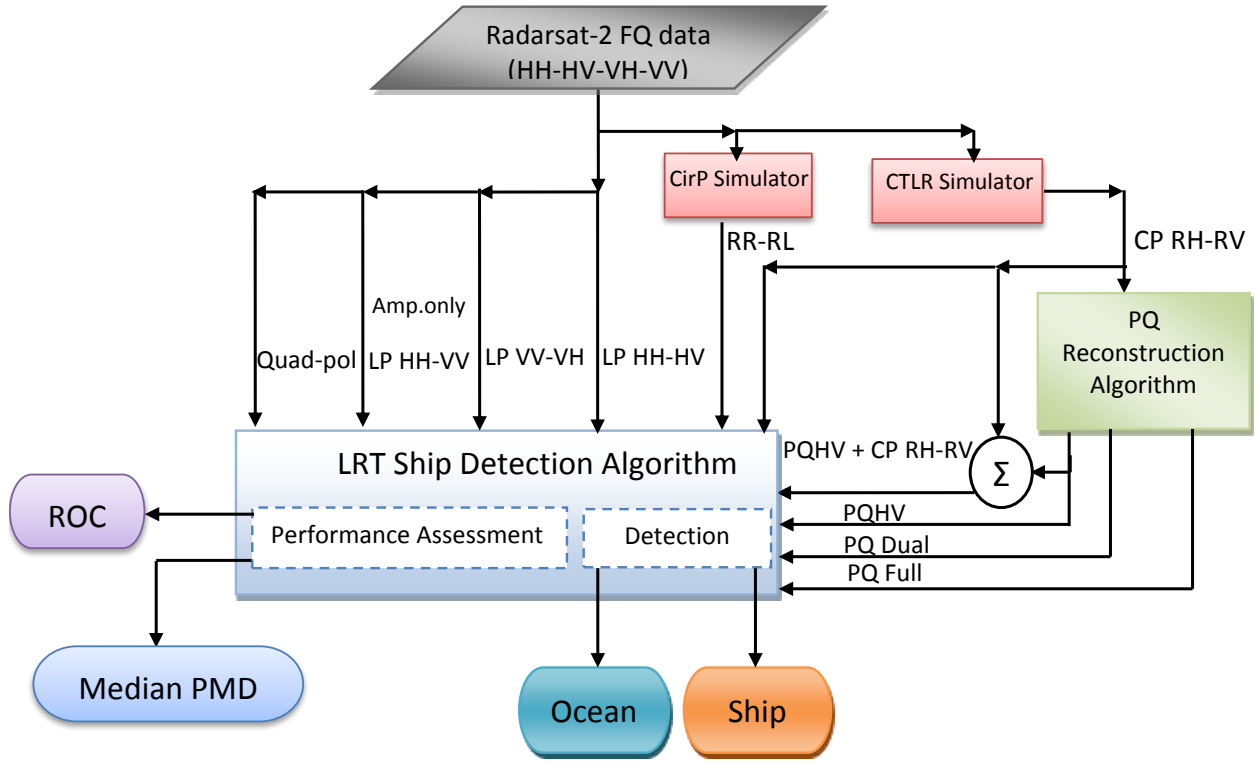
Figure 2.1: Strategy flowchart of the FQ analysis part in this chapter.

Linear:	coherent HH-HV, coherent VV-VH and incoherent HH-VV
Raw CirP :	coherent RR-RL
Raw CTLR :	coherent RH-RV
Reconstructed PQ:	Full PQ, coherent PQ HH-VV, and PQHV
Merged CP detector:	RH-RV-PQHV

This is a total of nine systems. We do not examine any of the observed single-pol systems as it has been reported in the literature to have the worst detection performance with respect to dual-pol and quad-pol systems [18, 19]. It is worth mentioning that in the FQ analysis part, the quad-pol detector is also used as a reference and is included in the performance comparison. However, in the RCM part, the quad-pol detector is not included in the comparison as the upcoming RCM provides only dual polarization on all low and medium resolution modes [80]. This is to provide wide swath width to be suitable for

47
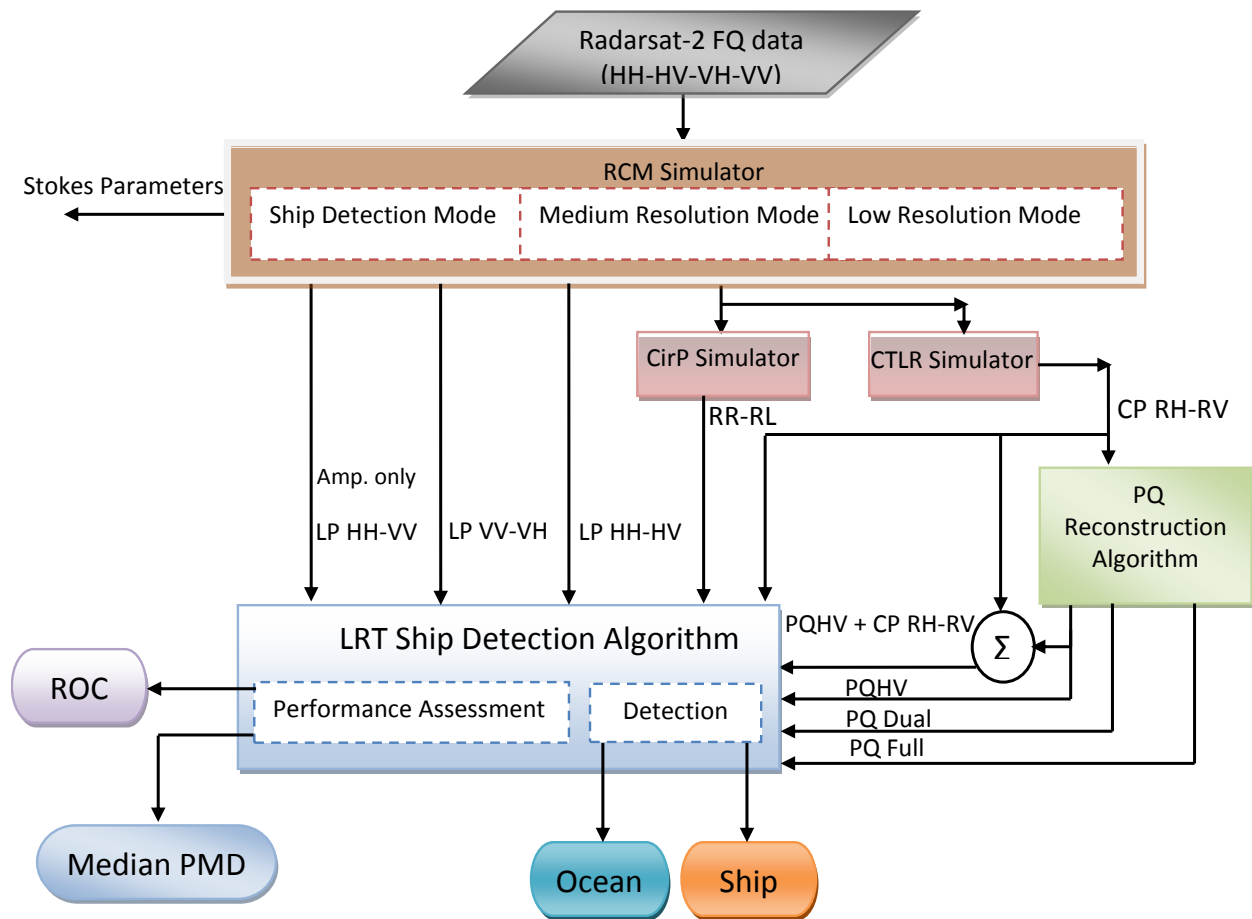
Figure 2.2: Strategy flowchart of the RCM analysis part in this chapter.

maritime surveillance applications. Moreover, in the RCM analysis part, one should note that the HH-VV configuration is not available in the RCM Ship Detection imaging mode, however only in the Medium and Low Resolution modes.

Ship Orientation Impact on Ship Detection

It is anticipated that the orientation of the ships with respect to the radar range direction might affect the detector performance. Higher performance (lower PMD) is expected for ship orientations of 90° and, to a lesser extent, 0°. At 90°, the ship is broadside to the radar range direction and offers the largest surface area facing the radar. At this angle, the hull and superstructure should generate a significant amount of double bounce and a higher radar cross section, thus a lower PMD [81]. At 0°, the ship offers the smallest surface area but its superstructure should also be roughly perpendicular to the range direction and it is expected to see a slightly lower PMD than at other orientations [81]. At all other angles, one would expect the radar pulse to be reflected away from the radar. Thus we are looking for enhanced performance (lower PMD) at 0° and 90°. So, in this study the impact of ship orientation on the detection performance is explored. The orientation relative to the range direction is measured, with 0° being parallel to the range direction. However, the bow from the stern could not be discriminated so, 0° is equivalent to 180° and 90° (perpendicular to the range direction and parallel to the azimuth direction) is equivalent to 270°. We also assume azimuthal symmetry, so 45° is equivalent to 135°. Thus, the angles are measured between 0° and 90°. The orientation of a ship is approximated to be included in one of five categories $(0°, 30°, 45°, 60°$ or $90°)$. In order to assess the impact of ship orientation on the detection performance numerically, we compute what we call the "the Number of Lowest PMD Occurrence Percentage – NLPOP". The NLPOP can be defined as:

$$\text{NLPOP} = \frac{\text{Number of times the lowest PMD occurs at a specific orientation category}}{\text{Number of detectors} \times \text{ Number of beams}} \times 100\%$$

(2.16)

Incidence Angle Impact on Ship Detection

In this chapter, the impact of incidence angle on the ship detection performance is investigated as well. For this study, scenes acquired by five beams (B) are used. Each beam has a specific incidence angle range as follows :

B2 : 19.77° - 21.78°.

B4 : 22.16° - 24.08°.

B8 : 26.88° - 28.71°.

B12 : 31.34° - 33.03°.

B21 : 40.17° - 41.61°.

For this study, 125 ships from all scenes acquired by these beams as depicted in Table 2.1 are identified. These ships have verified positions from the Automatic Identification System data distributed with SAR data. Rather than reporting the detection results for all 125 ships, we summarize detection results for all ships at a particular orientation by reporting the median PMD and indicate the number of ships used for the calculation. The median is used since the sample sizes are small and the median is less affected by outliers [81].

2.2.4   LRT Ship Detection Algorithm

In the LRT detection algorithm, a decision variable is calculated using the Neyman-Pearson criteria [16, 19]. The decision variable (L) is formed from the ratio of ship and ocean probability density function values at each pixel in the scene. Under the assumption of Gaussian statistics for ships and ocean scattering components, the decision variable is given by:

$$L = X^H C_o^{-1} X = \begin{cases} > \eta & \text{for a ship} \\ \leq \eta & \text{for ocean} \end{cases} \qquad (2.17)$$

where X is the scattering vector of the SAR system, $C_o = E(X_o X_o^H)$ is the ocean covariance matrix calculated for a region of the ocean and $E(\cdot)$ is the expectation operation over that region of the image, η is a threshold.

As in Eqn. 2.17, if the decision variable of the pixel is above the threshold, the pixel is considered from a ship. Otherwise, it belongs to the ocean.

Equation 2.17 is used for the determination of the decision variable for the coherent dual-pol systems (Quad-pol, LP, Cirp and CTLR) using appropriate definitions of the scattering vector X and the covariance matrix for each system. For the single-pol system the decision variable reduces to

$$L = \frac{|S_{i,j}|^2}{E(|S_{i,j}|_o^2)} \tag{2.18}$$

where $S_{i,j}$ is the scattering element of the single-pol system with i transmit and j receive polarization.

The decision variable for the RH-RV-PQHV hybrid system is developed by merging the decision variable of the coherent CTLR (RH-RV) system with the single-pol PQHV as in Eqn. 2.19. This system is called the merged CP detector.

$$L = X^H C_o^{-1} X + \frac{|S_{PQHV}|^2}{E(|S_{PQHV}|_o^2)} \tag{2.19}$$

where, C_o is the 2×2 ocean covariance matrix of the RH-RV coherent system and $X = [S_{RH} \ S_{RV}]$ is the scattering vector of the CTLR system.

For the PQ data, one should recall that the reconstruction algorithm can only reproduce the amplitude of the two co-pol components, their relative phase and only the HV amplitude. In this situation, it is considered that the full PQ system is composed of two systems: the HH-VV coherent dual-pol system and the HV single-pol system. The decision variable for this system can be then formulated by merging the decision variable of the coherent dual-pol system and that of the single-pol system [81] as in Eqn. 2.19 with using the scattering vector of the PQ HH-VV system, i.e. $X = [S_{PQHH} \ S_{PQVV}]$.

After the calculation of the decision variable for all pixels in the image, the decision variable is compared to a threshold for ship detection. This threshold is specified at a desired PFA. If the decision variable exceeds the threshold, the pixel is a ship; otherwise it

is ocean.

Before applying the LRT detector on the LP, CirP and the CTLR data, the data are spatially averaged with a 3×3 boxcar filter. The averaging is performed on the Hermitian product of the scattering components (i.e. $S_i.S_j^*$) used in calculating the decision variable for each SAR system and not on the complex scattering components. This is done to achieve a fair comparison with the PQ data since the reconstruction algorithm operates on the spatially averaged CTLR covariance matrix (which is averaged with same 3×3 boxcar filter) to produce the PQ data.

2.2.5 Detection Performance Assessment

In this study, the detection performance of the LRT algorithm is reported using two approaches. The first approach is the ROC curves. The ROC curve is a relation between the probability of missed detection (PMD) and the probability of false alarm (PFA) at various threshold values [19], [74].

To compute the PFA, a subset of the ocean with no targets is selected. Then the decision variables for each pixel in the selected ocean-only region are calculated. The decision variables are compared to a set of thresholds. For each threshold, if the decision variable is larger than the threshold, the pixel is considered a false alarm. To form the PFA at each threshold, the number of false alarms is divided by the total number of selected ocean pixels as in Eqn. 2.21.

For the same set of thresholds, the probability of detection (PD) values are computed as follows: first, one ship is selected from the image and the decision variable for each ship pixel is compared to the threshold. When the decision variable is higher than the threshold, the pixel is considered a detected pixel. The PD is computed by dividing the number of detected pixels by the total number of ship pixels and the PMD is calculated using Eqn. 2.20.

For the generation of the ROC curves, the thresholds can be set arbitrarily. In this study, all distinct values of ocean decision variables are used as thresholds. The PFA and the PMD

are calculated at each threshold value and the ROC is then generated using the (PFA, PMD) pairs.

$$PMD = 1 - \frac{N_D}{N_S} \tag{2.20}$$

$$PFA = \frac{N_{FA}}{N_o} \tag{2.21}$$

N_D is the number of detected pixels, N_S is the total number of a ship samples, N_{FA} is the number of false alarms, and N_o is the total number of ocean samples in a specified area.

The second approach of detection performance assessment is taking a section of the ROC curve at a specified PFA and record the corresponding PMD. The system with the lowest PMD is the one with the highest performance.

2.3   Conclusion

In this chapter, the methods used for the investigation of ship detection performance for a number of Radarsat-2 beam modes and SAR systems were introduced. Moreover, the data and study site were presented. This study is performed on SAR data with fine, medium and low resolution. In this work, the ship detection performance of compact polarimetric SAR systems is compared to linear dual polarimetric and circular transmit- circular receive polarimetric SAR systems. The CP systems involved are in the form of the RH-RV SAR and the reconstructed quad-pol data from the CP SAR. The reconstruction is performed using Collins reconstruction algorithm which is reviewed in this chapter. The LRT detection algorithm is used for ship detection in the SAR data. The detection performance is assessed using the ROC curves and the PMD at a specific PFA. The impact of resolution, beam incidence angle and ship orientation on the detection performance is investigated. Results and conclusions of this study are presented in Chapter 3.

Chapter 3

Ship Detection Performance Analysis of Compact Polarimetric Data

Results and Discussion

In this chapter, the results of applying the strategy presented in Chapter 2 to investigate the ship detection performance of compact polarimetry SAR systems are introduced. After the results are discussed, conclusions are accordingly made. This chapter is organized as follows. Section 3.1 outlines the results of the study. This section includes two subsections: subsection 3.1.1 which introduces the study results of the FQ data and subsection 3.1.2 which presents the results of the RCM data. Finally, section 3.2 concludes the findings of this chapter's work.

3.1 Results

3.1.1 Fine Quad Beam Mode Results

The summarized detection performance results of the Fine Quad beam mode are presented in Table 3.1. The table shows the median PMD values for each SAR system (detector) at a PFA of 10^{-5}. The table is organized so that the first column lists the orientation of the observed ships in degrees measured from the range direction and the other columns represent SAR detectors. The remainder columns are divided into three sets separated by vertical lines. The first set is for the CP systems (RH-RV, RH-RV-PQHV, Full PQ, PQHH-VV and PQHV). The second set is for the CirP (RR-RL) system and the third set is for the LP systems (HH-HV, VV-VH, HH-VV dual-pol and the quad-pol system). The table is also organized into five sections according to incidence angle, from the steepest incidence angle beam (B2: $19.77° − 21.78°$) at the top to the shallowest beam (B21: $40.17° − 41.61°$) at the

bottom. Each beam section contains ships identified in all scenes acquired with that beam. Within each section, the rows refer to ships at a particular orientation category, from 0° at the top to 90° at the bottom. At each orientation, table entries refer to the median PMD taken over the number of ships belong to that orientation. The last row of each section refers to median PMD taken over all the ships in all scenes of that beam. The lowest PMD (best performance) is shaded in dark grey. In cases where the lowest PMD was achieved with the quad-pol data, the next lowest non-quad-pol detector is shaded in dark grey. Detectors with performance within 0.02 of the lowest PMD are shaded with lighter grey. As mentioned previously, we expect enhanced performance (lower PMD) at 0° and 90°. So, the lowest PMD results per each SAR detector are indicted in bold face font as evidence of this effect.

The discussion in this section has three sides :

A. the effect of incidence angle on ship detection performance of SAR detectors.

B. the impact of ship orientation on the detectability of ships.

C. A comparison between the CP, CirP and LP systems detection performance.

A. Incidence Angle Impact

The first discussion is the performance of the detectors as the incidence angle increases from B2 to B21, an increase in the incidence angle of almost 22°. This relation can be seen clearly from Figure 3.1 which depicts the relationship between the overall median PMD over all ships per each beam at PFA of 10^{-5} for all detectors and the mean incidence angle for the available beam modes (B2-B21).

For CP detectors, it is found that the PQHV detector performance fluctuates at low incidence angles and then the performance improves as the incidence angle increases with a spike in its weakest performance at B4 and the best detection performance at B21. For the merged CP detector, the performance remains steady between B2 and B4 and then it improves with the best performance occurring at B21. For the CirP and all other PQ detectors, the detection performance improves as the incidence angle increases and its best
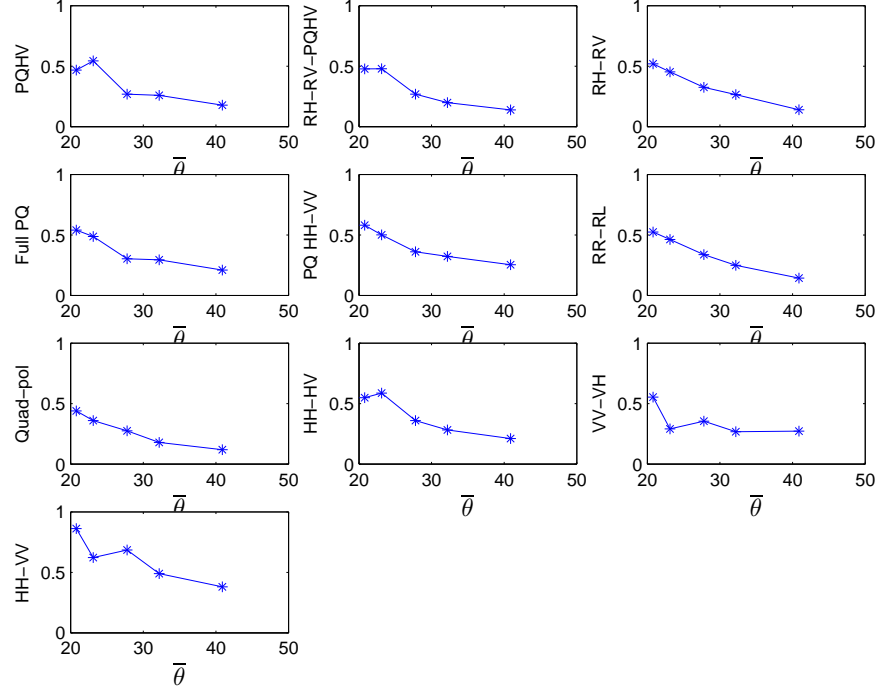
Figure 3.1: *Fine Quad beam mode* : overall median PMD for all ships within each beam at PFA of 10^{-5} for all CP, CirP and LP detectors as a function of the mean incidence angle ($\bar{\theta}$) at the range ($19.78° - 41.61°$). It is obvious that the strongest performance occurs at the shallowest incidence angle (B21) and the weakest performance occurs either at B2 or B4. However, the detection performance generally improves as the incidence angle increases for all detectors.

performance occurs at B21. The detection performance of the quad-pol detector improves gradually with the increase of the incidence angle. The LP HH-VV and LP VV-VH detectors performance improves between B2 and B4 and then fluctuates between B4 and B12. For the LP HH-VV, the performance then improves at B21 while for the LP VV-VH, the performance remains nearly steady between B12 and B21. For the LP HH-HV, the detection performance slightly deteriorates between B2 and B4 and then it improves with incidence angle increase. However, it is obvious that the detection performance generally improves as the incidence angle increases for all detectors with the strongest performance occurs at the shallowest incidence angle (B21).

B. Ship Orientation Impact

In order to shed light on the effect of ship orientation on the detection performance, the lowest PMD value of each detector is indicated in bold face font in Table 3.1. This is done at each incidence angle range (beam). We notice that the best performance at shallow incidence beams (B12, B21) occurs at the 0° orientation while for steep incidence bems (B2, B4), the lowest PMD mostly occurs at 90° orientation.

We can see that the NLPOP at the 90° orientation is 24% while the lowest PMD occurs at the 0° orientation for about 50% of the cases. This means that the lowest PMD still occurs at either 90° or the 0° orientations for about 74% of the cases as expected. For the remaining 26% of the cases, the lowest PMD occurs at other orientation angles without a clear trend.

C. Detection Performance of SAR Systems

Now we come to the comparison of the LP, CirP, PQ and CTLR detectors performance. For the steepest B2 beam, the highest median performance over all ships is achieved by the quad-pol detector followed by the PQHV and then the merged CP detector. However, over the various orientations, the best performance swings between the CP detectors with the merged CP detector is the best non quad-pol detector for 3 out of the five orientation categories. For the B4 beam, the overall best performance is occupied by either the LP HH-HV or LP VV-VH dual-pol over the orientation categories except for 0° where the best performer is the CirP detector. For the B8 beam mode, the best performance is for the PQHV at most orientations and over all ships within this beam followed by the merged CP detector. At the B12 beam, the best detector at all the orientations except two and over all ships is the quad-pol detector. At 0° orientation, the PQHV is the best detector followed closely by the merged CP detector. At 90° orientation, the native CTLR detector has the highest performance followed by the quad-pol. Over all ships in this beam, the highest performance is for the quad-pol followed by the merged CP detector. For the B21 beam,

Table 3.1: *Fine Quad beam mode*: median probability of missed detection (PMD) for several ships at a fixed probability of false alarm (PFA) of 10^{-5}. The leftmost column is the orientation of the observed ship in degrees measured from the range direction of the radar, i.e. if the ship is oriented along the range direction, its orientation is $0°$, while if it is oriented along the satellite track, its orientation is $90°$. The orientation angles are subscripted with the number of ships used in the estimate. The lowest PMD (best performance) is shaded in dark grey. In cases where the lowest PMD was achieved with the quad-pol data, the next lowest non-quad-pol detector is shaded in dark grey. Detectors with performance within 0.02 of the lowest PMD are shaded with a lighter grey. For each SAR detector, the lowest PMD is indicated with bold face font. The last row in each section is the overall median taken over the total number of ships within this beam (Tot.).

Ship Orient^n (deg)	PQHV	RH-RV-PQHV	RH-RV	Full PQ	PQHH-VV	RR-RL	HH-HV	VV-VH	HH-VV	Quad-pol
B2 $19.78° - 21.78°$										
0^4	**0.296**	0.273	0.346	0.367	0.504	0.358	**0.282**	**0.376**	0.854	**0.217**
30^7	0.466	0.433	0.517	0.449	0.511	0.464	0.615	0.589	0.807	0.433
45^7	0.487	0.603	0.626	0.603	0.639	0.628	0.613	0.641	0.950	0.592
60^3	0.627	0.594	0.596	0.609	0.707	0.598	0.641	0.637	0.833	0.609
90^2	0.415	**0.216**	**0.183**	**0.192**	**0.190**	**0.184**	0.355	0.514	**0.479**	0.226
Tot. = 23	0.469	0.477	0.519	0.540	0.580	0.524	0.549	0.553	0.862	0.439
B4 $22.16° - 24.08°$										
0^6	**0.410**	0.367	0.337	0.340	0.353	0.327	0.394	0.395	0.552	0.331
30^9	0.624	0.467	0.431	0.476	0.476	0.466	0.275	0.272	0.755	0.359
45^6	0.658	0.569	0.537	0.608	0.635	0.569	0.384	0.388	0.668	0.457
60^8	0.510	0.502	0.467	0.541	0.558	0.496	**0.244**	**0.245**	0.714	0.372
90^2	0.588	0.371	**0.320**	**0.339**	**0.339**	**0.297**	0.282	0.277	**0.526**	**0.286**
Tot. = 31	0.544	0.479	0.453	0.487	0.501	0.463	0.286	0.290	0.622	0.359
B8 $26.88° - 28.71°$										
0^3	0.302	0.290	0.377	0.341	0.377	0.372	0.403	0.396	0.620	0.323
30^5	**0.165**	**0.183**	**0.253**	**0.220**	**0.288**	**0.249**	**0.291**	**0.287**	**0.612**	**0.181**
45^5	0.301	0.295	0.328	0.318	0.363	0.338	0.369	0.364	0.671	0.315
60^4	0.288	0.308	0.369	0.345	0.384	0.392	0.357	0.348	0.717	0.305
90^5	0.271	0.281	0.338	0.323	0.356	0.336	0.385	0.383	0.697	0.296
Tot. = 22	0.268	0.269	0.325	0.303	0.360	0.337	0.359	0.354	0.685	0.275
B12 $31.34° - 33.03°$										
0^2	**0.057**	**0.067**	**0.100**	**0.107**	**0.131**	**0.098**	**0.146**	**0.154**	**0.275**	**0.075**
30^1	0.323	0.329	0.339	0.350	0.388	0.324	0.371	0.377	0.490	0.315
45^4	0.263	0.273	0.346	0.363	0.426	0.323	0.375	0.363	0.551	0.240
60^2	0.310	0.227	0.251	0.219	0.239	0.276	0.219	0.230	0.634	0.185
90^2	0.197	0.189	0.111	0.276	0.269	0.242	0.305	0.263	0.559	0.179
Tot. = 11	0.259	0.198	0.265	0.294	0.322	0.249	0.282	0. 267	0.490	0.179
B21 $40.17° - 41.61°$										
0^{10}	**0.097**	**0.065**	**0.074**	**0.094**	**0.150**	**0.078**	**0.163**	0.193	**0.215**	**0.067**
30^8	0.208	0.152	0.160	0.217	0.280	0.183	0.177	0.200	0.420	0.113
45^8	0.255	0.202	0.202	0.272	0.298	0.203	0.276	0.335	0.353	0.176
60^5	0.158	0.127	0.139	0.164	0.207	0.144	0.181	**0.188**	0.299	0.122
90^7	0.280	0.213	0.181	0.283	0.317	0.143	0.240	0.296	0.501	0.143
Tot. = 38	0.177	0.138	0.140	0.209	0.254	0.143	0.211	0.272	0.380	0.118

the quad-pol detector is the highest performance detector aver all orientations except for 0°
where the best performer is the merged CP detector. The best non quad-pol performer is the
merged CP detector for all orientations except 90° where the CirP is the best non quad-pol
performer. The quad-pol detector has the highest median PMD over all ships within this
beam mode followed by the merged CP detector and then the CTLR detector. It is also
noticed that the CirP detector has a close performance to the merged CP detector for all
orientations except one and over all ships.

Now the detection performance is discussed in terms of the overall median PMD as a
function of the PFA for all ships in a specific beam mode regardless of their orientation angles
for all LP, CirP and CP detectors. Figure 3.2 shows the overall median ROC curves for all
ships in the five Fine Quad beam modes. In the ROC curves, the detector with lower median
PMD has better performance (the lower the curve, the better the detector performance).

For the B2 ROC curves in Figure 3.2, we notice that the PQHV detector outperforms all
other detectors for PFA values up to 4×10^{-5} followed by the quad-pol detector. For lower
PMD values, the quad-pol detector outperforms all other detectors followed by the PQHV
performance and then the merged CP detector performance. The LP HH-HV and LP VV-
VH detectors perform better than the CTLR, the RR-RL and the Full PQ detectors for
high PFAs. On the other hand, at lower PFAs, the performance of these detectors becomes
comparable. The CirP and the CTLR CP detectors have comparable performance with the
CirP performs slightly better for high PFA values. The worst detection performance over
the entire PFA range is for the PQHH-VV detector.

For the B4 beam ROC curves in Figure 3.2, we can see that for high PFA values, the
best detector is the quad-pol followed so closely by both the LP HH-HV and the LP VV-
VH detector. At high PFAs, the PQHV and the merged CP detectors share nearly the
same moderate performance while the PQHH-VV and the Full PQ detectors have lower
performance. For low PFA values, we notice that the highest performance detectors are both
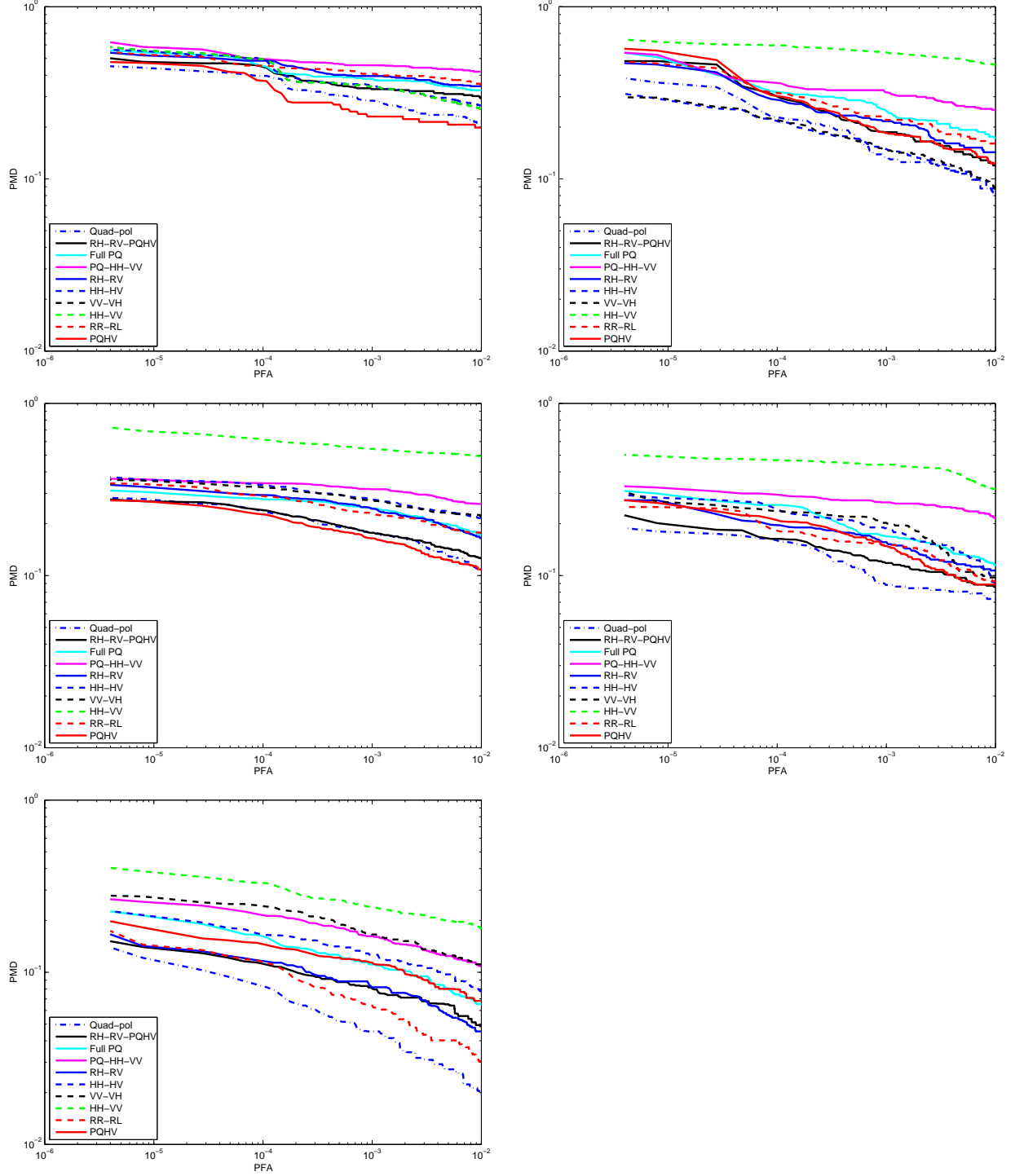
Figure 3.2: *Fine Quad beam mode*: overall median ROC curves for all ships with all orientations acquired by each of the incidence angle range for the Fine Quad beam imaging mode. Top left: B2 (19.77° − 21.78°). Top right: B4 (22.16° − 24.08°). Middle left: B8 (26.88° − 28.71°). Middle right: B12 (31.34° − 33.03°). Bottom left: B21 (40.17° − 41.61°).

the LP HH-HV and the LP VV-VH detectors followed by the quad-pol detector. The rest of the CP detectors (CTLR, PQHH-VV and merged CP detector) and the CirP detector have close detection performance except the PQHV detector which is the second worst performer for low PFA values. Clearly, the LP HH-VV occupies the worst performance over the entire PFA range.

For the B8 beam, one can see from Figure 3.2 that the PQHV detector outperforms all other detectors over the entire PFA range followed closely by the quad-pol detector and then by the merged CP detector. The CTLR, CirP and the Full PQ detectors have intermediate performance and the PQHH-VV, LP HH-HV and LP VV-VH detectors share a moderate performance for high PFAs. The LP HH-VV is the worst detector over the entire PFA range.

For the B12 beam, one can see that the quad-pol detector is the best detector over the entire PFA range. The merged CP detector has the second best performance for nearly the entire PFA range. The CTLR, the CirP and the PQHV detectors have a comparable performance that is better than that of the LP HH-HV and LP VV-VH for medium to low PFA values. The CirP detector has the third best performance for the PFA range from 8×10^{-5} to 10^{-3} and from 10^{-5} to 3×10^{-6}. The LP HH-VV detector has the worst detection performance and the PQHH-VV detector has the second worst performance over the entire PFA range.

For the B21 beam, the quad-pol detector has the best performance over the entire PFA range. The second best performance is shared by the native CTLR, the CirP and the merged CP detector for PFA values lower than 10^{-4} and up-to 10^{-5}. For higher PFAs, the CirP detector is the second best performer followed by both the CTLR and the merged CP detector. The PQHV detector performs better than the Full PQ detector for low PFAs while they have comparable performance for higher PFAs. The LP HH-VV is the worst detector followed by the LP VV-VH detector over the entire PFA range.

To summarize, one can see that for low incidence angles (B2), medium incidence beams

(B8 and B12) and shallow incidence beam (B21), generating PQHV has an advantage for ship detection as either the PQHV itself or when added to the native CTLR detector outperforms other detectors. For the B21 beam, we also see that the CTLR shares the merged CP detector best performance for low PFA. However, it is suggested that its performance deteriorates for PFA less than 10^{-5} while that of the merged CP detector will remain steady. Over all incidence angle categories, one can see that the CirP has a comparable performance to the CTLR. However, the CirP detector starts to have a higher performance for high PFA at the B12 and B21 beams. For B4, it is noticed that the LP detectors outperform all other detectors. So, generally, it is obvious that CP detectors, either raw CTLR or PQ detectors, outperform LP dual-pol detectors for medium to shallow incidence angles.

3.1.2   RCM Results

Here, the results of the detection performance of the RCM imaging modes are summarized in three tables, one table for each RCM mode: Table 3.2 for the Medium Resolution mode, Table 3.3 for the Low Resolution mode and Table 3.4 for the Ship Detection mode. These tables show the median PMD values for each SAR system (detector) at a PFA of 10^{-5}. Each table is organized so that the first column lists the orientation of the observed ships in degrees measured from the range direction, the last column shows the type of the system with the highest performance (H.Pr.)–lowest PMD: LP, CirP or CP and the other columns represent SAR detectors. These columns are divided into three sets separated by vertical lines. The first set is for the CP systems (RH-RV, RH-RV-PQHV, Full PQ, PQHH-VV and PQHV). The second set is for the CirP system and the third set is for the LP systems (HH-HV, VV-VH, HH-VV) dual-pol system. Tables 3.2 and 3.3 only are organized into five horizontal sections according to the incidence angle range (the beam), from the steepest incidence angle beam (B2: $19.77° − 21.78°$) at the top to the shallowest beam (B21: $40.17° − 41.61°$) at the bottom. Each beam section contains ships identified in all scenes acquired with that beam mode. Within each section, the rows refer to ships at a particular orientation

category, from 0° at the top to 90° at the bottom. At each orientation category, table entries refer to the median PMD taken over the number of ships with the corresponding orientation. The last row in each section refers to the median PMD taken over all the ships in all scenes of that beam mode. The lowest PMD (best performance) is shaded in dark grey. Detectors with performance within 0.02 of the lowest PMD are shaded with a lighter grey. As aforementioned, we expect enhanced performance (lower PMD) at 0° and 90°. So, the lowest PMD results per each SAR detector are indicted in bold face as evidence of this effect. Table 3.4 will be described later on in this chapter.

The discussion in this section has three sides for each RCM beam mode:

A. the effect of incidence angle on ship detection performance of SAR detectors.

B. the impact of ship orientation on the detectability of ships regardless of the resolution of the beam mode.

C. a comparison between the the CP, CirP and LP systems detection performance.

Medium Resolution RCM Beam Mode Results

A. Incidence Angle Impact

The graphics in Figure 3.3 depict the relationship between the overall median PMD over all ships for each beam at PFA of 10^{-5} for each detector and the mean incidence angle for the available beam modes (B2-B21). This figure shows that all dual-pol detectors have their weakest performance at the steepest incidence angle beam (B2).

The weakest detector for this beam mode, and overall detectors, was the LP HH-VV detector. These graphs show that detection performance increases (the median PMD decreases) as the incidence angle increases from the B2 ($\overline{\theta} = 20.78°$) beam to the B12 ($\overline{\theta} = 32.19°$) beam. The exception to this general observation is that the performance of the PQHV detector deteriorates slightly from beam B8 to B12.
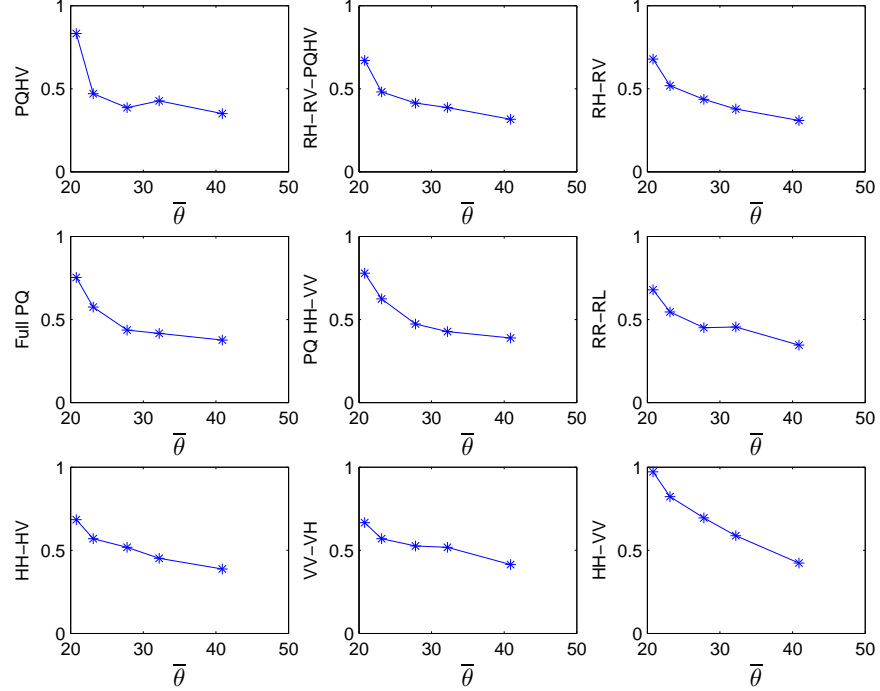
Figure 3.3: *Medium Resolution RCM mode* : overall median PMD for all ships within each beam at PFA of 10^{-5} for all CP, CirP and LP detectors as a function of the mean incidence angle at the range $(19.78° - 41.61°)$. The first two rows show the plots for the CP and CirP detectors and the third row is for the LP detectors. It is clear that the detection performance generally improves as the incidence angle increases for all detectors with the strongest performance occurring at the shallowest incidence angle (B21) and the weakest performance occurring at the steepest incidence angle (B2).

B. Ship Orientation Impact

In order to shed light on the effect of ship orientation on the detection performance, the lowest PMD value for each detector is indicated in bold face font in Table 3.2, 3.3 and, 3.4. This is done for each incidence angle range.

The effect of ship orientation on detection performance dos not show a clear trend for the two steepest beam modes. While several detectors have their strongest performance for ships at 90° at B2, several others have their strongest performance for ships at 45°. The situation is comparable at B4, except fewer have their strongest performance at 90°. At B8, every detector has their strongest performance at 0°, while at B12, every detector has their strongest performance at 90°. For the shallowest beam (B21), the lowest PMD occurs for

ships between 60° and 90°.

The NLPOP at 90° orientation is 46.67% while the lowest PMD occurs at the 0° orientation for 20% of the cases. This means that the lowest PMD still occurs at either 90° or 0° orientations for about 66% of the cases in this RCM mode which is consistent with our expectations.

For the remaining 34% of the cases, the lowest PMD occurs in 17.78% of the cases only at low incidence angle beams at 45° orientation. However, for the remaining cases, the lowest PMD occurs at either 30° or 60° orientation without any clear trend.

C. Detection Performance of SAR Systems

Table 3.2 shows that the performance of the CP, CircP, and LP detectors vary with ship orientation at incidence angles between 20° and 24°, and there is no clear advantage to CP over LP. At 27° incidence (B8), the reconstructed HV detector (PQHV) has the strongest performance, slightly better than when paired with the two raw CP channels. For the two steeper beams (B12 and B21), the raw CP channels have the strongest performance, and there is no advantage to performing the linear reconstruction, as neither the full PQ nor the addition of the reconstructed HV to RH-RV, improves the performance. Thus at incidence angle greater than 30° there is a clear advantage to the dual-pol CP polarization.

Figure 3.4 provides the ROC curves for the five beam modes shown in Table 3.2. These graphs show the detection performance in terms of the overall median PMD as a function of the PFA for all ships within each beam for all orientation angles for each of the LP, CirP and CP detectors. For incidence angle between 20° and 24° (beams B2 and B4) we can see that there is a sharp drop in performance for the CP detectors between 10^{-3} and 10^{-4} PFA. At the steepest beam (B2), below this performance drop, the highest performers are the reconstructed HV detector, the raw RH-RV and their combination. As the PFA drops, the performance of the PQHV detector deteriorates significantly. The RH-RV detector, also deteriorates but remains stronger than all other detectors, except LP VV-VH. However,

Table 3.2: *Medium Resolution RCM mode*: median probability of missed detection (PMD) for several ships at a fixed probability of false alarm (PFA) of 10^{-5}. The leftmost column is the orientation of the observed ship in degrees estimated from the range direction of the radar. The orientation angles are subscripted with the number of ships used in the estimate. The lowest PMD (highest performance) is shaded in dark grey. Detectors whose performance is within 0.02 of the lowest PMD, are shaded in a light grey. Within each beam, the ship orientation that generated the lowest PMD is indicated with bold face font. The last row in each beam section is the overall median taken over the total number of ships within this beam (Tot.).

Ship Orient^{n} (deg)	PQHV	RH-RV-PQHV	RH-RV	Full PQ	PQHH-VV	RR-RL	HH-HV	VV-VH	HH-VV	H.Pr.
B2 : $19.78^{\circ} - 21^{\circ}$										
0^{4}	0.774	0.668	0.679	0.719	0.765	0.691	0.745	0.733	0.958	CP
30^{7}	0.908	0.845	0.896	0.896	0.896	0.896	0.842	0.745	0.942	LP
45^{7}	**0.640**	0.621	0.583	0.714	0.721	0.585	**0.613**	**0.617**	0.987	CP
60^{3}	0.835	0.872	0.964	0.998	0.998	0.963	0.661	0.661	0.948	LP
90^{2}	0.903	**0.587**	**0.583**	**0.572**	**0.573**	**0.582**	0.658	0.635	**0.727**	CP
Tot. = 23	0.832	0.670	0.678	0.753	0.779	0.678	0.684	0.666	0.972	LP
B4 : $22.16^{\circ} - 24.08^{\circ}$										
0^{6}	0.565	0.622	0.647	0.679	0.707	0.646	0.625	0.632	0.778	CP
30^{9}	0.428	0.456	0.475	**0.529**	0.571	0.484	0.552	0.552	**0.743**	CP
45^{6}	**0.409**	**0.420**	**0.445**	0.543	0.584	**0.449**	0.603	0.610	0.806	CP
60^{8}	0.675	0.706	0.730	0.757	0.789	0.731	0.629	0.624	0.929	LP
90^{2}	0.633	0.533	0.536	0.558	**0.563**	0.548	**0.543**	0.533	0.747	CP & LP
Tot. = 31	0.470	0.481	0.518	0.575	0.624	0.545	0.570	0.570	0.823	CP
B8 : $26.88^{\circ} - 28.71^{\circ}$										
0^{3}	**0.260**	**0.277**	**0.350**	**0.375**	**0.411**	**0.415**	**0.470**	**0.482**	**0.613**	CP
30^{5}	0.386	0.417	0.445	0.454	0.504	0.496	0.519	0.522	0.668	CP
45^{5}	0.468	0.488	0.529	0.525	0.562	0.531	0.540	0.559	0.749	CP
60^{4}	0.377	0.401	0.421	0.454	0.422	0.441	0.506	0.528	0.698	CP
90^{5}	0.391	0.422	0.466	0.472	0.510	0.478	0.559	0.563	0.694	CP
Tot. = 22	0.386	0.414	0.463	0.436	0.473	0.450	0.518	0.526	0.695	CP
B12 : $31.34^{\circ} - 33.03^{\circ}$										
0^{2}	0.438	0.400	0.399	0.444	0.458	0.496	0.476	0.537	0.545	CP
30^{1}	0.528	0.514	0.506	0.508	0.538	0.569	0.544	0.569	0.629	CP
45^{4}	0.479	0.456	0.449	0.486	0.502	0.534	0.504	0.532	0.601	CP
60^{2}	0.403	0.313	0.305	0.306	0.312	0.352	0.333	0.353	0.623	CP
90^{2}	**0.219**	**0.211**	**0.114**	**0.301**	**0.284**	**0.293**	**0.304**	**0.324**	**0.428**	CP
Tot. = 11	0.427	0.387	0.378	0.416	0.427	0.455	0.452	0.518	0.588	CP
B21 : $40.17^{\circ} - 41.61^{\circ}$										
0^{10}	0.342	0.293	0.285	0.365	0.370	0.292	0.320	0.361	0.350	CP
30^{8}	0.334	0.315	0.311	0.328	0.333	0.325	0.356	0.406	0.393	CP
45^{8}	0.411	0.385	0.379	0.426	0.433	0.399	0.436	0.500	0.465	CP
60^{5}	**0.317**	0.289	0.278	**0.303**	**0.303**	0.278	0.306	**0.331**	**0.345**	CP & CirP
90^{7}	**0.317**	**0.261**	**0.242**	0.318	0.325	**0.256**	**0.300**	0.429	0.359	CP
Tot. = 38	0.350	0.316	0.309	0.376	0.389	0.346	0.387	0.414	0.423	CP
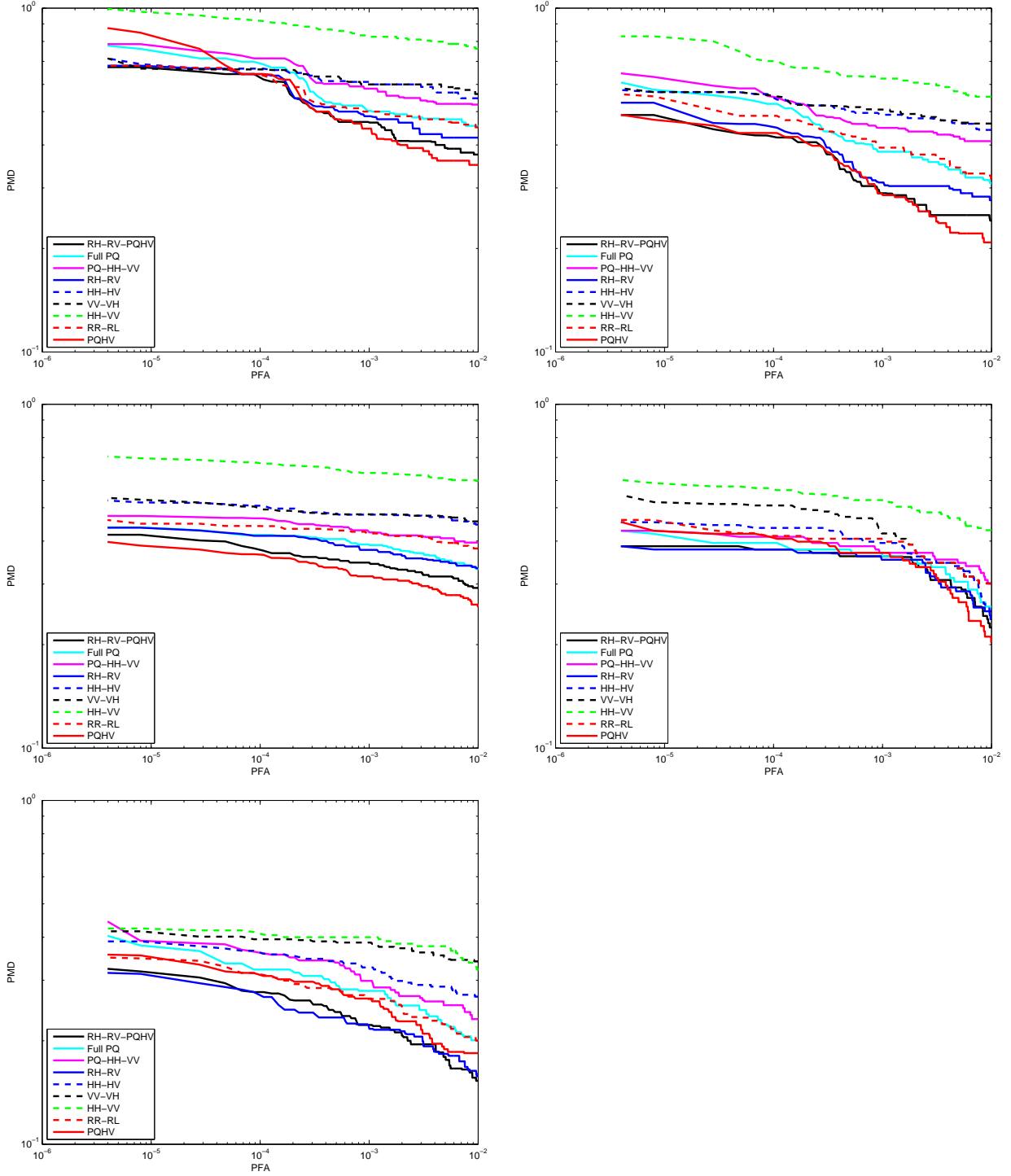
Figure 3.4: *Medium Resolution RCM mode*: overall median ROC curves for all ships with all orientations acquired by each of the incidence angle range for the simulated RCM Medium Resolution imaging mode. Top left: B2 ($19.77° − 21.78°$). Top right: B4 ($22.16° − 24.08°$). Middle left: B8 ($26.88° − 28.71°$). Middle right: B12 ($31.34° − 33.03°$). Bottom left: B21 ($40.17° − 41.61°$).

there is a suggestion that below a PFA of 10^{-5}, the LP VV-VH detector starts to weaken, while the RH-RV remains steady. The situation is very similar in the B4 beam, except that even after the drop in performance of these three detectors (PQHV, RH-RV, merged CP detector), they remain stronger than any of the others. At this slightly shallower incidence angle it appears there is some advantage in combining the RH-RV with the PQHV.

The ROC curve for the B8 beam carries the same message as the tabulated results. The reconstructed HV detector has the strongest performance, slightly better than when in combination with RH-RV. For beam B12, the reconstructed HV detector is quite strong below a PFA of 10^{-3}. The RH-RV detector has slightly weaker performance with no apparent advantage of adding PQHV. For lower PFA values, the RH-RV detector and the merged CP detector share the best performance. At 41° (B21), the RH-RV detector has the highest performance for PFAs up to 10^{-3}, again, with no apparent advantage of calculating and adding the PQHV channel. On the other hand, for high PFA levels, adding the PQHV to the CTLR detector improves the detection performance.

Low Resolution RCM Beam Mode Results

A. Incidence Angle Impact

Figure 3.5 shows how the overall median PMD for each detector changes a function of the imaging beam incidence angle in the range $(19.75° - 41.61°)$ for the RCM Low Resolution mode. At this lower resolution the behaviour of the CP/CirP and LP detectors is quite different at the steeper incidence angles. The performance of the CP and CircP detector is similar at the two steepest incidence angle and then the performance improves significantly at B8, while the performance of the three LP detectors shows a fairly strong performance gain between B2 and B4. With the exception of HH-VV, which again has the weakest performance over all the detectors, the detection performance does not improve between B8 and B21, and in some cases, the performance actually deteriorates slightly. Thus, for the Low Resolution cases, the performance gains in observed ships at shallow incidence angles

68
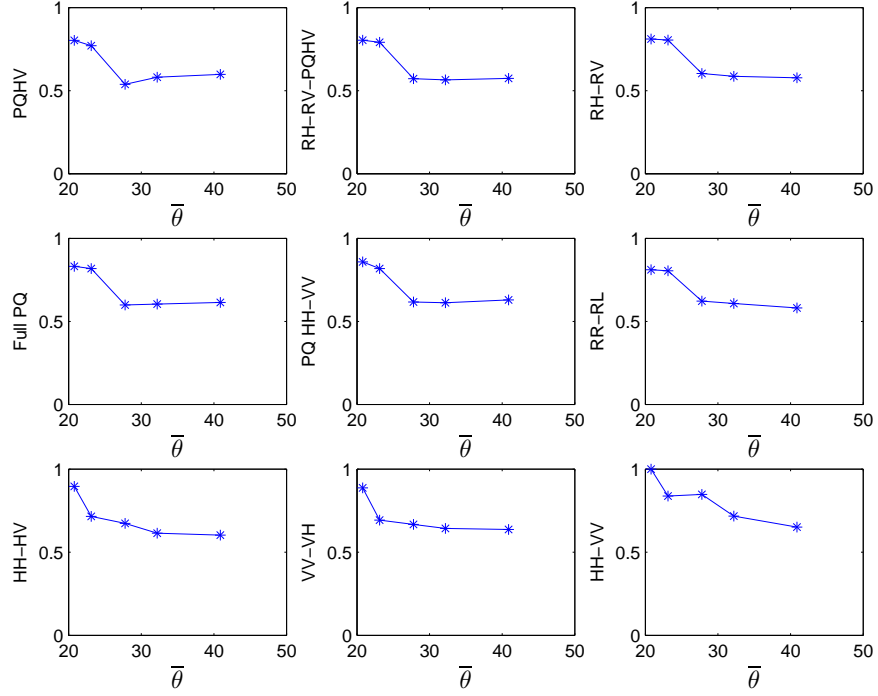
Figure 3.5: *Low Resolution RCM mode* : overall median PMD for all ships within each beam at PFA of 10^{-5} for all CP and FP detectors as a function of the mean incidence angle at the range $(19.78° - 41.61°)$. The first two rows show the plots for the CP and CirP detectors and the third row is for the LP detectors. It is noticed that the performance improves from B2 to B8 however, the performance gains at shallow incidence angles are more modest than for Medium Resolution.

Table 3.3: *Low Resolution RCM beam mode*: median probability of missed detection (PMD) for several ships at a fixed probability of false alarm (PFA) of 10^{-5}. The leftmost column is the orientation of the observed ship in degrees estimated from the range direction of the radar. The orientation angles are subscripted with the number of ships used in the estimate. The lowest PMD (highest performance) is shaded in dark grey. Detectors whose performance is within 0.02 of the lowest PMD, are shaded in a light grey. Within each beam, the ship orientation that generated the lowest PMD is indicated with bold face font. The last row in each beam section is the overall median taken over the total number of ships within this beam (Tot.).

Ship Orient^n (deg)	PQHV	RH-RV-PQHV	RH-RV	Full PQ	PQHH-VV	RR-RL	HH-HV	VV-VH	HH-VV	H.Pr.
B2 : $19.78° - 21°$										
0^4	0.839	0.840	0.849	0.863	0.875	0.866	0.884	0.881	0.996	CP
30^7	0.810	0.811	0.811	0.838	0.846	0.811	0.905	0.909	1.00	CP
45^7	0.829	0.847	0.847	0.873	0.891	0.847	0.889	0.886	1.00	CP
60^3	0.721	0.726	0.758	0.790	0.802	0.759	0.948	0.962	1.00	CP
90^2	**0.636**	**0.645**	**0.667**	**0.697**	**0.709**	**0.669**	**0.855**	**0.861**	**0.910**	CP
Tot. = 23	0.803	0.804	0.811	0.831	0.858	0.811	0.896	0.887	1.00	CP
B4 : $22.16° - 24.08°$										
0^6	0.763	0.787	0.823	0.825	0.825	0.808	0.717	0.685	0.759	LP
30^9	0.808	0.774	0.741	0.806	0.808	0.741	0.803	0.803	0.809	CP
45^6	**0.715**	0.722	0.764	0.812	0.821	0.763	0.691	0.710	0.853	LP
60^8	0.810	0.936	0.940	0.953	0.962	0.940	0.669	0.668	0.921	LP
90^2	0.786	**0.637**	**0.635**	**0.635**	**0.630**	**0.636**	**0.652**	**0.641**	**0.689**	CP
Tot. = 31	0.771	0.791	0.805	0.818	0.818	0.805	0.715	0.693	0.838	LP
B8 : $26.88° - 28.71°$										
0^3	0.510	0.545	0.577	0.587	0.607	0.627	0.669	0.665	0.759	CP
30^5	0.549	0.574	0.620	0.610	0.631	0.648	0.664	0.651	0.836	CP
45^5	0.616	0.610	0.643	0.627	0.661	0.685	0.716	0.719	0.873	CP
60^4	0.579	0.613	0.638	0.626	0.646	0.659	0.756	0.748	0.881	CP
90^5	**0.498**	**0.517**	**0.560**	**0.575**	**0.596**	**0.589**	**0.629**	**0.644**	**0.739**	CP
Tot. = 22	0.538	0.572	0.603	0.599	0.617	0.622	0.673	0.667	0.848	CP
B12 : $31.34° - 33.03°$										
0^2	0.614	0.594	0.597	0.613	0.615	0.644	0.663	0.713	0.788	CP
30^1	0.694	0.686	0.688	0.703	0.703	0.688	0.703	0.718	0.725	CP
45^4	0.627	0.612	0.620	0.652	0.688	0.633	0.667	0.687	0.729	CP
60^2	0.543	0.485	0.490	0.474	0.485	0.519	0.520	0.537	0.738	CP
90^2	**0.396**	**0.383**	**0.182**	**0.443**	**0.435**	**0.417**	**0.446**	**0.475**	**0.549**	CP
Tot. = 11	0.581	0.565	0.586	0.604	0.612	0.608	0.614	0.643	0.717	CP
B21 : $40.17° - 41.61°$										
0^{10}	0.594	0.565	0.569	0.609	0.619	0.564	0.573	0.620	0.617	CP
30^8	0.595	0.567	0.579	0.605	0.621	0.597	0.613	0.641	0.647	CP
45^8	0.641	0.611	0.607	0.644	0.650	0.632	0.648	0.684	0.660	CP
60^5	0.612	0.538	0.534	0.596	0.594	0.524	0.512	0.637	0.542	LP
90^7	**0.469**	**0.434**	**0.425**	**0.490**	**0.490**	**0.452**	0.514	0.629	0.551	CP
Tot. = 38	0.598	0.574	0.577	0.614	0.629	0.581	0.603	0.637	0.651	CP

are more modest than for Medium Resolution. Nevertheless, there is still a clear advantage in observed ships at incidence angles at a minimum of 28°.

B. Ship Orientation Impact

In this beam mode, by calculating the percentage of the cases in which the lowest PMD occurs at each orientation angle (the NLPOP), it has been found that for 91.11% of the cases, the lowest PMD occurs at the 90° orientation. In about 2.22% of the cases (one case only), the lowest PMD occurs at the 0° orientation while in the rest of the cases, the lowest

PMD occurs at the other orientations without clear trend.

C. Detection Performance of SAR Systems

In this low resolution RCM mode, one can see from Table 3.3, that the detection performance is slightly more variable than in the Medium Resolution data. For the Low Resolution data, the strongest detector for the B2 and B8 beams is the PQHV. The B4 beam had variable results with the standard linear dual-pol detectors have generally stronger performance than the CirP and CP detectors.

For the two shallower beams, the results are more variable than in the Medium Resolution case, but the trend is similar. The raw RH-RV detector with and without the combination of the reconstructed HV has the strongest performance. It is also noticed that the highest performance over all beams occurs at B8 by the PQHV detector. Adding PQHV to the RH-RV data seems to strengthen the detector more for low resolution data. Overall, the CP detectors significantly outperform the linear dual-pol and the CirP detectors as was the case in the Medium Resolution data.

Figure 3.6 shows the ROC curves for the five beams simulated in the RCM Low Resolution mode, and allows us to explore the detection performance as a function of the PFA. For the lowest incidence angle, B2, one can see that the PQHV has the strongest performance for all PFAs, except for a section where the combination with RH-RV is an advantage. This is the case with the B8 beam as well - the PQHV detector had the strongest performance across all levels of PFA.

The B4 results seem to be an anomaly. The performance of the CP detectors is strong up to a PFA of 10^{-4}, after which they deteriorate significantly. For lower PFA levels, at this incidence, the two coherent linear dual-pol detectors have the strongest performance.

For the two shallow beams the raw RH-RV detector, with and without PQHV, has the strongest performance across all levels of PFA. It appears that at the lowest PFA, the RH-RV detector begins to fall off, and the addition of PQHV maintains the strength of this

71
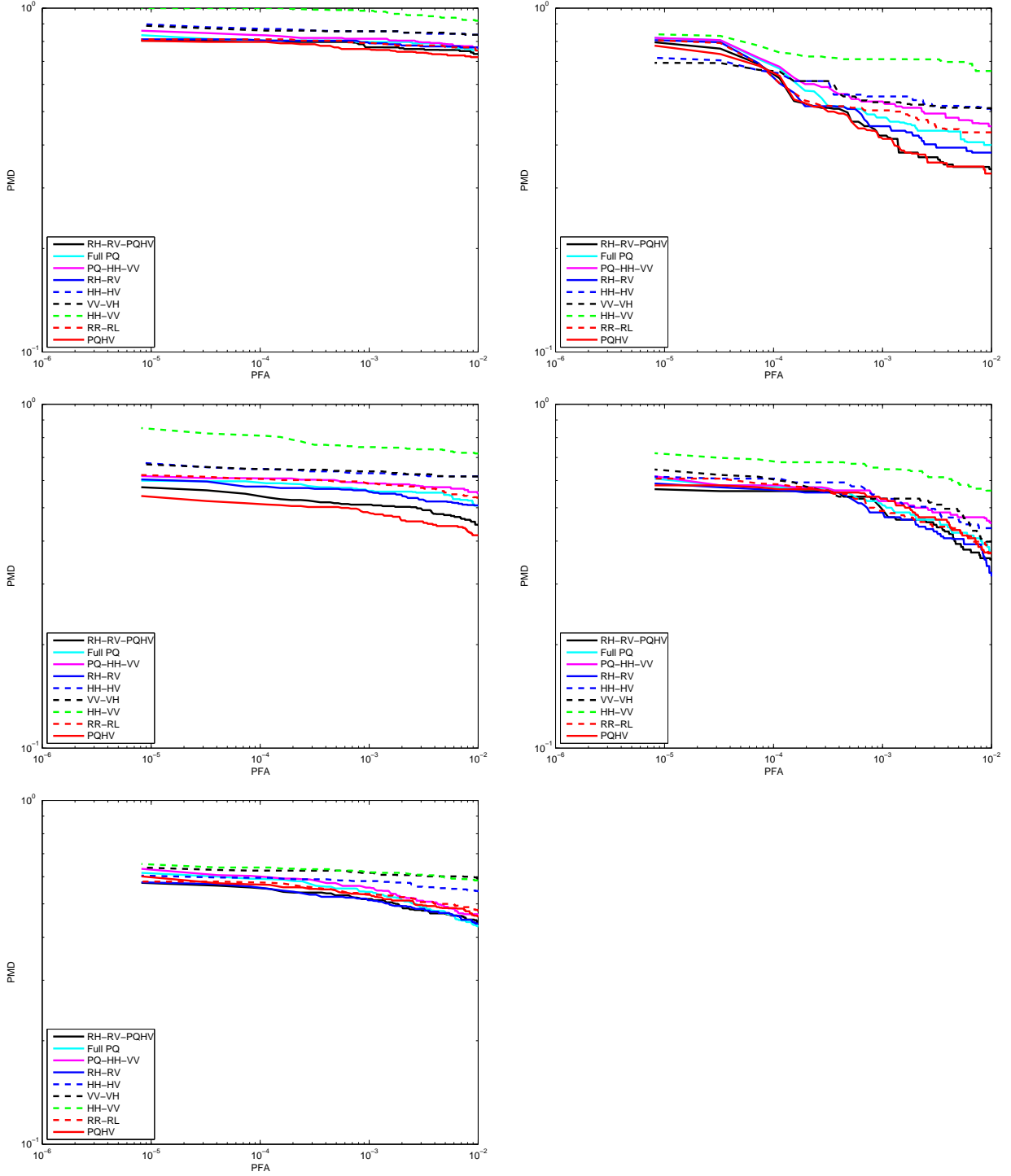
Figure 3.6: *Low Resolution RCM beam mode*: overall median ROC curves for all ships with all orientations in all scenes of each of the incidence angle range for the simulated RCM Low Resolution imaging mode. Top left: B2 (19.77° − 21.78°). Top right: B4 (22.16° − 24.08°). Middle left: B8 (26.88° − 28.71°). Middle right: B12 (31.34° − 33.03°). Bottom left: B21 (40.17° − 41.61°).

Table 3.4: *Ship Detection RCM mode (Beam B21 only)*: median probability of missed detection (PMD) for several ships at a fixed probability of false alarm (PFA) of 10^{-5}. The leftmost column is the orientation of the observed ship in degrees estimated from the range direction of the radar. The orientation angles are subscripted with the number of ships used in the estimate. The lowest PMD (best performance) is shaded in dark grey. Detectors with performance within 0.02 of the lowest PMD are shaded with a lighter grey. For each SAR detector, the lowest PMD is indicated with bold face font. The last row is the overall median taken over the total number of ships within this beam (Tot.).

Ship Orient^n (deg)	PQHV	RH-RV-PQHV	RH-RV	Full PQ	PQHH-VV	RR-RL	HH-HV	VV-VH	H.Pr.
B21 : $40.17° - 41.61°$									
0^{10}	**0.326**	**0.183**	**0.167**	**0.196**	**0.221**	**0.200**	**0.248**	**0.339**	CP
30^8	0.672	0.465	0.442	0.398	0.410	0.544	0.584	0.770	CP
45^8	0.706	0.364	0.344	0.337	0.341	0.405	0.542	0.888	CP
60^5	0.445	0.325	0.321	0.363	0.384	0.361	0.373	0.457	CP
90^7	0.456	0.363	0.305	0.365	0.365	0.352	0.503	0.589	CP
Tot. = 38	0.476	0.292	0.274	0.319	0.332	0.329	0.393	0.526	CP

detector. However, overall one can see that the CP detectors outperform the linear-pol and CirP detectors for the Low Resolution data.

 Ship Detection RCM Beam Mode Results

As indicated in Sec. 4.1, the RCM Ship Detection mode will cover the incidence angle range $36° - 51°$. In this study, this mode is only simulated for the scenes acquired by the B21 beam ($40.17° - 41.61°$). Therefore, for this RCM mode, it is not possible to investigate the impact of incidence angle on detection performance. Table 3.4 shows the median PMD value at a PFA of 10^{-5} for all CP detectors, the CirP detector, and the LP HH-HV and the LP VV-VH only.

The native RH-RV detector has the strongest performance over most orientation angles and has the strongest median performance over all ships within the four scenes. There is no apparent advantage in adding the PQHV channel to this detector. For the two intermediate ship orientation angles of $30°$ and $45°$, the Full PQ detector has the strongest performance, although in the latter case the RH-RV detector was within 2%.
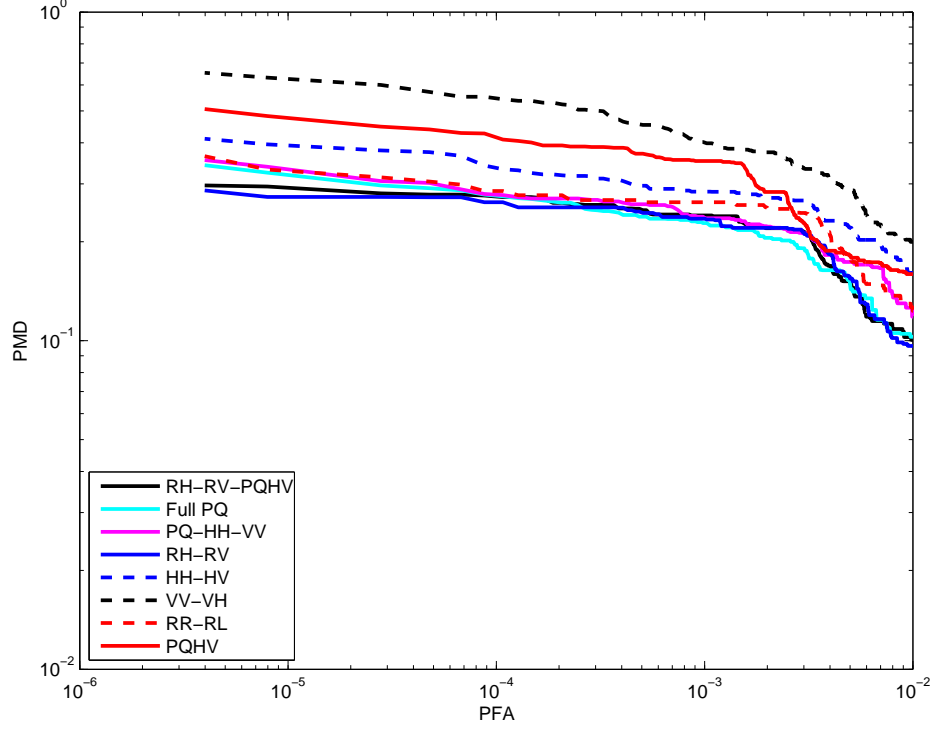
Figure 3.7: *RCM Ship Detection mode (Beam B21 only)*: overall median ROC curves for all ships with all orientations.

In order to investigate the impact of ship orientation on the detection performance, we can see that for all detectors, the lowest PMD value occurs at the 0° orientation which means that the NLPOP = 100% for this category. This opposes what was found in the Low Resolution mode where the 90° orientation has the highest NLPOP. This can be interpreted again on the light of the fact that the range pixel spacing of the Ship detection mode is the least in all modes. Thus, ships with 0° orientation have the largest number of pixels in the range direction which gives less chance of missed detection and hence lower PMD values than other orientations.

The ROC curves shown in Figure 3.7 mirror the Medium and Low Resolution results. The RH-RV detector has the strongest performance across all levels of PFA, followed closely by RH-RV-PQHV. It appears from the ROC curves that the performance of all detectors is weakening as the PFA decreases, except the RH-RV and RH-RV-PQHV, whose performance seems to be relatively constant after PFA of 10^{-4}. In general, the CP detectors are all

stronger than the linear dual-pol and RR-RL detectors.

3.1.3 Discussion

Table 3.5 summarizes the median detection performance over all ship orientations. The effect of ship orientation on detection performance is first summarized. For the FQ beam mode, the effect of ship orientation is variable with NLPOP of 24% for 0° mostly occurred at incidence angle ranges between 32° and 41° and 50% for 90° mostly occur between the two steep incidence angle beams B2 and B4. For the Ship Detection Mode at B21, there is significantly enhanced performance at 0°, for all detectors. For Low Resolution mode, for all detectors and all incidence angles there is enhanced detection at 90°, with an NLPOP of 91%. The effect of ship orientation on Medium Resolution is more variable. For the shallow beams - incidence angles between 32° and 41° – detection performance is enhanced at 90° orientation, with some enhancement at the shallowest beam at 60°. At B8, all detector had enhanced detection at 0°. At the two steepest beams, the performance is more variable, with half the detectors having their lowest PMD at 90°, and the rest at intermediate orientation angles. The NLPOP with this imaging mode is 90°:46.67%; 0°: 20%; and intermediate angles: 34.33%. In general, it has been found that, for all modes, the best performance occurs at either 0° or 90° orientation for more than 66% of the cases.

The effect of ship orientation on ship detectability has been pointed out by many papers [84] - [87]. Margarit and his colleagues have integrated detailed ship and sea surface scattering models with a SAR simulation system (called GRECOSAR) that can model polarimetric backscatter as a function of the dynamic three-dimensional ship orientation [86, 87]. They note that the different polarimetric scattering mechanisms are mixed at spatial resolutions comparable to Radarsat-2 FQ and that the polarimetric backscatter, in this case, is very sensitive to incidence angle and orientation [86, 87] . Our results confirm that the ship orientation has a clear impact on the performance of the LRT detector.

Second we discuss the effect of incidence angle. The general trend is that as the incidence

Table 3.5: Summary of detection performance results.

RCM Mode	PQHV	RH-RV-PQHV	RH-RV	Full PQ	PQHH-VV	RR-RL	HH-HV	VV-VH	HH-VV	H.Pr.
B2 : $19.78° − 21°$										
Fine Quad	0.469	0.477	0.519	0.540	0.580	0.524	0.549	0.553	0.862	CP
Low	0.803	0.804	0.811	0.831	0.858	0.811	0.896	0.887	1.00	CP
Medium	0.832	0.670	0.678	0.753	0.779	0.678	0.684	0.666	0.972	LP
B4 : $22.16° − 24.08°$										
Fine Quad	0.544	0.479	0.453	0.487	0.501	0.463	0.286	0.290	0.622	LP
Low	0.771	0.791	0.805	0.818	0.818	0.805	0.715	0.693	0.838	LP
Medium	0.470	0.481	0.518	0.575	0.624	0.545	0.570	0.570	0.823	CP
B8 : $26.88° − 28.71°$										
Fine Quad	0.268	0.269	0.325	0.303	0.360	0.337	0.359	0.354	0.685	CP
Low	0.538	0.572	0.603	0.599	0.617	0.622	0.673	0.667	0.848	CP
Medium	0.386	0.414	0.463	0.436	0.473	0.450	0.518	0.526	0.695	CP
B12 : $31.34° − 33.03°$										
Fine Quad	0.259	0.198	0.265	0.294	0.322	0.249	0.282	0. 267	0.490	CP
Low	0.581	0.565	0.586	0.604	0.612	0.608	0.614	0.643	0.717	CP
Medium	0.427	0.387	0.378	0.416	0.427	0.455	0.452	0.518	0.588	CP
B21 : $40.17° − 41.61°$										
Fine Quad	0.268	0.269	0.325	0.303	0.360	0.337	0.359	0.354	0.685	CP
Low	0.598	0.574	0.577	0.614	0.629	0.581	0.603	0.637	0.651	CP
Medium	0.350	0.316	0.309	0.376	0.389	0.346	0.387	0.414	0.423	CP
Ship Detection	0.476	0.292	0.274	0.319	0.332	0.329	0.393	0.526	-	CP

angle increases, the detection performance increases. For the FQ mode, it is noticed that the performance is enhanced from B2 to B21 for all detectors except for the LP VV-VH and LP HH-VV. These two detectors suffer from deteriorated performance between B4 and B8. Between B2 and B4, the detection performance is enhanced for all detectors except for the PQHV and the LP HH-HV. For the RCM modes, it has been mentioned earlier that the performance gain between the two steepest beams is relatively modest for Low Resolution. In addition, for a few of the Low Resolution detectors, the performance deteriorates slightly as the incidence angle increased from B12 to B21. For example, the strongest Low Resolution detector over all beams (RH-RV-PQHV), is at B12. This is not the case for the Medium Resolution detectors whose performance increases steadily from B2 through to B21.

As expected, the detection performance increases with spatial resolution. Within each beam, the performance of FQ mode outperforms all RCM modes. Among all RCM modes, the performance of the Medium Resolution is significantly stronger than the Low Resolution. And with two exceptions, the Ship Detection Mode has stronger performance than the Medium Resolution. The highest detection performance across all beams and spatial resolutions is the FQ mode followed by the Ship Detection RCM mode at B21, as expected. It is worth mentioning that the performance of the RH-RV detector of the Ship Detection and Medium Resolution modes is close to that of the PQHV detector of the FQ mode at

B21.

Ship detection performance reported by Vachon et al. [29], using Radarsat-1 data, and Askari and Zerr [35], using ERS ScanSAR data, with fine and low resolution, demonstrate that shallow incidence angle beams are preferable for ship detection, due to high ship/sea contrast. These studies also find that ship detection performance is higher for fine beam modes, due to their large incidence angle and higher resolution, than the lower resolution ScanSAR data. Our results are consistent with all these findings in terms of effect of both resolution and incidence angle on detection performance.

In general, it is found in this study that the detection performance of the CP detectors to be stronger than the standard linear dual-pol detectors. In all but three cases, the strongest detector for each beam/resolution is a CP detector. At the three steepest beams between 20° and 28°, the strongest performer is the PQHV detector. At the two shallowest beams, the strongest performer for the Medium and Ship Detection resolutions, is the RH-RV detector. For Low Resolution at these incidence angles and for the FQ mode at B12 (32°), the performance of this detector is enhanced slightly by adding PQHV. For the FQ mode at B21 (40°), the strongest performance is for the PQHV followed by the merged CP detector.

As there are no published analyses of ship detection performance with simulated RCM data, this study results are compared to other SAR systems. Liu and Meek [16] used CP data, simulated from a single Radarsat- 2 Fine Quad (Beam 4) scene, for ship detection. Although they do not reconstruct PQ data for the purpose of ship detection, they use the raw CTLR CP data to compare the detection performance of the ship detection LRT algorithm [16] with quad-pol, |HH/HV| and HH. The detection performance analysis is carried out on eight ships by plotting the ROC curves for these ships. For five of the eight cases studied, the simulated CTLR system provided improved performance over the |HH/HV| system. For the other three cases, the |HH/HV| system has a slightly higher performance than the CTLR

system. Our results agree with Liu's in that, for the FQ and all RCM modes at B4 beam, the CTLR performs better for some orientation categories while for the others, the LP HH-HV performs better than the CTLR. A single paper is found in the literature that generates PQ data and compares the ship detection performance of the PQ data with quad-pol data using ROC approach as in the current study [66]. Yin et. al [66] generate two ROC curves for two different data sources: JPL AIRSAR and SIR-C, presumably based on two individual ships. The ROC curves show the detection performance of the original quad-pol data, PQ data based on their refined algorithm, PQ data based on the original Souyris algorithm and the compact polarimetry data (in their case he simulated $\pi/4$ data). They do not explain how the LRT was implemented in these cases, thus it is not known whether the two PQ cases and the CP case are amplitude-only or if they are a sum of a coherent HH/VV and |HV |. Finally, it is not mentioned in that paper what the incidence angles of the imaging beams nor the orientation of the two ships were. In both cases, the quad-pol detectors outperform the PQ and CP detectors. For the AIRSAR case, the PQ and CP detectors have comparable performance while in the SIR-C case, the CP detector have much higher performance than the PQ case. Thus, although, they used $\pi/4$ configuration, our results are consistent with the Yin results in that detectors based on the coherent dual-pol compact polarimetry data have higher performance than those based on the full set of quad-pol covariance matrix elements reconstructed from the CP data.

3.2   Conclusion

In this chapter, an investigation of ship detection performance was introduced for a number of Radarsat-2 beam modes; the Fine Quad mode and three simulated Radarsat Constellation Mission modes with different resolution. The investigation of ship detection performance for the simulated dual-pol RCM data is the first in the literature. In this study three wide swath imaging modes that will be available on RCM imaging radars are examined: Low

Resolution, Medium Resolution, and Ship Detection. The focus of this study was on dual-polarization image data, as these provide a balance between multiple polarization and wide swath imaging.

In this work, the detection performance was assessed in terms of the median probability of missed detection (PMD) for each system calculated over a number of ships spread over the available scenes as a function of the probability of false alarm (PFA) and at specific PFA value. It has been found that, at incidence angles greater than 25° compact polarimetry modes have superior ship detection performance to linear polarization data. At steeper incidence angles, the two polarization configurations have comparable performance. For all polarizations, ship detection performance increases with incidence angle, with the highest performance at about 40°. In addition, detection performance increases with spatial resolution, the FQ mode data has the strongest performance over all RCM modes data while for RCM data, the Low Resolution data has the weakest performance and the Ship Detection mode has the strongest performance. Several different types of compact polarimetry data were explored, including the raw RH-RV data, and pseudo quad-pol (PQ) data reconstructed from the CP data. It has been found that PQHV and RH-RV, by themselves and in combination had the highest performance over other CP and linear-pol data. The PQHV data is most effective at steeper incidence angles, less than 30°. At angles greater than 30°, RH-RV data has the highest performance for Medium Resolution and Ship Detection modes, while for FQ mode and Low Resolution, the addition of PQHV improves the performance. This study also took ship orientation into consideration and investigated the impact of the orientation on the detection performance. Higher detection performance is expected when the ship and its superstructure were perpendicular to the radar bore sight. This expectation was met at incidence angles for the Low Resolution data. For Medium Resolution data, higher performance for perpendicular ship orientations at incidence angles greater than 27° was observed, and no effect at steeper incidence angles was found. Enhanced performance

is expected for ships parallel to range direction. This was observed for the FQ and Ship Detection modes at shallow incidence angles. Thus, the results of this study suggest that the three RCM modes generally, and the Ship Detection mode in particular, are promising compromise between the ship detection performance and the wide swath width desired for maritime surveillance. Furthermore, it has been found that the compact polarimetric SAR detectors outperform the conventional linear dual-pol detectors at the three RCM modes for ship detection. Moreover, the results show that CP reconstruction of ocean data using Collins algorithm aids in improving the ship detection performance for FQ and the three RCM modes.

Chapter 4

Hybrid Ship Detection Algorithm for CP SAR

Methods and Theoretical Concepts

The second part of the thesis introduces a new ship detection algorithm for CP SAR. This part is covered in Chapter 4 and 5. In this chapter, the data used and a detailed description of the detection algorithm is introduced. Moreover, the theoretical concepts and related basics of each part of the proposed algorithm are presented. In Chapter 5, results from the proposed detection algorithm are discussed and finally, conclusions are drawn from the performed work.

The Stokes vector and derived parameters of CP SAR are utilized to develop a robust ship detection algorithm in compact polarimetric SAR data. The proposed algorithm combines four detection techniques together to improve the detection performance and discrimination between ships and false alarms. The introduced detection algorithm has a pre-screener and a discriminator. The pre-screener of the algorithm is a hybrid one that employs three detection methods and has two steps. The first pre-screening step uses global thresholding to highlight all possible target candidates. In the second pre-screening step, the detected candidates are retested by using either one of two new Adapted Thresholding Detectors (ATDs). These detectors retest the candidate targets against their local background statistics. The developed ATDs are the Stokes parameters LRT and S_0-CFAR detectors. The selection between these two pre-screeners is made according to the size of the candidate target. The Gaussian Mixture Model approach is used to estimate the joint pdf of the Stokes parameters for the LRT detector for ocean and ship data and for the Stokes S_0 of ocean data. The discriminator of the algorithm relies on the scattering mechanisms of the detected target to distinguish ships from false alarms.

The performance of the proposed algorithm is assessed by comparing the number of detected ships with verified positions to the total number of ships with AIS positions. The chapter is organized as follows. Section 4.1 presents the data and the preprocessing operations applied to it. Sec 4.2 to Sec 4.7 present the basic concepts related to the proposed algorithm. A detailed description of the developed ship detection algorithm is given in Sec 4.8. Section 4.9 outlines the measure of the detection performance assessment of the algorithm. Finally, section 4.10 concludes the chapter.

4.1 Data and Study Site

The proposed detection algorithm is applied to data simulated in three RCM modes: Medium resolution, Low Resolution and Ship detection imaging modes, as in the first part of the thesis. The polarimetric dataset used in this study to simulate the RCM data is composed of six RS-2 scenes of the Gibraltar Strait acquired by the Fine Quad beam (FQ-21). The scenes are located around $(35° - 37°)$ N, $(5° - 6°)$ W. The scenes are referred to by their numbers. The scene numbers "Scene No.", the acquisition date "Acq. date" and time "Acq. time" of each scene are depicted in Table 4.1. All scenes have a range sample spacing of 4.73 m and the azimuth spacing is 5.1 m. The FQ-21 beam covers the incidence angle range of $[40.17° - 41.61°]$. Nominal Radarsat-2 Fine Quad mode resolution is approximately 5.2 m in range by 7.6 m in azimuth. The average wind speed in m/s "W.S." calculated for each scene according to the model developed by Vachon and Wolfe [79] is also provided in the table. The data is calibrated by the (βo) radar backscatter coefficient. Automatic identification system (AIS) data is available for a number of ships in each scene to be used for detection performance assessment. The total number of ships with AIS positions in all scenes is 147 ship. The number of ships with verified positions "No. Sh." for each scene is depicted in Table 4.1. The verified ships have various sizes; ship lengths range from 29 m to 337 m.

In this work, the use of RCM data for ship detection is explored as these data have a

Table 4.1: An overview of the Fine Quad Radarsat-2 data of the Strait of Gibraltar scenes used in the study of this chapter. The "Acq. date" refers to the scene acquisition date, the "Acq. time" is the scene acquisition time in GMT, the "W.S" is the wind speed in (m/s) and "No. Sh." is the number of ships with verified positions in each scene. A value of < 3 for the wind speed indicates that the wind speed was too low to be estimated from the data.

Scene No.	Acq. time	Acq. date	W.S (m/s)	No. Sh.
1	06:22:40	2009-02-14	13.3	9
2	06:22:38	2009-02-14	12.1	8
3	18:23:29	2009-02-09	5.5	11
4	18:23:29	2008-11-05	<3	11
5	18:23:32	2009-02-09	6.2	54
6	18:23:32	2008-11-05	<3	54

wider swaths than the FQ data. The RCM data is simulated as a single look complex (SLC) image in the three imaging modes. The simulated data has a noise floor of approximately -22 dB (according to the RCM specifications) which is larger than the original Radarsat-2 data which has a noise floor of approximately -30 dB [80]. The incidence angle range "Inc. Ang.", the simulated spatial resolution of the SLC data "SLC. Res.", the nominal multi-look spatial resolution "ML Res.", the number of looks "N Look", the simulated multi-look pixel spacing "ML_s Pix Sp." and the nominal swath width "N.S.W" of each RCM mode are indicated in Table 4.2. The RCM data is simulated using a software developed and provided by Dr. Francois Charbonneau of Canada Centre for Remote Sensing (CCRS).

Table 4.2: An overview of the simulated RCM data in the three imaging modes used in this study. This table shows the incidence angle "Inc. Ang." in degrees, the SLC simulated resolution "SLC. Res."in the (range x azimuth) directions, the nominal multi-look spatial resolution "ML Res.", the number of looks "N Look" in the (range x azimuth) directions, the simulated multi-look pixel spacing "ML_s Pix Sp." and the nominal swath width "N.S.W in Km for each of the modes.

RCM Beam Mode	ML Res.	N Look	Inc. Ang.	SLC. Res.	ML_s Pix Sp.	N.S.W
Medium Resolution	50 m	4 x 1	$19° - 58°$	7.9 m x 49.7 m	28.6 m x 20 m	350 Km
Low Resolution	100 m	8 x 1	$19° - 54°$	8.3 m x 98.8 m	57.1 m x 40 m	500 Km
Ship Detection	variable	variable	$36° - 51°$	2.7 m x 48 m	-	350 Km

4.1.1 Data Preparation

As the ship detection algorithm introduced in this thesis is designed specifically for CP SAR Stokes parameters, some pre-processing operations need to be performed on the original full polarimetric data. First, the RCM data is simulated in the three RCM modes using the RCM simulator with the original quad-pol images as input. Second, the CTLR CP scattering vector is generated for each RCM mode using Eqn. 2.2 for the entire scene from the simulated RCM images. For the Low Resolution and Medium Resolution modes, the data are multilooked according to the number of looks depicted in Table 4.2 by spatially averaging pixels in the range direction. On the other hand, the Ship Detection mode data is used as SLC image because, according to RCM specifications, the number of looks for this mode is not specified [80]. Next, for each RCM mode, the Stokes vector is then constructed for each pixel in the image using Eqns. 4.1 - 4.4. This step results in four images for the scene, an image for each Stokes parameter. The required spatial averaging is performed using a 3×3 boxcar filter for the Low and Medium Resolution modes. For the Ship Detection mode, a 5×5 boxcar filter is used as this data has not been multi-looked . These window sizes are selected to achieve a trade-off between the required smoothing effect and the corresponding deteriorated resolution. After that, the Stokes parameter images are passed to the land masking algorithm.

4.2 Stokes Parameters

When a polarized wave interacts with a target, its state of polarization may be altered. While radar transmits fully polarized waves, the received waves may be fully or partially polarized. In other words, completely polarized incident wave may become randomly polarized after being scattered by an object that gives rise to multiple internal reflections. George Stokes [88] developed a method to represent the state of polarization of partially polarized waves, namely the Stokes vector which is composed of four real quantities that capture all the information

about the backscattered field [58]. The general expressions of the Stokes parameters are given in Chapter 1 in Eqns. 1.14 to 1.17. In this Chapter, the focus is on the use of the Stokes parameters and their derived parameters of the CTLR CP SAR. The Stokes parameters forms consistent with this case are given in Eqns. 4.1 to 4.4

For a dual-pol SAR which receives two orthogonal linear polarizations (E_H and E_V) in response to a right-circularly polarized transmitted wave, the Stokes parameters are given as [58, 89]

$$S_0 = \langle |E_H|^2 + |E_V|^2 \rangle = S_0 \tag{4.1}$$

$$S_1 = \langle |E_H|^2 - |E_V|^2 \rangle = m\, S_0\, \cos 2\chi\, \cos 2\psi \tag{4.2}$$

$$S_2 = 2\,\mathcal{R}\langle E_H E_V^* \rangle = m\, S_0\, \cos 2\chi\, \sin 2\psi \tag{4.3}$$

$$S_3 = 2\,\mathcal{I}\langle E_H E_V^* \rangle = m\, S_0\, \sin 2\chi \tag{4.4}$$

where $\mathcal{R}$ and $\mathcal{I}$ are the real and imaginary parts of the complex quantity respectively, $*$ is the complex conjugate and the triangular brackets are the spatial averaging operator. The right column of this formalism relates the Stokes parameters to the polarization ellipse variables; χ and ψ; where χ is the ellipticity of the polarization ellipse, while ψ is the orientation of the major axis of the polarization ellipse as shown in Figure 4.1. The degree of polarization (m) is defined as the ratio of the power of the polarized portion of the wave to the total power of the wave. Stokes S_0 represents the total power of the wave; S_1 is the difference between the power of the two orthogonal linear components, S_2 is the difference between the power of the $\pi/4$ rotated two orthogonal components and S_3 is the difference between the power of the right and left circularly polarized components [90, 91, 92]. Of the four parameters, only three are independent [91] since, generally, $S_0^2 \geq S_1^2 + S_2^2 + S_3^2$.
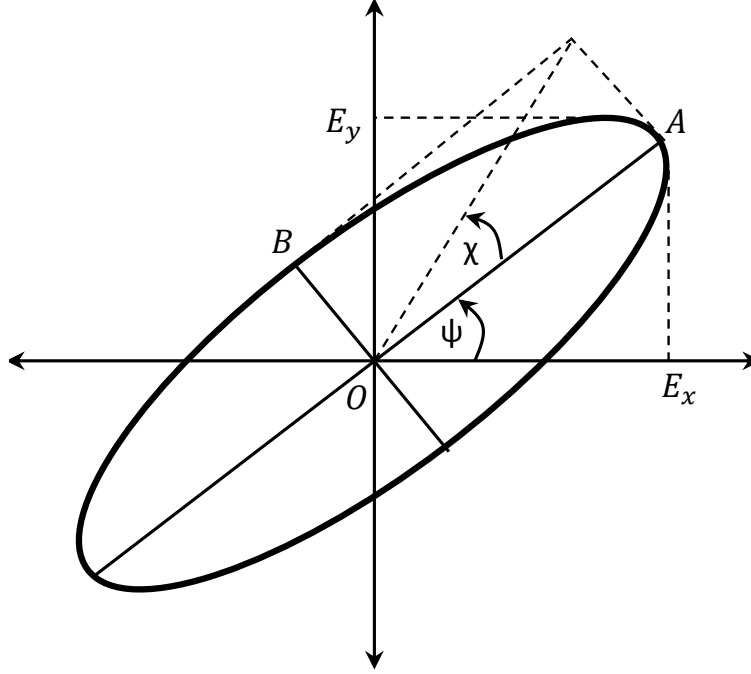
Figure 4.1: The polarization ellipse. E_x, E_y is the horizontal and vertical components of the electric field vector respectively. OA is the ellipse semi-major axis, OB is the ellipse semi-minor axis, χ is the ellipticity angle and ψ is the orientation angle.

4.3   Stokes Derived Parameters

As pointed in Chapter 1, there may be many parameters that are derived from the Stokes parameters. These child parameters have their relation to the physical scattering mechanism from targets [89]. In this chapter, only two child parameters are used jointly for ship detection. The first one is the degree of polarization m defined in Sec. 4.2 and given as [20]

$$m = \frac{[S_1^2 + S_2^2 + S_3^2]^{1/2}}{S_0} \qquad (4.5)$$

Since 1950's, m has been recognized as the most important parameter that shows how much the backscattered wave is polarized [68, 93, 94]. Values of m range from 0 for completely depolarized wave to 1 for completely polarized wave while m takes values in between these two extremes for partially polarized waves. Therefore, m for odd and even bounce scatterers is close to 1 while for volume scatterers, m is close to 0.

The second derived parameter used in this research is the ellipticity of the polarization

ellipse, χ which is related to Stokes parameters through the relation [68]

$$\sin(2\chi) = \frac{S_3}{mS_0} \qquad (4.6)$$

The ellipticity χ is the angle determined by the ratio of the semi-major axis to the semi-minor axis of the polarization ellipse [92]. Thus, it describes the degree to which the polarization ellipse is oval. In addition, the sign of χ indicates the handiness of elliptical/circular polarization. The ellipticity χ takes values in the range [-45° to 45°]. The value -45° corresponds to the right-handed circular polarization while the value +45° is for the left-handed circular polarization. When $\chi = 0$, the wave is linearly polarized with an orientation determined by the angle ψ.

4.4 Compact Polarimetric Decomposition

Decomposition is a mature technique that is used to interpret the information contained in the radar data and relate it to the scattering mechanisms or the physical properties of the imaged area. For quad-polarimetric data, decomposition works on splitting the polarized backscatter of each image pixel into a combination of scattering mechanisms [95]. Polarimetric decomposition techniques may be classified into coherent and incoherent decomposition. The polarimetric coherent decomposition is implemented using the scattering matrix to study point targets. However, the polarimetric incoherent decomposition works on the coherency or covariance matrix to study distributed targets [95].

In compact polarimetric decomposition, two or more parameters derived from the Stokes parameters of the dual-pol CP data are used jointly to classify radar backscatter into the corresponding scattering mechanism [20]. There have been two CP decomposition techniques reported in the literature; the $m - \delta$ and the $m - \chi$ decomposition [20, 25, 68]. The degree of polarization m is a common decomposition parameter in both techniques.

In the $m - \delta$ decomposition, the second decomposition parameter is the δ angle defined as the relative phase between the two received components [25]. The δ angle can be calculated

using Stokes parameters according to the relation [23]

$$\delta = \tan^{-1}\left(\frac{S_3}{S_2}\right) \tag{4.7}$$

The δ angle is a discriminator between odd and even bounce scatterers especially when circular polarization is transmitted. In other words, odd bounce scattering causes the phase of the incident field to be shifted by 180° with each bounce, while the reflected wave from even bounce scatterer has zero phase shift with the incident wave. For instance, if the transmitted wave has right circular polarization, then odd bounce scatterer returns a strong backscatter in the opposite sense of rotation polarization [20, 23]. That is, left handed circularly polarized wave which implies that δ is positive while δ is negative for even bounce scatterers [23].

According to this decomposition scheme and in response to right circularly polarized transmission, backscatter contribution to the odd, even and volume scattering mechanisms is classified as follows [20]

$$\text{bs} = [mS_0(1 + \sin(2\delta))/2]^{1/2} \tag{4.8}$$

$$\text{db} = [mS_0(1 - \sin(2\delta))/2]^{1/2} \tag{4.9}$$

$$\text{vs} = [S_0(1 - m)]^{1/2} \tag{4.10}$$

where, vs is the contribution of backscatter in the volume scattering mechanism, bs is the contribution to the Bragg scattering or odd bounce scattering and db is the contribution to the double or even bounce scattering mechanism. When δ is positive, this means that the surface scattering is dominant. On the other hand, when δ is negative, the dominant scattering mechanism is even bounce. Volume scattering is evaluated by multiplying the degree of depolarization (1-m) by the total backscatter power S_0 [20].

In the $m - \chi$ decomposition, the ellipticity χ, as given in Eqn. 4.6, is selected as the second decomposition parameter. This is attributed to its sign, which is an unambiguous indicator of even versus odd bounce backscatter [68, 96]. According to this decomposition,

the backscatter in response to a right circularly polarized transmission contributes to the three aforementioned scattering mechanisms according to

$$\text{bs} = [mS_0(1 + \sin{(2\chi)})/2]^{1/2} \tag{4.11}$$

$$\text{db} = [mS_0(1 - \sin{(2\chi)})/2]^{1/2} \tag{4.12}$$

$$\text{vs} = [S_0(1 - m)]^{1/2} \tag{4.13}$$

As can be seen from the above equations, vs is the same in both schemes while in bs and the db expressions, the δ is replaced by χ. When the right circularly polarized (with negative χ) wave experiences odd bounce reflection due to Bragg surfaces or trihedrals, the received wave is expected to have the opposite sense of rotation (left circular polarization) with positive χ [96]. This causes bs to be larger than db. On the other hand, reflection from even bounce scatterers is expected to be stronger in the same sense of rotation as the incident wave, that is, the right circular polarization [96]. Thus, the db, in this case, becomes larger than bs.

Recently, the $m - \delta$ and $m - \chi$ decompositions have been applied to the CP data collected by the Mini-RF aboard NASAs Lunar Reconnaissance Orbiter [26] and the Mini-SAR on India's lunar Chandrayaan-1 satellite [27] to study the lunar surface [67, 68, 98]. These studies show that the $m - \chi$ decomposition is an efficient technique to interpret surface features according to single (odd) or double (even) bounce signatures in the polarized portion of the backscattered wave, and characterizes the randomly polarized constituents. They conclude that the $m - \chi$ decomposition has demonstrated to be robust in the event that the transmitted field is not perfectly circularly polarized and more efficient than the the $m - \delta$ technique [68]. Therefore, the $m - \chi$ decomposition has been selected to be used in the discrimination stage of the proposed detection algorithm.

4.5 Statistics of Stokes Parameters

Generally, the statistics of SAR data is essential for image speckle reduction, target detection, identification, and classification [99]. Derivation of the statistics of SAR data in the form of scattering vector and covariance matrix have been widely covered in the literature [99] - [103]. Nevertheless, few papers have addressed the issue of analytically deriving the pdf of the Stokes parameters for SAR data. The statistics of the four Stokes parameters of partially polarized light was first derived by Barakat [90]. Later, the work of Barakat was extended by Touzi and Lopes [91]; they derived the pdfs of the Stokes parameters as a function of the effective phase difference and complex correlation coefficients between the receive channels for SLC and multilook SAR data. Jin et. al [101] refined the Stokes pdfs derived by Touzi and Lopes [91] by using some reasonable approximations validated by real SAR data. It is noteworthy that the pdfs formulated in the literature were derived for the individual Stokes parameters. However, to-date and to the best of our knowledge, no single paper presents the joint statistics of the Stokes vector elements of SAR data. Since the LRT component of the proposed detection algorithm requires the joint pdf of the four Stokes parameter, the Gaussian Mixture Model method is proposed to estimate the joint statistics of the CP SAR Stokes vector in this study.

4.6 Gaussian Mixture Model Method for pdf Estimation

The GMM method is a semi-parametric approach that is used for the estimation of the probability density function of random data [76]. The GMM method is utilized in the current study to estimate the pdfs for ocean and ship Stokes parameters. The selection of the GMM for pdf estimation emerges from the need to estimate accurate pdfs for ocean and ship backscatter to improve detection performance. This is attributed to the ability of the GMM approach to form smooth approximations to arbitrarily shaped pdfs even when they are not Gaussian. Moreover, its components describe the multi-modal nature of the

distribution. So, it is reasonable to consider fitting a mixture of Gaussian components for the density estimation given the computational tractability of Gaussian density function [76].

Generally, in the GMM method, the pdf to be estimated can be considered as a linear combination (mixture) of K number of D-dimensional Gaussian pdfs with different parameters as in Eq. (4.14). The GMM is parametrized by the mean vectors, covariance matrices and mixture coefficients for each Gaussian component of the mixture.

$$f(\mathrm{u}; \theta) = \sum_{k=1}^{K} p_k \, g(\mathrm{u}; \mu_k, C_k) \tag{4.14}$$

where u is a D-dimensional data vector (i.e. the measurement data for which the pdf is to be constructed), K is the number of Gaussian components in the mixture, $\theta = (\theta_1, \theta_2, ..., \theta_{K)}$ is the vector of all components parameters where $\theta_k = (p_k, \mu_k, C_k)$ is the parameter vector of the k_{th} Gaussian component containing the coefficient of that component p_k as well as its mean vector μ_k and the covariance matrix C_k. The term $g(\mathrm{u}; \mu_k, C_k), \ k = 1, ..., K$ is the kth Gaussian density given as

$$g(\mathrm{u}; \mu_k, C_k) = \frac{1}{(2\pi)^{D/2} \, |C_k|^{1/2}} \exp^{-\frac{1}{2}(\mathrm{u}-\mu_k)^T C_k^{-1} (\mathrm{u}-\mu_k)} \tag{4.15}$$

Since the mixture coefficients are actually the mixing probabilities of the components, they should be non-negative and their values should never be greater than 1. Thus, the constraints $0 \leq p_k \leq 1$ and $\sum_{k=1}^{K} p_k = 1$ apply.

There are several techniques for estimating the parameters of a GMM. By far the most popular and most straightforward method is the maximum likelihood estimation (MLE) [104]. So, the problem of pdf estimation can be summarized as the problem of finding the parameters of the mixture that maximizes the likelihood of the estimated pdf to generate the data that was used to estimate the pdf. To convert that into a mathematical problem, the likelihood function of the unknown parameters must be deduced and after that to be maximized to estimate the unknown mixture parameters. The likelihood function in our

case is given by

$$L(\mathrm{u};\theta) = \prod_{n=1}^{N} f(u_n;\theta) = \prod_{n=1}^{N} \sum_{k=1}^{K} p_k \, g(u_n;\mu_k, C_k) \tag{4.16}$$

It is clear that the likelihood function $L(\mathrm{u};\theta)$ is a non-linear function of the unknown parameter vector θ which means that no direct solution is possible. However, maximum likelihood parameter estimates can be obtained iteratively using the expectation-maximization (EM) algorithm [105].

The EM algorithm works as follows, beginning with an initial model θ^i, the new model θ^{i+1} is estimated such that $L^{i+1}(\mathrm{u};\theta) > L^i(\mathrm{u};\theta)$. Then the new model becomes the initial model for the next iteration and the process is repeated until some convergence criterion is reached. In the EM algorithm, this is done in two steps; the first is the expectation (E step)and the second is the maximization (M step). The iterative equations of the EM algorithm [76] are given as in Eqs. (4.17 - 4.20).

E step

$$p^i(k|n) = \frac{p_k^i \, g(u_n;\mu_k^i, C_k^i)}{\sum_{k=1}^{K} p_k^i \, g(u_n;\mu_k^i, C_k^i)} \tag{4.17}$$

M step

$$p_k^{i+1} = \frac{1}{N} \sum_{n=1}^{N} p^i(k|n) \tag{4.18}$$

$$\mu_k^{i+1} = \frac{\sum_{n=1}^{N} p^i(k|n) \, u_n}{\sum_{n=1}^{N} p^i(k|n)} \tag{4.19}$$

$$C_k^{i+1} = \frac{\sum_{n=1}^{N} p^i(k|n)[u_n - \mu_k^{i+1}][u_n - \mu_k^{i+1}]^T}{\sum_{n=1}^{N} p^i(k|n)} \tag{4.20}$$

Where $p(k|n)$ is the *a posteriori* probability for component k and p_k, μ_k and C_k are defined as above.

4.6.1 Gooodness of Fit of the GMM and Number of Components Determination

In this study, the assessment of the goodness of fit of the GMM distribution and the determination of the appropriate number of Gaussian components in the GMM are done using information statistics (parsimony indices) [76]. These statistics are based mainly on the value of (-2) times the log-likelihood of the model, adjusted for the number of parameters in the model. In other words, given a set of candidate models for the data, the preferred model is the one with the minimum index value. Hence, parsimony indices not only reward goodness of fit, but also include a penalty that is an increasing function of the number of estimated parameters [76]. This penalty discourages over fitting and is used to determine the appropriate number of components in mixture models [76]. So, in comparing different models for the same data, one will prefer models with lower values on these indices.

The most common parsimony indices include the Akaike Information Criterion (AIC) [106] given as Eq. (4.21) and the Schwarz Bayesian Criterion also called the Bayesian Information Criterion (BIC) [107] given by Eq. (4.22).

$$AIC = -2\ln(L) + 2p \tag{4.21}$$

$$BIC = -2\ln(L) + p\ln(N_p) \tag{4.22}$$

where $\ln(L)$ is the log-likelihood, p is the number of estimated model parameters and N_p is the total number of data points used for pdf estimation.

The AIC and BIC are used for comparison across several plausible models where the lowest value indicates the best fitting model. It is worth mentioning that there is no common acceptance of the best criteria for determining the number of components in mixture modelling [108]. However, it has been shown that the BIC provides a better model selection than the AIC [107, 108]. It has been shown in the literature that the AIC tends to select models with large number of components which may overfit the data especially when the number of data points are large [107] which is applicable to our case. Moreover, a study conducted by Nylund et. al [108] which looked at the performance and the ability of these

indices and others to correctly identify the number of components in mixture models showed that the BIC performs the best among all information criteria for model selection in mixture models. Thus, in this study, it is decided to use the BIC for the selection of GMM order and the assessment of the goodness of fit.

4.7 Land Masking

Land masking is a preprocessing operation that is applied after the RCM data is simulated and before applying the detection algorithm to the scenes. Land regions in the scenes are excluded to avoid producing false alarms. In this work, the land is masked after detecting the shoreline from the RGB images generated by the m-χ decomposition of the CP RCM images. The shoreline is detected using Canny edge detector [109] after smoothing speckles using the Lee filter [110]. In order to extract the shoreline perimeter, morphological dilation and erosion operations are used. After the shoreline is extracted, land pixels included within the shoreline perimeter are set to zero and not included in any calculations afterward.

4.8 The Proposed Ship Detection Algorithm

In pixel-based ship detection algorithms, each image pixel is to be classified either to a ship or to the ocean. So, the ship detection problem is simply a binary test of simple hypotheses: the null hypothesis in which the pixel belongs to the ocean whereas the alternative hypothesis in which the pixel belongs to a ship. According to the Neyman-Pearson lemma [74, 111], the best statistical test for the binary hypotheses is the one that maximizes the probability of detection at a specific probability of false alarms [74]. This aim can be achieved through using the Likelihood Ratio Test. However, the LRT requires the pdf of the ocean and the ship data. As ships are not known *apriori*, it is often not possible to estimate the pdf of ship data. Hence, it is usually resorted to use the background (ocean) statistics only for the hypothesis testing like in the CFAR detectors. In this thesis, we tackle the problem of

ship detection using a new hybrid detection algorithm that utilizes both the LRT and the CFAR detectors in its primary stages. The proposed ship detection algorithm is composed of a pre-screener and a discriminator. The pre-screening stage aims to highlight candidate ships and it is composed of two steps: a global thresholding step followed by an adaptive thresholding one. The discriminator distinguishes between real ships and false alarms based on the type of scattering mechanism of the targets detected by the pre-screener. Finally, a detection decision is taken based on that. In the following section, a detailed description of the proposed detection algorithm is given. The detection procedures of the introduced hybrid ship detection algorithm are summarized in the flow chart of Figure 4.2.

4.8.1 The Pre-screening Stage

In the first step of pre-screening, the entire image is scanned to search for ships candidates using a global threshold. Since ships are usually fabricated from reflective materials, ship pixels appear brighter than surrounding ocean pixels which means that the received power by the SAR sensor from ships is larger than that from ocean. As the S_0 value of each pixel represents the total power scattered from the area contained by that pixel, in this first pre-screening step, the S_0 image is globally thresholded to highlight candidate targets. Figure 4.3 shows 2D plots of the S_0 values of ship pixels surrounded by ocean. Figure 4.4 shows an intersection of the S_0 surface plot across one range line at a fixed azimuth. It is clear that the S_0 values of ocean is much less than that of ship pixels. Therefore, the global threshold is set to be the maximum S_0 value of a block of ocean pixels which is still much less than S_0 of most ship pixels. This step results in a large number of candidate detections which is useful to avoid missing any ships although some of these detections are anticipated to be false alarms from ocean pixels.

In order to refine the detections of the first pre-screening step, these detections are subjected to an adaptive thresholding step to test the candidate pixels against their neighboring ocean pixels at a specific PFA.
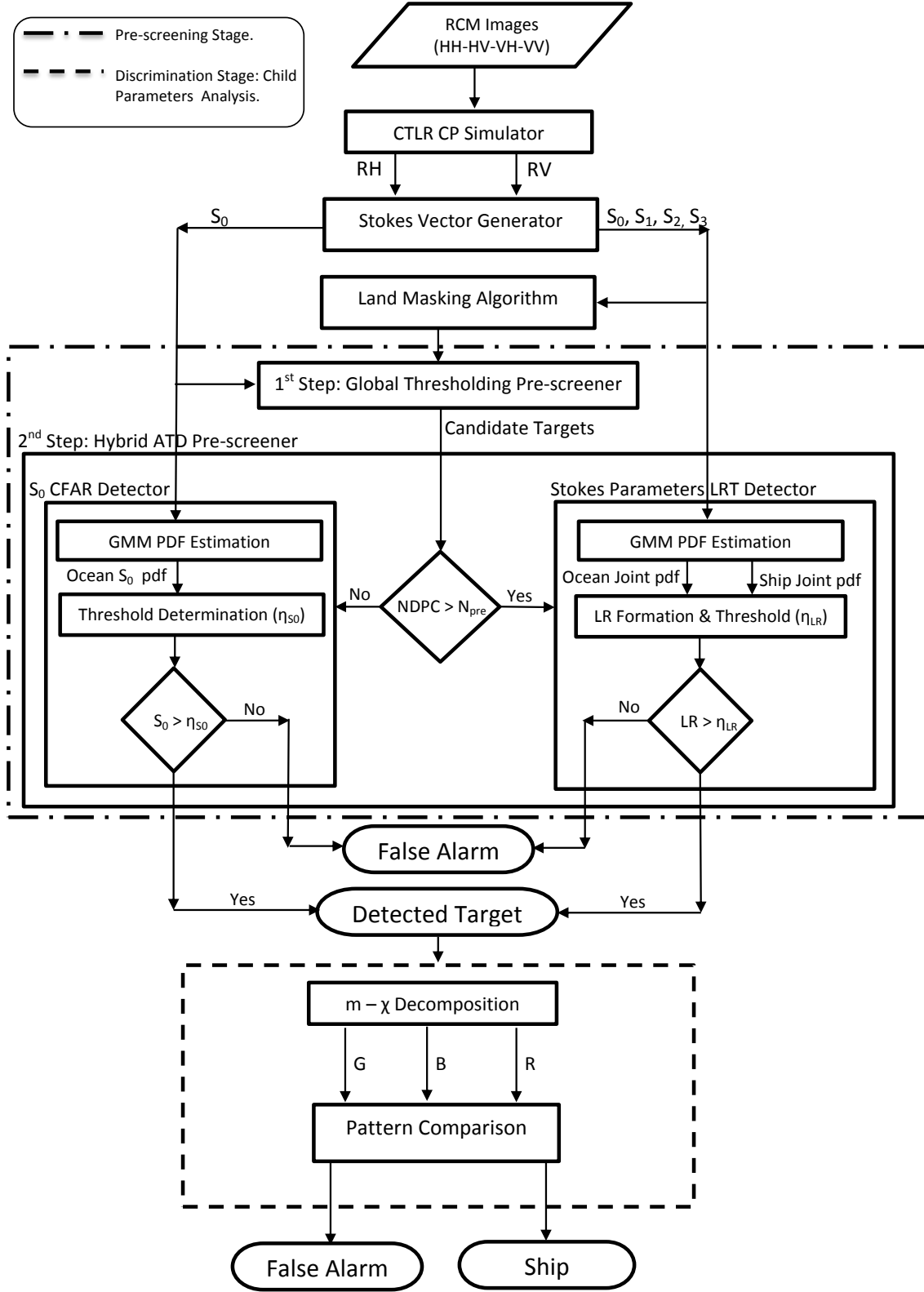
Figure 4.2: Flow chart of the proposed hybrid ship detection algorithm. NDPC refers to the number of detected pixels per candidate target, η_{LR} is the threshold of the LRT detector and η_{S0} is the threshold of the CFAR detector.
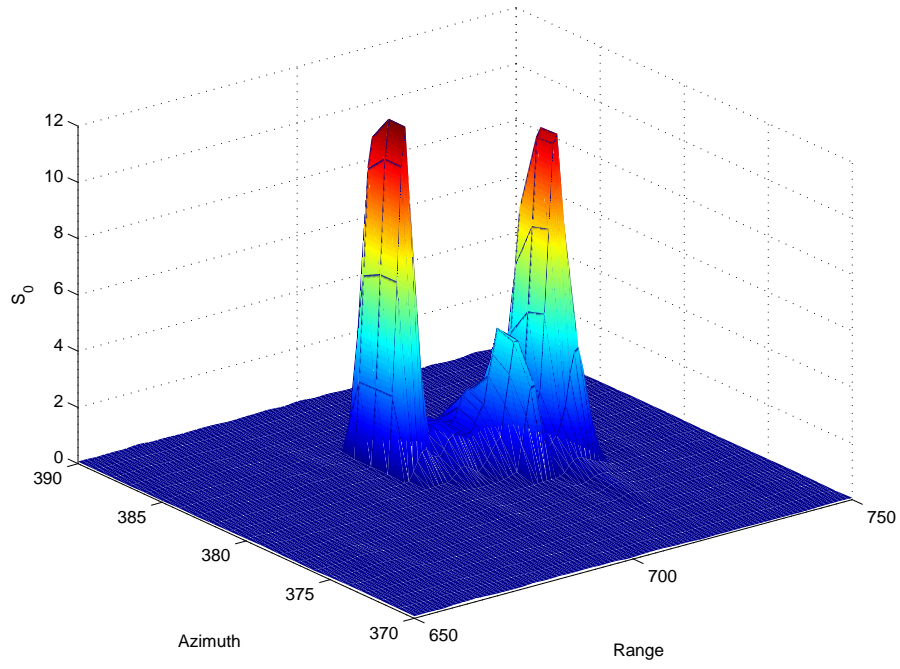
Figure 4.3:   3D-plot of Stokes S_0 of a ship surrounded by ocean.
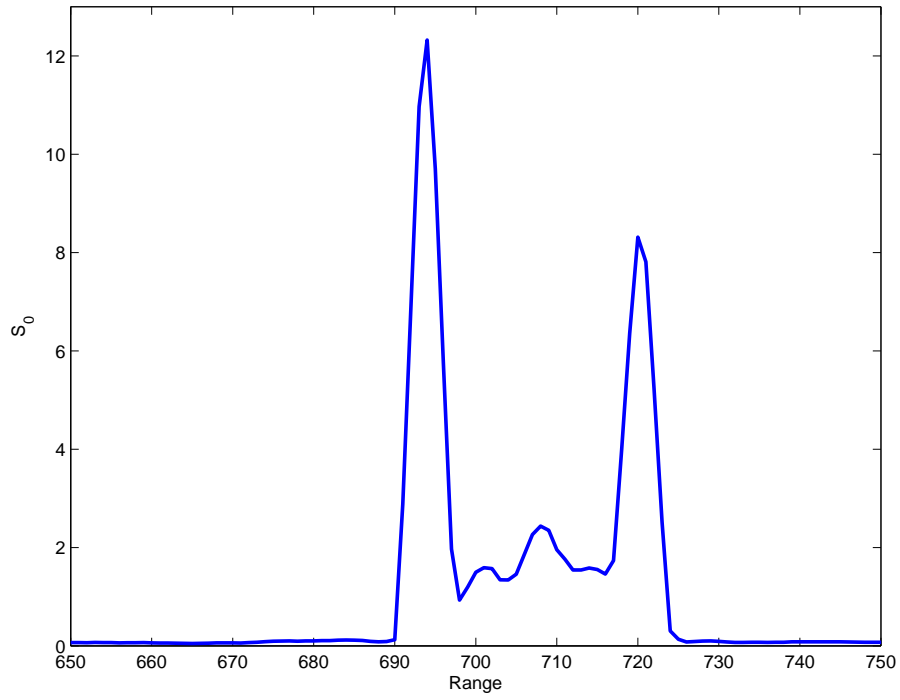
Figure 4.4: An intersection of the surface plot of Figure 4.3 along the range direction at a fixed azimuth.

97

Window Setup for the Pre-screening Stage

As the second pre-screening step is designed to work only on candidate targets detected by the first pre-screening step, each candidate target is surrounded by a rectangular window called the "target window". Each pixel of this window is then tested by an ATD against a threshold. When the LRT detector is used, all pixels of the candidate target are used for the estimation of the ship data pdf. The target window is surrounded by another larger window called the "background window". The pixels included in the background window are used for the estimation of the ocean data pdf and threshold determination. The window setup of the second step of the pre-screening stage is depicted in Figure 4.5. This setup differs from conventional CFAR window setup which includes additional guard window between the target and background windows. In this setup, a guard window is not used since the entire candidate ship is included in the target window. Moreover, as a precautionary procedure in the case of close candidate targets, if any detected pixel is found in the background window, it is then excluded from ocean data.

The target window boundaries are set to be:

$$A_T = az_{min} - C1; \tag{4.23}$$

$$B_T = az_{max} + C1; \tag{4.24}$$

$$C_T = rn_{min} - C1; \tag{4.25}$$

$$D_T = rn_{max} + C1; \tag{4.26}$$

Where A_T and B_T are the boundaries in the azimuth, C_T and D_T are the ones in the range direction, az_{min} and az_{max} are the minimum and maximum pixel indices in the azimuth direction respectively and rn_{min}, rn_{max} are the minimum and maximum pixel indices in the range direction respectively (the coordinates origin is at the top-left corner). C1 is a constant offset from the candidate target minimum and maximum range indices. In this study, C1 is set to be one pixel to reduce the computational burden and to avoid including pixels from other close candidate targets.
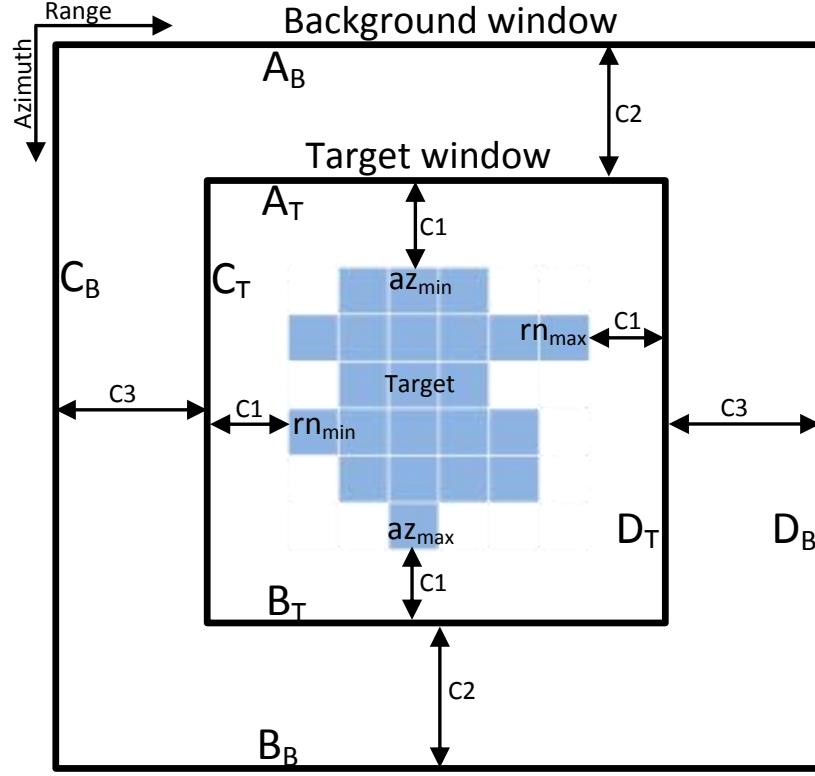
Figure 4.5: Window setup of the pre-screening stage second step. A_T B_T, C_T, D_T are the boundaries of the target window defined as in Eqns. 4.24 - 4.26. A_B, B_B, C_B, D_B are the boundaries of the background window defined as in Eqns. 4.28 - 4.30.

The boundaries of the background window are set as

$$A_B = A_T - C2; \tag{4.27}$$

$$B_B = B_T + C2; \tag{4.28}$$

$$C_B = C_T - C3; \tag{4.29}$$

$$D_B = D_T + C3; \tag{4.30}$$

Where A_B and B_B are the boundaries in the azimuth, C_B and D_B are the boundaries in the range direction. A_T, B_T, C_T, D_T are the boundaries of the target window. C2 and C3 are constant offsets from the target window boundaries. C2 and C3 can be equal or different according to the number of pixels in the range and azimuth directions of the image and according to the target position in the image. For instance, candidate targets near image boundaries and land mask require special window shapes and dimensions to ensure

99

appropriate pdf estimation of background data.

In the second pre-screening step, either one of two ATDs is used to threshold each pixel in the target window which contains the entire candidate target with a threshold. This threshold is determined adaptively so that a constant PFA is maintained over the entire image. These two ATDs are the LRT and the S_0-CFAR detectors. The selection between the two ATDs is made based on the total number of pixels of candidate target detected by the pre-screener first step. The number of detected pixels per candidate target is counted before passing the targets to the second pre-screening step. Since the target data pdf is to be estimated by the GMM method, there should be an adequate number of data points of the target. If the number of candidate target pixels is large enough, the LRT detector is used; otherwise, the CFAR one is used. More explanation about this number is given in Chapter 5.

The Stokes Parameters Likelihood Ratio Test Detector

The Stokes parameters LRT pre-screener is used to retest each candidate target against a threshold determined according to the local statistics of the background pixels surrounding the target at a specific PFA. The proposed LRT detector is formulated to use the joint pdf of the four Stokes parameters of ocean and candidate target data to generate the likelihood ratio (LR) instead of the traditionally used joint pdf of the scattering vector components. Then, at each pixel of the target window, the value of the likelihood ratio or a monotonic function of it is compared to a threshold determined at a specific PFA to decide on the object to which the pixel under test belongs. The determination of the threshold value isdiscussed in Sec. 4.8.2. When the LR value of the pixel exceeds the threshold, the alternative hypothesis is accepted and the pixel is related to a target. Otherwise, the null hypothesis is accepted which means that the pixel is related to the ocean.

After the candidate target is passed to the second pre-screening LRT step, the joint pdf of the four elements of the Stokes vector is estimated. The pixels of the background

window are used to estimate the Stokes parameters joint GMM pdf of ocean data. Similarly, all detected pixels within the target window are used for target (ship) Stokes parameters joint pdf estimation. The GMM algorithm estimates the joint pdf of the Stokes Parameters starting from k=1 and D = 4 (one multivariate Gaussian component), calculating the BIC and then increasing the number of components by one and then comparing the BIC of all models to choose the appropriate number of components which is related to the smallest BIC. This process is conducted one time for ocean pdf and another time for the ship pdf for each large candidate target. After the pdfs are estimated, the likelihood ratio is then calculated for each pixel in the target window. The likelihood ratio is defined as

$$LR_{SP}^{'}(x,y) = \frac{f_s(\mathrm{u(x,y)}; \theta_s)}{f_o(\mathrm{u(x,y)}; \theta_o)} \tag{4.31}$$

where $LR_{SP}^{'}(x,y)$ is the likelihood ratio value of the Stokes parameters (SP) at an image pixel with (x,y) pixel coordinates; $f_o(\mathrm{u(x,y)}; \theta_o)$ and $f_s(\mathrm{u(x,y)}; \theta_s)$ are the ocean and ship Stokes parameters joint pdfs values respectively at the (x,y) pixel, u is a 4-Dimensional vector of the Stokes parameters u $= [S_0 \quad S_1 \quad S_2 \quad S_3]^T$, θ_s and θ_o are the vectors of all components parameters of ocean and ship pdf respectively, where $\theta_s = (p_s, \mu_s, C_s)$ is the parameter vector of ship GMM and $\theta_o = (p_o, \mu_o, C_o)$ is the parameter vector of ocean GMM.

The value to be compared with the threshold is computed using the natural logarithm of Eq. (4.31) at each pixel of the target window using the estimated GMM SP joint pdfs for ocean and ships as in Eq. (4.32).

$$LR_{SP}(x,y) = \ln \left(\frac{\sum_{k=1}^{K_s} p_{s_k} \, g(\mathrm{u(x,y)}; \mu_{s_k}, C_{s_k})}{\sum_{k=1}^{K_o} p_{o_k} \, g(\mathrm{u(x,y)}; \mu_{o_k}, C_{o_k})} \right) \tag{4.32}$$

Where the subscript 'o' is related to ocean and the subscript 's' is related to ship joint pdf parameters. K_o and K_s are the number of Gaussian components in the ocean SP joint pdf and ship SP joint pdf respectively and (x,y) are the pixel's coordinates.

After the LR_{SP} (LR_{SP} is called hereafter as LR for simplicity) value is calculated for each pixel in the target window, it is then compared to a threshold and a decision is made

based on the rule:

$$(LR_{SP}(x,y) \geq \eta) = \begin{cases} 1 \implies & \text{target pixel} \\ 0 \implies & \text{ocean pixel} \end{cases} \tag{4.33}$$

Where $LR_{SP}(x,y)$ is the likelihood ratio value at the pixel (x,y) and η is the threshold value.

After the pre-screening stage, the re-detected targets are passed to the discrimination stage.

The Constant False Alarm Rate Detector

The CFAR detector is selected as a second step pre-screener when the number of detected pixels per candidate target is not adequate to be used for target pdf estimation. In the CFAR detector, the same window setup is used as for the LRT detector and the value of S_0 is reused again for testing candidate pixels. It is to be compared to a local S_0 value (threshold) and not to a global one as done in the first pre-screening step. The S_0 value of each pixel in the target window is compared to a threshold that is determined using the statistics of the local background included in the background window at a specific PFA. If the value of S_0 of the pixel exceeds the predefined threshold, it is considered that the pixel belongs to a target, otherwise it is considered that the pixel belongs to the ocean as in the following decision rule

$$(S_0(x,y) \geq \eta) = \begin{cases} 1 \implies & \text{target pixel} \\ 0 \implies & \text{ocean pixel} \end{cases} \tag{4.34}$$

where $S_0(x,y)$ is the S_0 value at the pixel (x,y) and η is the threshold value. It is worth mentioning that for both ATDs and for each candidate target, if any of its pixels is re-detected, then the target is considered detected. After all the candidates are retested by the second pre-screening step, they are passed to the discrimination stage. The discrimination stage is described in details in Sec. 4.8.3 after explaining the threshold determination process in the next section.

4.8.2 Threshold Calculation

The threshold values for both ATDs were determined at a specific PFA using ocean statistics of background pixels. In the LRT pre-screener, the threshold (η) is the value of the log-likelihood ratio LR_{SP} of ocean pixels that achieves a desired PFA value. We recall that the PFA equals the area under the tail of the ocean data pdf curve starting at a specific data value (η) as per Eqn. 4.35, [111].

$$\text{PFA} = \int_{\eta}^{\infty} \text{H}(l;\theta)\, dl \tag{4.35}$$

where $\text{H}(l;\theta)$ is the pdf of the ocean data (l). In the LRT case, $\text{H}(l;\theta)$ is the joint GMM pdf of the LR_{SP} of ocean pixels expressed as

$$H(l;\theta) = \sum_{k=1}^{K} p_k\, g(l; \mu_k, C_k) \tag{4.36}$$

where l is the ocean log-likelihood data vector, θ is the vectors of all components parameters of ocean log-likelihood pdf, and $\theta = (p, \mu, C)$ is the parameter vector of log-likelihood GMM.

For each large candidate target, first, Stokes vectors of all ocean pixels of the background window are substituted in the log-likelihood ratio of Eqn. 4.32 to obtain the data vector l. Then, the pdf of the ocean log-likelihood ratio is estimated using the GMM method as described previously. Finally, the commutative distribution function (cdf) is evaluated numerically at each value in the ocean set. As the area under the pdf curve equals 1, then the area under the tail is then evaluated according to the relation 4.37. After that, the threshold η is determined at a specific PFA by linear interpolation.

$$\text{Tail} = 1 - \text{cdf} \tag{4.37}$$

For the CFAR pre-screener, the threshold is determined by using the GMM pdf of ocean S_0 estimated by background pixels in a similar way. So, for the CFAR threshold, first, the ocean S_0 GMM pdf is estimated. Then, the cdf is calculated numerically and the distribution tail is evaluated after that accordingly. Finally, the threshold η is determined at a specific PFA
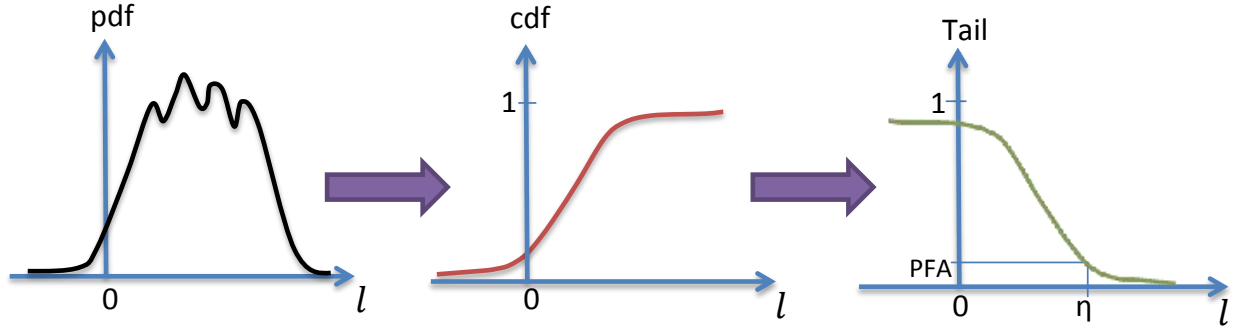
Figure 4.6: Procedures of threshold determination for the pre-screening stage of the detection algorithm. pdf is the GMM of the log-likelihood ratio (l), cdf is its corresponding cumulative distribution function and η is the threshold at a specific value of the PFA.

by linear interpolation. Figure 4.6 shows the procedures of threshold determination for the pre-screening stage of the detection algorithm.

 Pre-screening Stage of Candidate Targets Near Land Regions

Land region data is excluded using the land masking algorithm before applying the detection algorithm to the scene. However, candidate targets that are detected by the global thresholding step and located near land regions need special treatment in both second pre-screening step and discrimination stage. This is decided as the high reflections from land may interfere with ocean returns at these regions. In this section, we focus on the window set up for these candidates, while the special treatment related to the discrimination stage is deferred to Sec. 4.8.3.

After masking land regions, land pixel values are replaced by zeros. Thus, if the regular window setup, depicted in Figure 4.5, is used with targets close to land, ocean data pdf may be inappropriately estimated due to the large number of background pixels with zero values or the GMM algorithm may be unable to estimate the pdf at all. So, before passing the candidate targets to the second pre-screening step, the distance between the center of the detected target to all pixels on the perimeter of the land-mask is calculated for each candidate target. If the distance to any of these pixels is less than a pre-defined value, then

the background window is enlarged. Then, any candidate pixels or pixels with zero values are excluded before the estimation of ocean data pdf. The distance is set arbitrarily as will be shown in the results chapter. If the candidate is far from land, the regular window setup is used. After determining near and far candidates and setting window sizes, the appropriate ATD is selected to each candidate target.

4.8.3 The Discriminator: Child Parameters Analysis and Final Decision

For the purpose of reducing false alarms and as a final stage in the detection process, all re-detected targets from the previous stage are subjected to further child parameters analysis to classify the re-detected targets either as real ship or false alarm. The discrimination herein is based on the type of scattering mechanism of the candidate pixels. It is well known that the ocean exhibits dominantly surface scattering while ships may have hybrid scattering mechanisms (even, odd and volume) due to ship construction materials, superstructure, orientation with respect to radar beam and other factors. We also recall that there is a relationship between the physical scattering mechanism and the child parameters derived from the Stokes parameters [25]. This is exploited in the discrimination stage to distinguish between ship targets from surrounding ocean. Therefore, this approach is anticipated to improve the discrimination performance.

In this stage we use the degree of polarization m and the ellipticity (χ) for discrimination through the $m - \chi$ decomposition. The m and χ can be calculated from Stokes parameters as in Eqs. 4.5 and 4.6 respectively. After calculating m and χ and according to the $m - \chi$ decomposition described in Sec. 4.4, a color-coded (RGB) image is then constructed from three individual color (Red, Green and Blue) images [68] as in Eqns. 4.38 - 4.40. Each of the colors represents a scattering mechanism type: R represents the even bounce, B represents the odd bounce and the G represents volume scattering.

$$\text{B} = [mS_0(1 + \sin{(2\chi)})/2]^{1/2} \tag{4.38}$$

$$R = [mS_0(1 - \sin(2\chi))/2]^{1/2} \tag{4.39}$$

$$G = [(S_0(1 - m))]^{1/2} \tag{4.40}$$

Figure 4.7 shows the Red, Blue, Green and the combined RGB images of a ship in ocean built based on the $(m-\chi)$ decomposition. It is clear from the RGB image (the top rightmost part of Figure 4.7 that the sea surface pixels are dominated by the blue color which reflects the single bounce scattering. On the other hand, ship pixels color results from a mixture of the three colors with a percentage of each color that is proportional to the corresponding scattering mechanism strength at that pixel. This mixture can be one of seven classes as suggested by Raney in [96] and shown in Table 4.3. It is also noticed that the strength of all three colors for ship pixels is larger for ship pixels than ocean pixels.
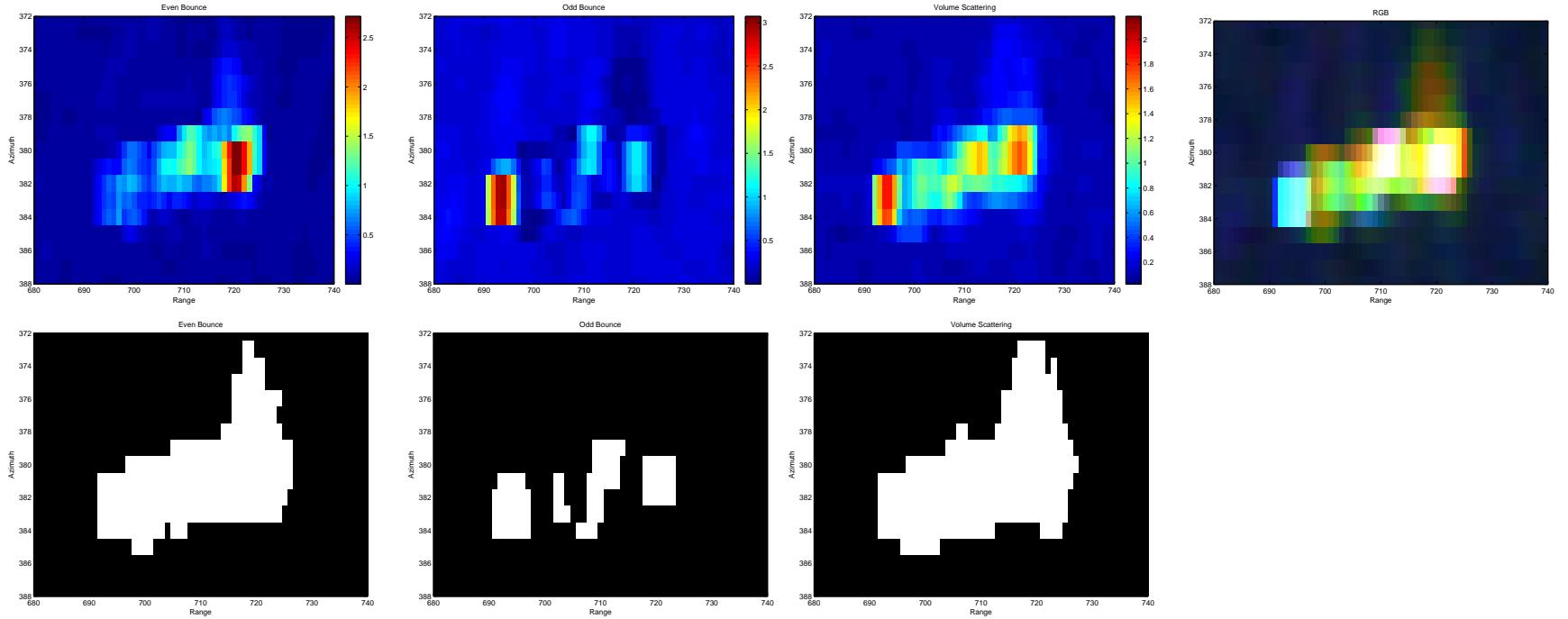
Figure 4.7: The original Red, Blue, Green, RGB and the Ŕ, B́, Ǵ and RGB images after thresholding of a ship with verified position in ocean. Top row from left to right: original Red. original Blue, original Green and original RGB images evaluated from Eqns. 4.38 - 4.40. Red image represents the even bounce scattering, Blue image represents the odd bounce scattering and Green image represents the volume scattering. Bottom row from left to right: Binary images resulted from thresholding the top row images: Ŕ, B́, Ǵ.

In order to quantitatively involve the $m - \chi$ decomposition to discriminate ships from falsely detected ocean clusters, three steps are introduced as follows:

1. Each of the R, B and G images is subjected separately to a thresholding process to generate three new binary images (Ŕ, B́ and Ǵ). So, for the R image, for instance, Ŕ image is generated using the rule

$$\text{Ŕ}(x,y) = \left\{ \begin{array}{lcl} 1 & : & \text{R}(x,y) \geq \eta_R \\ 0 & : & \text{R}(x,y) < \eta_R \end{array} \right\} \tag{4.41}$$

where η_R is the threshold of the Red image. The threshold of each color image is selected experimentally to be the maximum color strength of an ocean block of pixels. It has been found that most ship pixes values for the Red and Green colors exceed the maximum color strength of ocean pixels while only some ship pixels have Blue color values that are larger than the ocean pixels as seen from Figure 4.7 which shows the Ŕ, B́ and Ǵ and the RGB image for a ship in ocean.

2. Each pixel in the three binary color images (Ŕ, B́, Ǵ) are jointly compared to a three binary digit patterns to construct another binary image called the discrimination image $d(x, y)$. Each of the patterns correspond to a single or a combination of scattering mechanisms. As we have 3 binary images, there are 8 possible combinations that a pixel can take. These combinations are depicted in Table 4.3. In order to distinguish between ships and false alarms, we compare each pixel's value in the three binary images to five of the patterns shaded in gray color in Table 4.3. The pattern "ŔǴB́ = 000" is rejected as it indicates that the pixel is from ocean according to the thresholding process which gives 0 for ocean pixels with low color strength. The pattern "ŔǴB́ = 001" is also rejected which reflects only high single bounce scattering which may results from an ocean pixel. The pattern "ŔǴB́ = 100" is also rejected as we found by experiment that ship ghosts has high double bounce strength. Ship ghosts appear in SAR images as a line of bright pixels along the range direction due to the high reflectivity of ship pixels [112]. Figure 4.8 shows the Red,

108

Blue, Green and the combined RGB images built based on the $(m - \chi)$ decomposition of a ship and its ghost in the top row. The bottom row of Figure 4.8 shows the Ŕ, B́, Ǵ after thresholding. It is obvious from these images that the Blue and Green color strength of ship ghost is low and below the threshold of each color. This is confirmed from the binary images of the thresholded Blue and Green images as all ghost pixels have zero values. On the other, it is clear from the Red and the RGB images that the Red color strength (the even bounce scattering) is higher than the red threshold. Thus, ship ghost can be detected incorrectly as ships. Therefore, it is seen to exclude the "ŔǴB́ = 100" pattern from the comparison.

So, if a pixel's binary pattern coincides with one of the four patterns "ŔǴB́ = [111, 110, 010, 101, 011]" , then 1 is placed in that pixel of the discrimination image; otherwise 0 is placed.

Table 4.3: All possible patterns that a pixel can have in the three binary color images (Ŕ, B́ and Ǵ). Gray shaded patterns only are to be compared with the (Ŕ, B́, Ǵ) images pixels. The 'db' stands for the double bounce; the 'vs' for the volume scattering and the 'bs' for the Bragg scattering or the odd bounce scattering mechanism (Scattering Mech.)

Ŕ	Ǵ	B́	Scattering Mech.
0	0	0	-
1	0	0	db
0	1	0	vs
0	0	1	bs
1	1	0	db + vs
1	0	1	db + bs
0	1	1	vs + bs
1	1	1	db + vs + bs
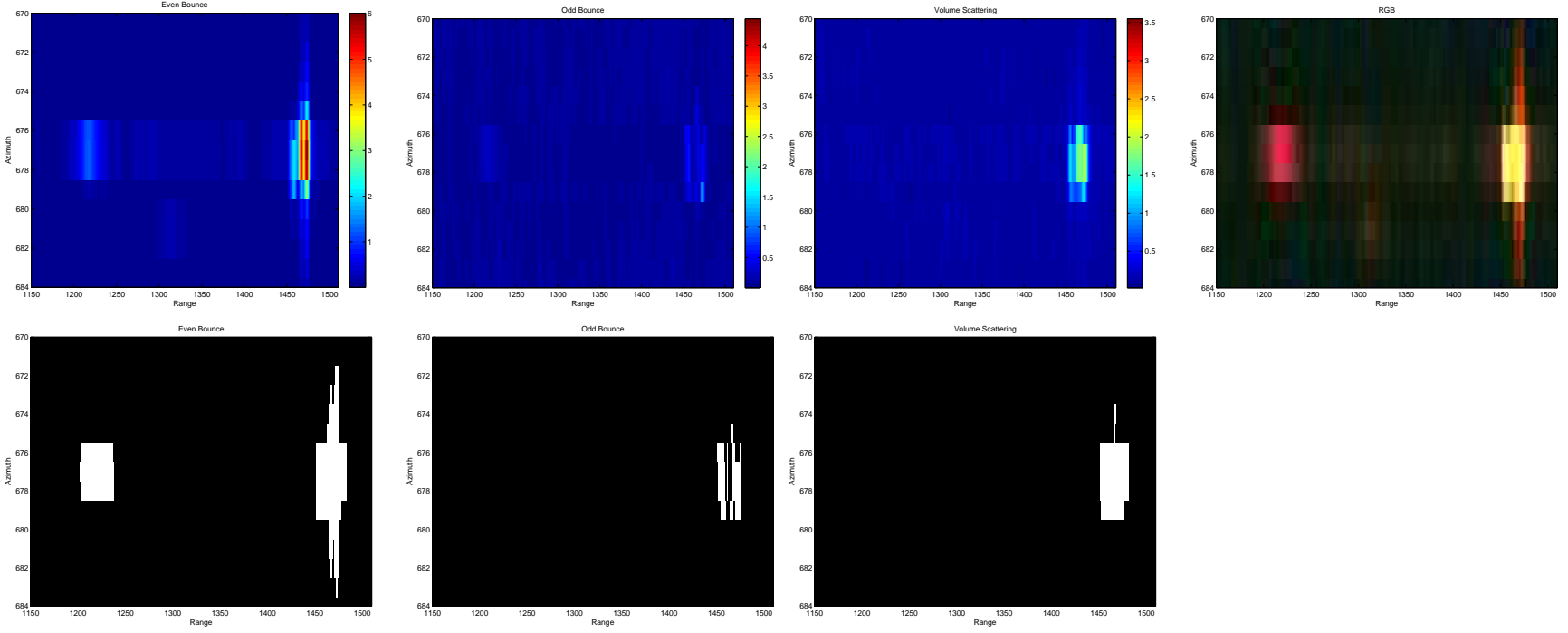
Figure 4.8: The original Red, Blue, Green, RGB and the Ŕ, Б́, Ǵ and RGB images after thresholding of a ship with verified position and its ghost. Top row from left to right: original Red. original Blue, original Green and original RGB images evaluated from Eqns. 4.38 - 4.40. Red image represents the even bounce scattering, Blue image represents the odd bounce scattering and Green image represents the volume scattering. Bottom row from left to right: Binary images resulted from thresholding the top row images: Ŕ, Б́, Ǵ.

3. Finally, all pixels of each detected target resulting from the pre-screening stage are compared with their corresponding values in the discrimination image $d(x,y)$ according to the condition 4.42; i.e. if a target pixel is detected by both pre-screener and discriminator, then the pixel is declared a ship pixel,

$$[t_d(x,y) \ \&\& \ d(x,y)] = \left\{ \begin{array}{ll} 1 \Longrightarrow & \text{ship pixel} \\ 0 \Longrightarrow & \text{false alarm} \end{array} \right\} \tag{4.42}$$

where, $t_d(x,y)$ is the value of the pixel (x,y) in a detected target.

4. When all pixels in a given target are rejected according to the above discrimination condition, then this target is considered a false alarm. On the other, when any of the pixels within a target is accepted, then the entire target is considered a ship.

Discrimination of Target Candidates Near Land Regions

Near-land candidates need a special treatment in the discrimination stage like the pre-screening stage. Near shores, there is high reflections from land that may interfere with backscattering from ocean thus providing bright pixels that may be falsely detected as ships by the pre-screeners. Therefore, more strict condition should be applied in the discrimination process for targets detected at these regions. That is, only candidate pixels having strong strength of the three colors (all three types of the scattering mechanisms) are accepted as ship pixels. In other words, detected pixels with values coinciding with the pattern "ŔǴB́ = 111" are considered from a ship; otherwise, it is deemed as false alarm.

4.9 Detection Performance Assessment of the Hybrid Ship Detection Algorithm

The output of the proposed detection algorithm is a set of targets declared as real ships. In order to assess the detection performance of the developed algorithm, the final detections

should be confirmed as ships by verification data. However, not all ships in the ocean carry AIS transponders. Therefore, it is expected that some of these final detections be ships with no verification data. These detections will be called in the results chapter the "extra targets". In fact, without the verification data, it is not possible to confirm that these targets are real ships even if multiple different detection algorithms are applied to the same data. This is because no two detectors give the same final detections when applied to exactly the same scene [8]. Therefore, we will assess the detection performance using only ships with verified positions and not taking extra detections into consideration in the assessment operation.

In each scene, there were a considerable number of ships with verified positions given by the AIS data available with the RS-2 scenes. AIS positions for ships located exactly at the shoreline was ignored since these ships were masked out by the land masking algorithm as a part of the shoreline before the application of the ship detection algorithm. Moreover, monitoring ships near the shoreline is less important than ships sailing far in the ocean. Put in a different way, ships at the shoreline maybe guarded by terrestrial surveillance methods like shore-based radars. However, SAR-based ship surveillance is necessary to monitor ships outside the field supervised by the terrestrial surveillance methods.

To assess the detection performance, the percent ratio of the detected ships with verified positions to the total number of ships with AIS positions is calculated. This percent ratio is called "the verified detection rate (VDR) percentage" defined as in Eqn. (4.43). The VRD shows how many ships with validated positions are correctly detected by the detection algorithm.

$$\text{VDR\%} = \frac{\text{number of detected ships with verified AIS positions}}{\text{total number of ships with verified AIS positions}} * 100 \qquad (4.43)$$

4.10 Conclusion

In this chapter, a new ship detection algorithm for CP SAR was introduced. Moreover, the basics and theoretical concepts related to this algorithm are reviewed. The proposed

algorithm combines four detection techniques together to improve the detection performance. The proposed detection algorithm has a pre-screener and a discriminator. The pre-screener of the algorithm is a hybrid one that employs three detection methods: global thresholding, Stokes LRT and S_0-CFAR. In the first pre-screening step, a global thresholding process is utilized to highlight all possible target candidates. In the second pre-screening step, the detected candidates are retested by using either the Stokes parameters LRT or the S_0-CFAR detectors. The selection between these two pre-screeners is made according to the size of the candidate target. The GMM approach is used to estimate the joint pdf of the Stokes parameters for the LRT detector for ocean and ship data and for the Stokes S_0 of ocean data. The discriminator of the proposed algorithm uses the m-χ decomposition technique to distinguish ships from false alarms.

This study is performed on simulated RCM SAR data in the Medium and Low Resolution and the Ship Detection modes. The performance of the proposed algorithm is assessed by comparing the number of detected ships with verified positions to the total number of ships with AIS positions. Results and conclusions of this study are presented in Chapter 5.

Chapter 5

Hybrid Ship Detection Algorithm for CP SAR

Results and Discussion

In this chapter, the results of applying the proposed hybrid ship detection algorithm to a number of RS-2 scenes are introduced. After presenting the results, conclusions are drawn accordingly. This chapter is organized as follows. In Sec. 5.1, parameters setup of the GMM algorithm are discussed. Sec. 5.2 presents the setup of the detection algorithm parameters and the detection results for the Medium Resolution RCM mode data. The detection results of the Low Resolution RCM mode are introduced in Sec. 5.3 and the results of the Ship Detection mode are given in Sec. 5.4. Finally, in Sec. 5.5, concluding remarks are made about the presented work.

5.1 GMM pdf Estimation Algorithm Setup and Results

For the Stokes parameters LRT pre-screener, the GMM algorithm is run twice for each candidate target: once for the estimation of ocean Stokes data joint pdf and another for target's Stokes data joint pdf. The input to the GMM algorithm is the 4-D Stokes vector of the data pixels for which the pdf is to be estimated and the output is the joint Stokes parameters pdf of that data. After the likelihood ratios of all background pixels are computed, they are fed to the GMM algorithm to estimate ocean LR pdf as required to determine the adaptive threshold at the desired PFA.

For the S_0-CFAR pre-screener, the algorithm is run once for the estimation of ocean S_0 pdf using background window pixels. This pdf is used to determine the required threshold at a specific PFA. In order to reduce missing ships, the PFA is selected to be relatively high;

that is to be 10^{-6} at all candidate clusters for both LRT and CFAR detectors.

For both ATD pre-screeners, the number of components (k) is set to 1 at the beginning and it is then increased by 1 till reaching an arbitrarily large value. At each k, the BIC is calculated and stored. After that, the model with the lowest BIC is selected to be the best fit to the data. At each k, the initial mixing probabilities are set to be equal for all components: k observations from the data are selected at random as the initial component means and variances. This setup of the GMM algorithm is the same for all three RCM modes.

In the second pre-screening step, either one of two ATDs is used to threshold each pixel in the target window. These two detectors are the LRT and the CFAR detectors. The selection between the two ATDs is made based on the total number of pixels per candidate target detected by the pre-screener's first step. If the number of candidate target pixels is larger than 40 pixels, the LRT detector is used; otherwise, the CFAR is used. Although, more data points is preferred for accurate pdf estimation, a trade-off between adequate number of data points for accurate pdf estimation and the speed of the detection algorithm should be made. In other words, the more data points used for the pdf estimation, the more number of components need to be tested for the selection of the best GMM of the data by the BIC criteria, and consequently, the more run time the algorithm takes per detected candidate which may affect its validity for near real time results.

A sample of the Gaussian Mixture Modeling of ocean S_0 data, from an ocean subset extracted from the Low Resolution mode data, is shown in Figure 5.1. Another sample GMM results for ocean likelihood ratio (LR) data in the Ship Detection RCM mode is shown in Figure 5.2. In these figures, the top subplots present the number of GMM components (N_c) versus their corresponding BIC values. The middle subplots show the 1-D pdf and the histogram of ocean S_0, while the bottom subplots present the cdf and tail probability. It is clear from Figure 5.1, that the BIC values of the S_0 pdf start high and then decrease to a minimum and then increase as the number of components increases. The minimum BIC

value corresponds to the best fit to the data. The GMM of this S_0 data has 3 components. From the middle subplot of Figure 5.1, one can visually observe the goodness of fit of the GMM pdf for the S_0 data. The bottom subplot of Figure 5.1 shows the tail of the GMM pdf that is used to determine the threshold of the CFAR detector.

For the ocean LR data, it is obvious from the top subplot of Figure 5.2 that the general decrease-then-increase behavior of the BIC values with the increase in the number of components for the LR GMM is similar to that of the S_0 case. However, the BIC values suffer from fluctuations starting at k = 2 till k = 10 and then the BIC values start to increase linearly with the number of components increase. The GMM pdf of this LR data has 5 components. The goodness of fit of the GMM pdf for the LR data can visually be observed from the middle subplot. One can see from this subplot how the GMM approach is able to clearly describe the nature of LR data. The bottom subplot shows the range of the threshold values of the LRT detector.

Figure 5.3 shows the Gaussian Mixture Modeling of the joint pdf for ocean and ship Stokes parameters data in the Medium Resolution RCM mode. The left subplot shows the number of Gaussian components (N_c) of ocean Stokes joint GMM against the corresponding BIC values. In the right subplot, the (N_c, BIC) relation is depicted for Ship Stokes parameters joint GMM. It is obvious that for the ocean joint Stokes case, the BIC values have a similar general trend to that of the ocean LR. Nevertheless, it is noticed that ship data BIC values start high, fluctuate with a decreasing trend till reaching a minimum and then increase with fluctuation with the number of Gaussian components increase. This observation may be attributed to the high variability in ship backscatter along with the multidimensional pdf estimation of the Stokes parameters 4-D data. For this data set, ocean joint GMM pdf has 13 components while ship joint GMM has 24 components.
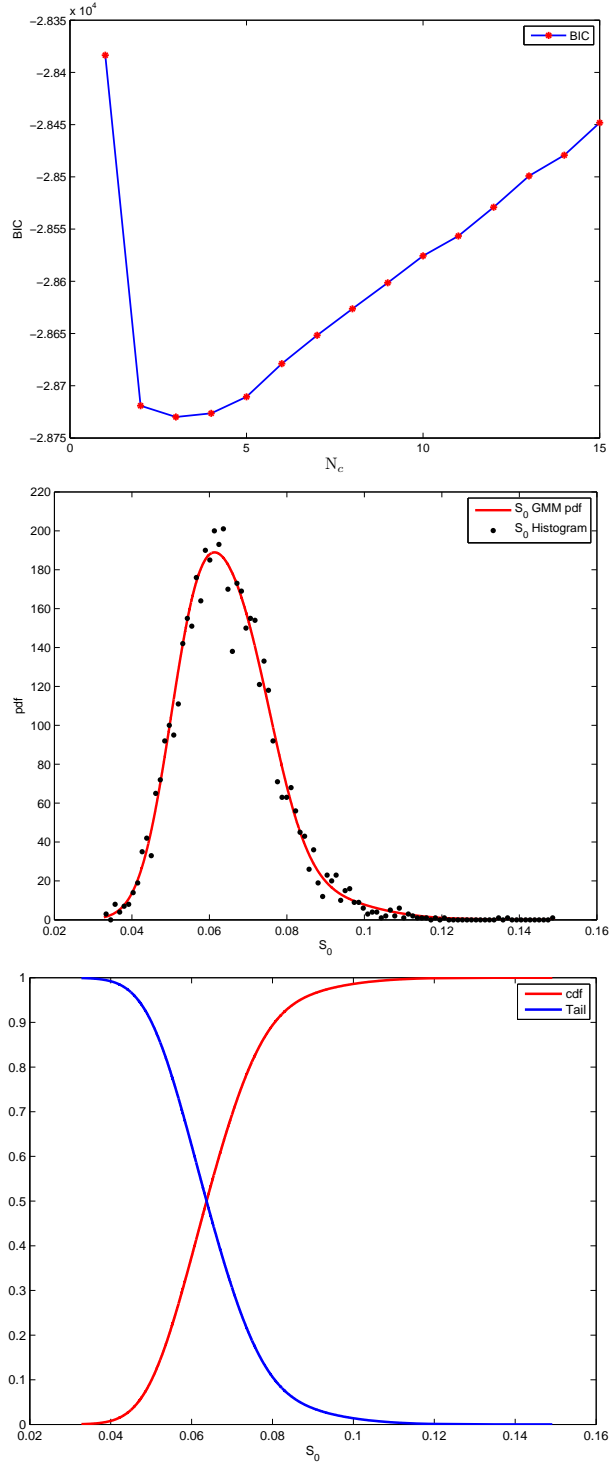
Figure 5.1: *Low Resolution RCM mode* : Gaussian Mixture Modeling of ocean S_0 data. Top: Number of Gaussian components (N_c) of S_0 GMM against BIC values. Middle: ocean S_0 pdf (3 components GMM) and histogram. Bottom :ocean S_0 cdf and tail probability. The GMM of this S_0 data has 3 components which corresponds to the minimum BIC. The goodness of fit of the GMM pdf for this ocean S_0 data can be seen from the middle subplot and the range of threshold values of the CFAR detector can be seen from the bottom subplot.
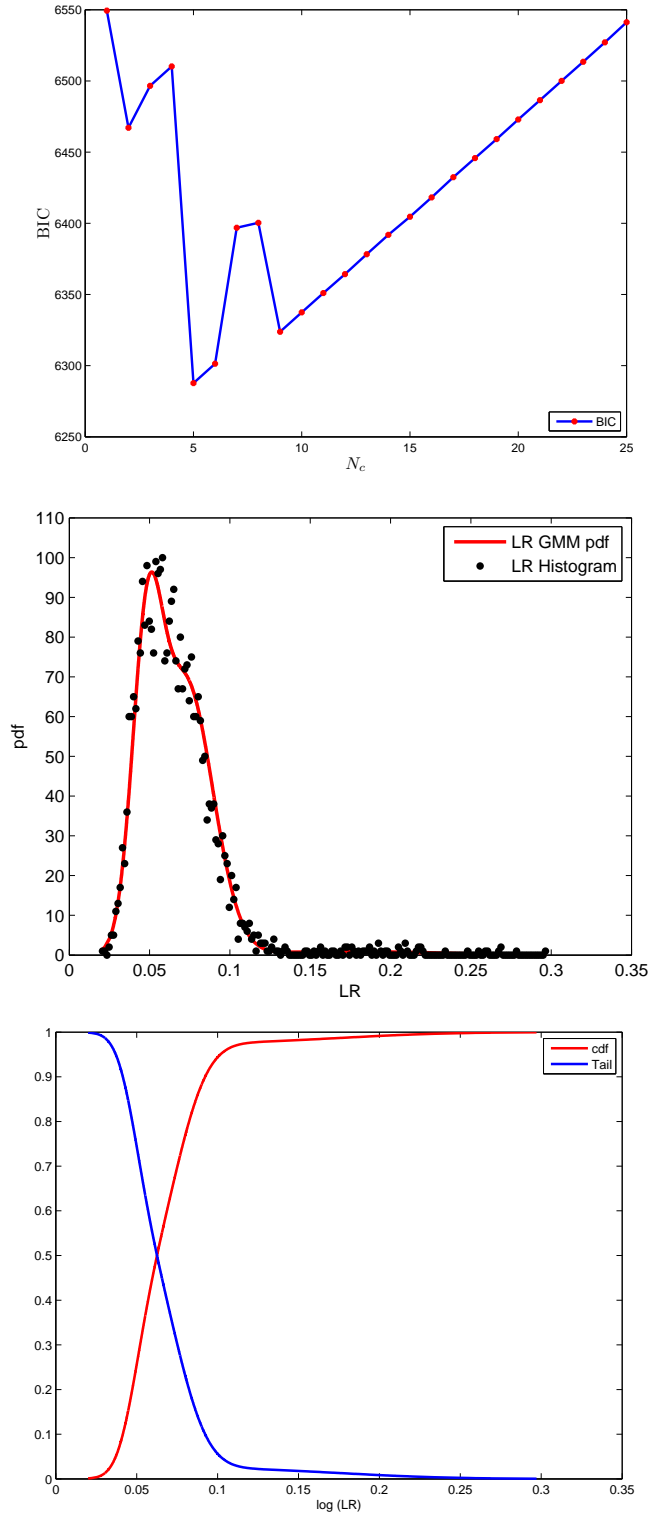
Figure 5.2: *Ship Detection RCM mode* : Gaussian Mixture Modeling of ocean LR data. Top: Number of Gaussian components (N_c) of ocean LR GMM against BIC values. Middle: ocean LR pdf and histogram. Bottom: ocean LR cdf and tail probability. The GMM of this ocean LR data has 5 components which corresponds to the minimum BIC. The goodness of fit of the GMM pdf for this ocean LR data can be seen from the middle subplot and the range of threshold values of the Stokes LRT detector can be seen from the bottom subplot.
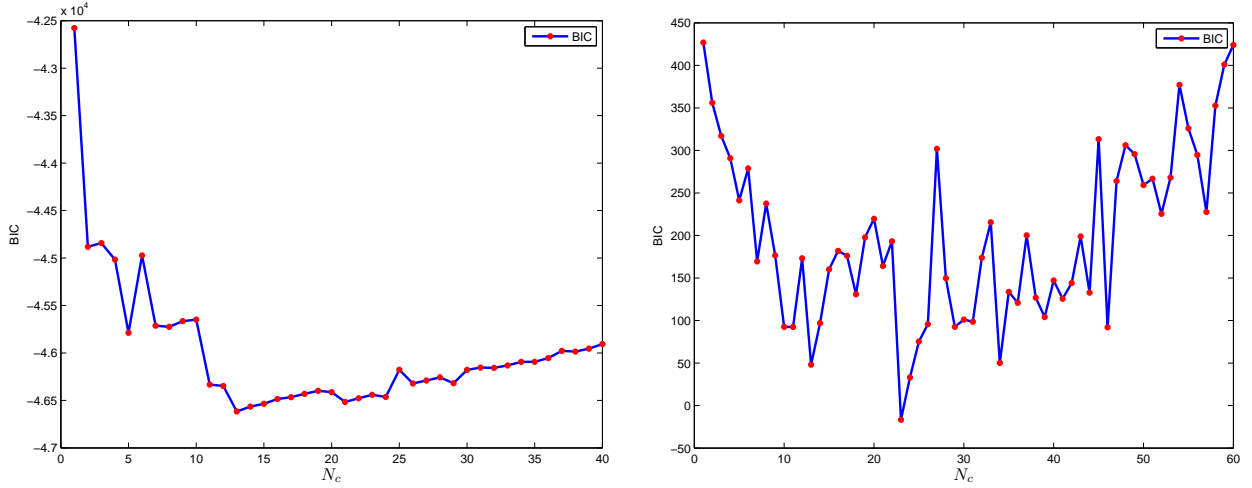
Figure 5.3: *Medium Resolution Mode* : Gaussian Mixture Modeling of the joint pdf for ocean and ship Stokes parameters data. Left : Number of Gaussian components (N_c) of ocean LR GMM against BIC values for joint pdf of ocean Stokes parameter data. Right : Number of Gaussian components (N_c) of ship Stokes GMM against BIC values.

5.2 The Medium Resolution RCM Mode Results

### 5.2.1 Setup of Detection Algorithm Parameters

First step Pre-screening stage

In order to determine the global threshold required for this step, a block of (400×400) ocean pixels with no targets is extracted from each scene. Then, the maximum S_0 value of the ocean pixels is taken to be the global threshold.

Target and Background Windows Setup

For the Medium Resolution mode, the regular target window has an offset from the maximum and minimum range and azimuth target boundary pixels of 1 pixel (C1 = 1). However, the background window offsets from the target window, C2 and C3, are equal and are set to 10 pixels. These values are selected to achieve both accurate ocean data pdf estimation for the smallest candidate target of one pixel and to facilitate fast run of the pre-screener algorithms. For near-land candidates, C1 remains the same as for far-from-land targets while C2 and C3 is enlarged to 30 pixels to ensure adequate non-zero data points for accurate ocean data pdf

119

estimation.

5.2.2   Detection Results

The detection results of each pre-screening step and the discrimination stage applied to Scene 1 is shown in Figure 5.4. In Figure 5.4, red squares represent the verified position of ships, green stars represent candidate targets detected by the global thresholding first pre-screening step, yellow crosses represent detected targets after the ATD pre-screeners and the white dots represent the final detections after the discrimination stage. The top left subplot of Figure 5.4 shows the detections of the first pre-screening step (global thresholding). The top right subplot shows the detections of the second pre-screening step (CFAR and Stokes LRT ATDs). The bottom subplot presents the final detections after discrimination stage (child parameters analysis). It is clear that the number of candidate targets is large after the first pre-screening step which is attributed to the global thresholding process. The number of re-detected targets by the ATD pre-screeners is less than that of the first pre-screening step after taking the effect of local sea state in determining the threshold of each ATD. However, after the child parameter analysis of the discrimination stage, all ships with verified positions are properly detected with two more extra targets. These two targets were declared by the discrimination stage to have a strong hybrid scattering mechanism which is highly unlikely to be from ocean clusters but may result from ships (with no verified positions) or other maritime objects like buoys.
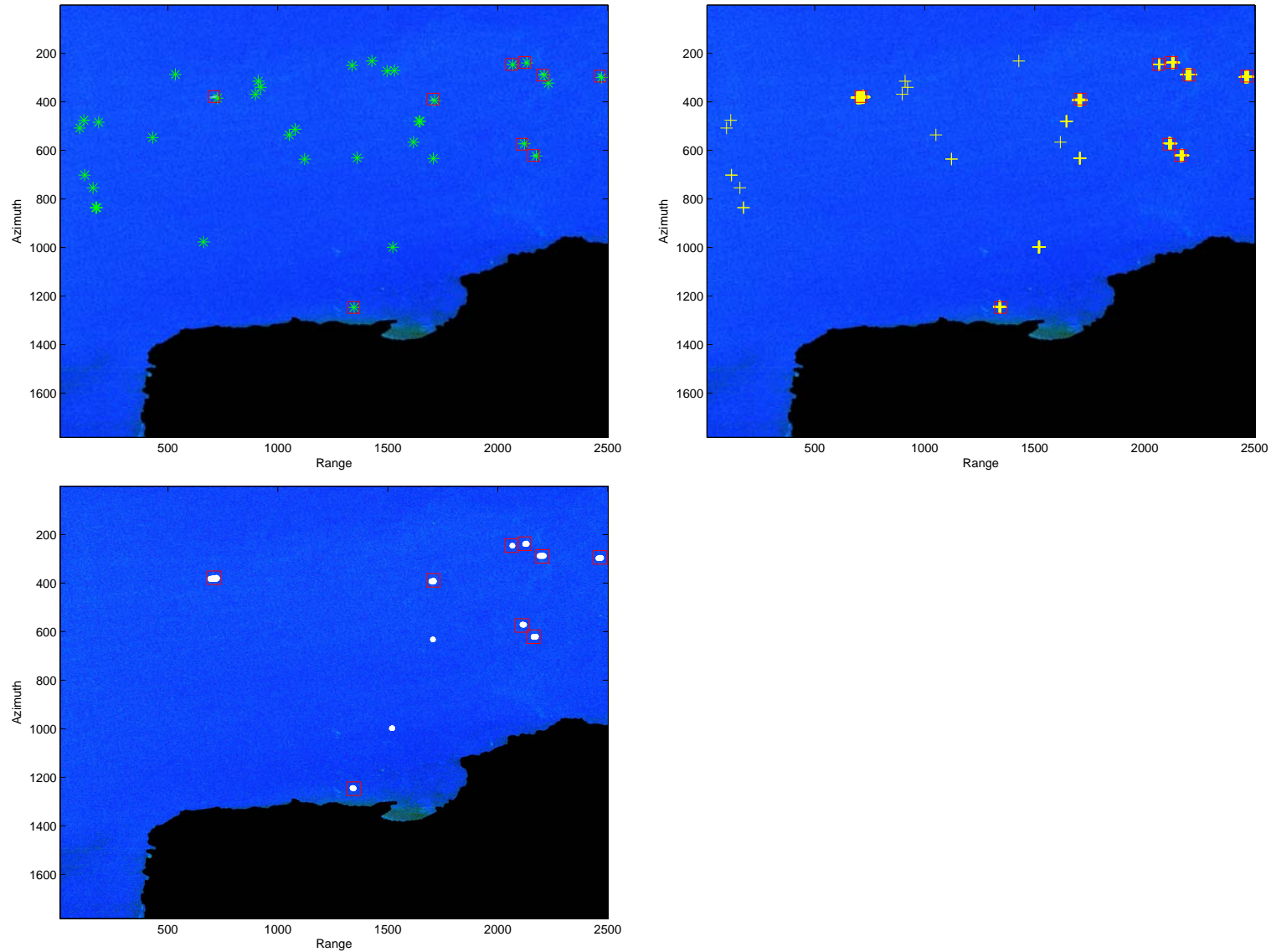
Figure 5.4: *Medium Resolution RCM mode* : Detection results of applying the hybrid detection algorithm stages to Scene 1. Red squares represent the verified positions of the ships, green stars represent the candidate target detected by the global thresholding first pre-screening step, yellow crosses represent the detected targets after of the ATD pre-screeners and the white dots represent the final detections after the discrimination stage. Top left : results of the first pre-screening step (global thresholding). Top right: results of the second pre-screening step (CFAR and Stokes LRT ATDs). Bottom: final detections after discrimination stage (child parameters analysis). Detections are superimposed on the RGB images of the $m - \chi$ decomposition.

The final detection results of all six scenes in the Medium Resolution RCM mode are shown in Figure 5.5 to Figure 5.10. The number of detected targets after each stage is shown in Table 5.1 for all scenes. The table entries represent the number of detections after the first pre-screening step (1st Pre-scr.), the second pre-screening step (2nd Pre-scr.) and the final detections after the discrimination stage. The final detections are sorted as detections with AIS positions (AIS(D)), missed detections with AIS positions (AIS(M)) and extra detections (Ext.). The total number of detections and the Verified Detection Rate (VDR) percentage are also shown for each scene. It is clear that, for all scenes, the number of total final detections is much less than that after the pre-screening stage. Put differently, in all scenes of this mode, the number of detections from the pre-screening stage ranges from 1.3 to 2.3 times more than the total number of final detections. This may be attributed to the fact that the pre-screening stage relies on the brightness of the pixel relative to the neighboring ocean pixels. So, some detections may be bright speckles pixels of ocean but detected as candidate targets by the pre-screener. However, the discrimination stage distinguishes between targets and ocean according to the scattering mechanism which significantly reduces potential false alarms. It is also noticeable that the numbers of detections after the first and second pre-screening steps are close and in some cases are equal. This may be due to the nearly homogeneous sea state over the entire scene for all scenes and the smoothing effect of spatial averaging. Overall, the detection algorithm is able to detect all ships with verified positions with a VDR percentage of 100%. Moreover, it is noticed that the number of extra detections which may correspond to other maritime objects in all scenes, except scenes 5 and 6, is relatively low.

Table 5.1: *Medium Resolution RCM mode* : Number of detections after applying all stages of the hybrid detection algorithm to all scenes. The table entries represent the number of detections after the first pre-screening step (1st Pre-scr.), the second pre-screening step (2nd Pre-scr.) and the final detections after the discrimination stage. The final detections are sorted to detections with AIS positions (AIS(D)), missed detections with AIS positions (AIS(M)) and extra detections (Ext.). The total number of detections and the Verified Detection Rate (VDR) percentage are also shown for each scene. The last row presents the total number of detections over the six scenes after each detection stage.

Scene	1st	2nd	Final Detections			Total No.	VDR
No.	Pre-scr.	Pre-scr.	AIS(D)	AIS(M)	Ext	Det.	
1	37	25	9	0	2	11	100%
2	15	15	8	0	1	9	100%
3	21	21	11	0	2	13	100%
4	35	35	11	0	6	17	100%
5	129	110	54	0	11	65	100%
6	102	99	54	0	10	64	100%
Tot.	339	305	147	0	32	179	100%

Figure 5.5: *Medium Resolution RCM mode* : Final detections of Scene 1 detected by the hybrid detection algorithm superimposed on the RGB images of the $m - \chi$ decomposition. Red squares represent the verified position of the ships and white dots represent the final detections.
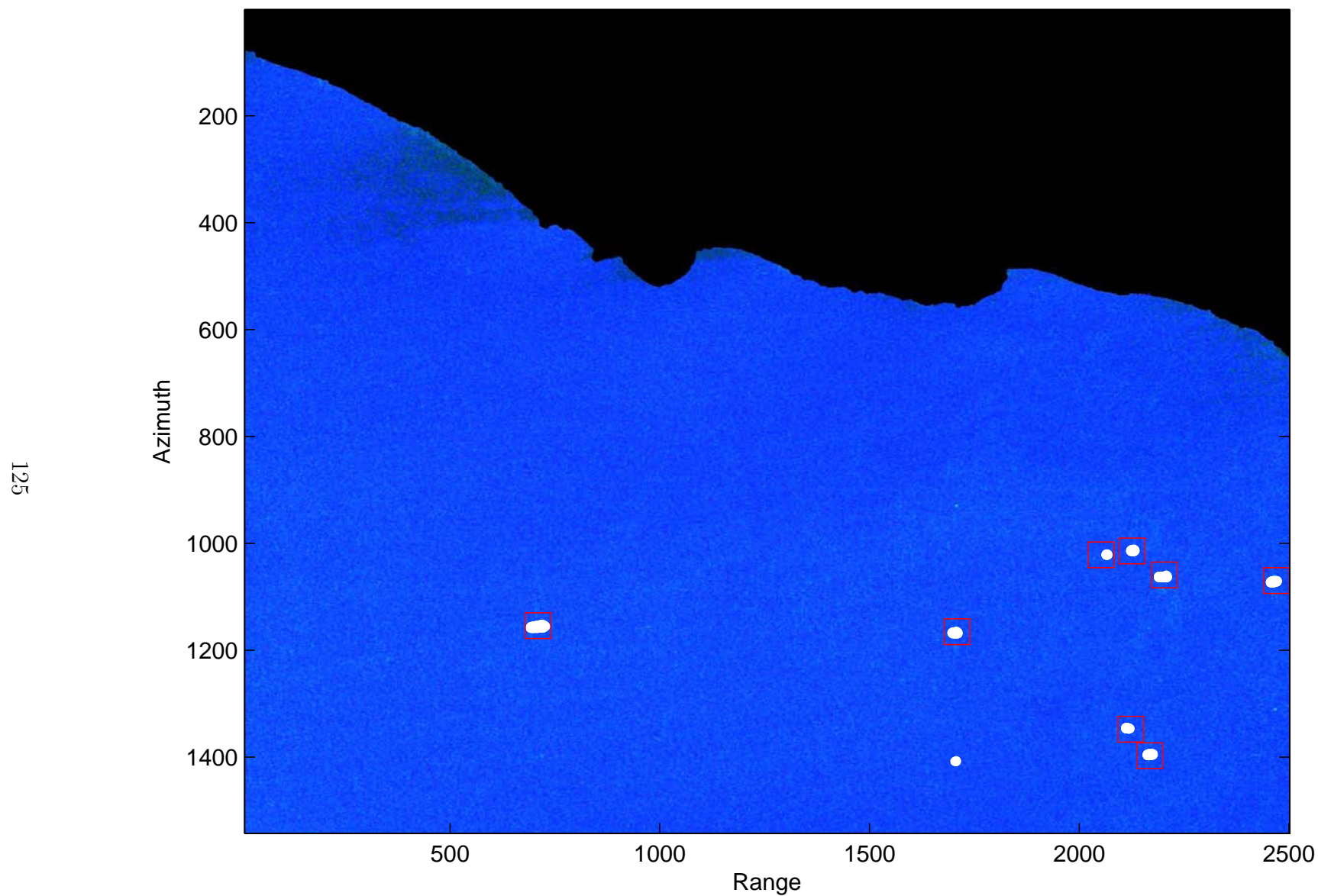
Figure 5.6: *Medium Resolution RCM mode* : Final detections of Scene 2 detected by the hybrid detection algorithm superimposed on the RGB images of the $m - \chi$ decomposition. Red squares represent the verified position of the ships and white dots represent the final detections.
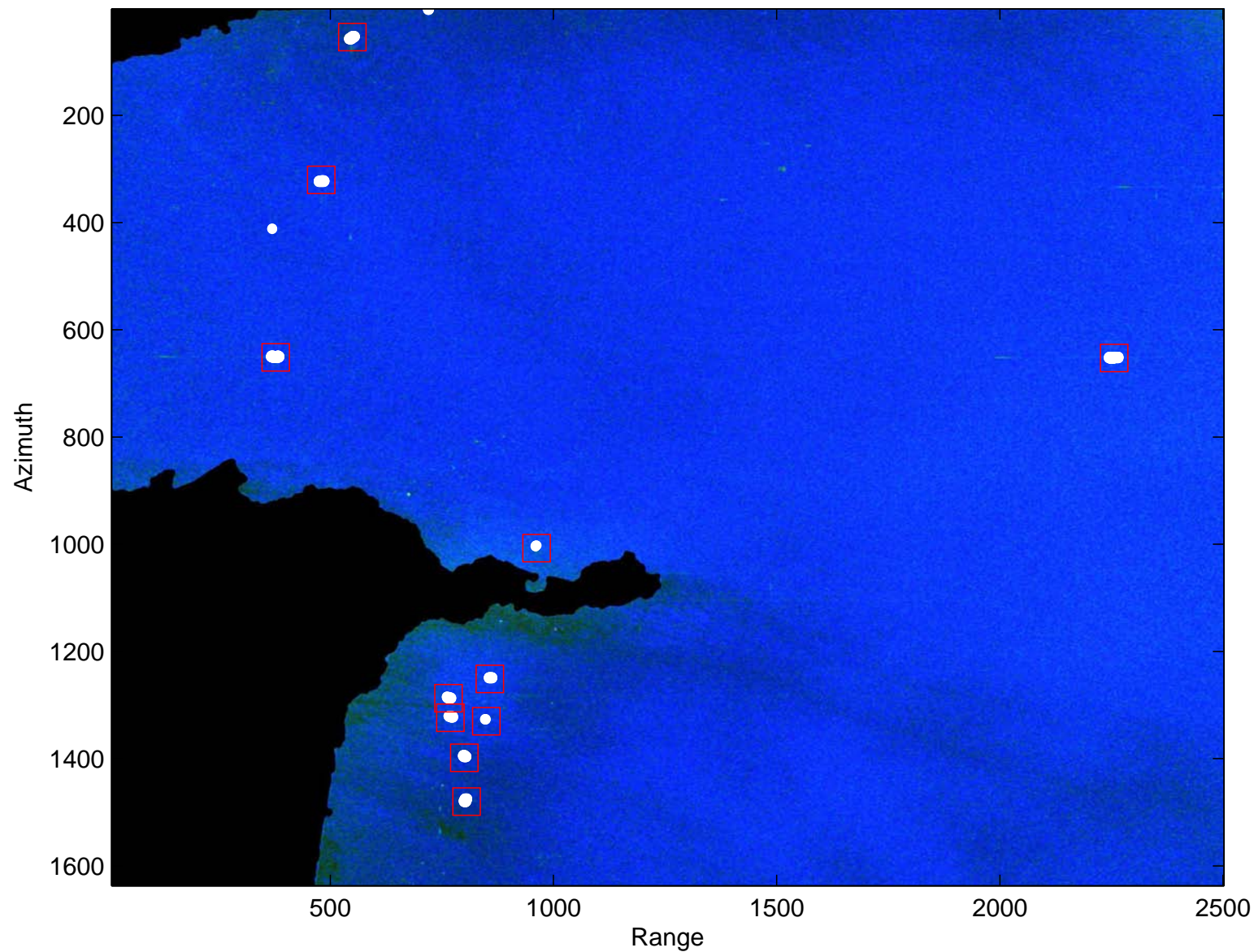
Figure 5.7: *Medium Resolution RCM mode* : Final detections of Scene 3 detected by the hybrid detection algorithm superimposed on the RGB images of the $m - \chi$ decomposition. Red squares represent the verified position of the ships and white dots represent the final detections.
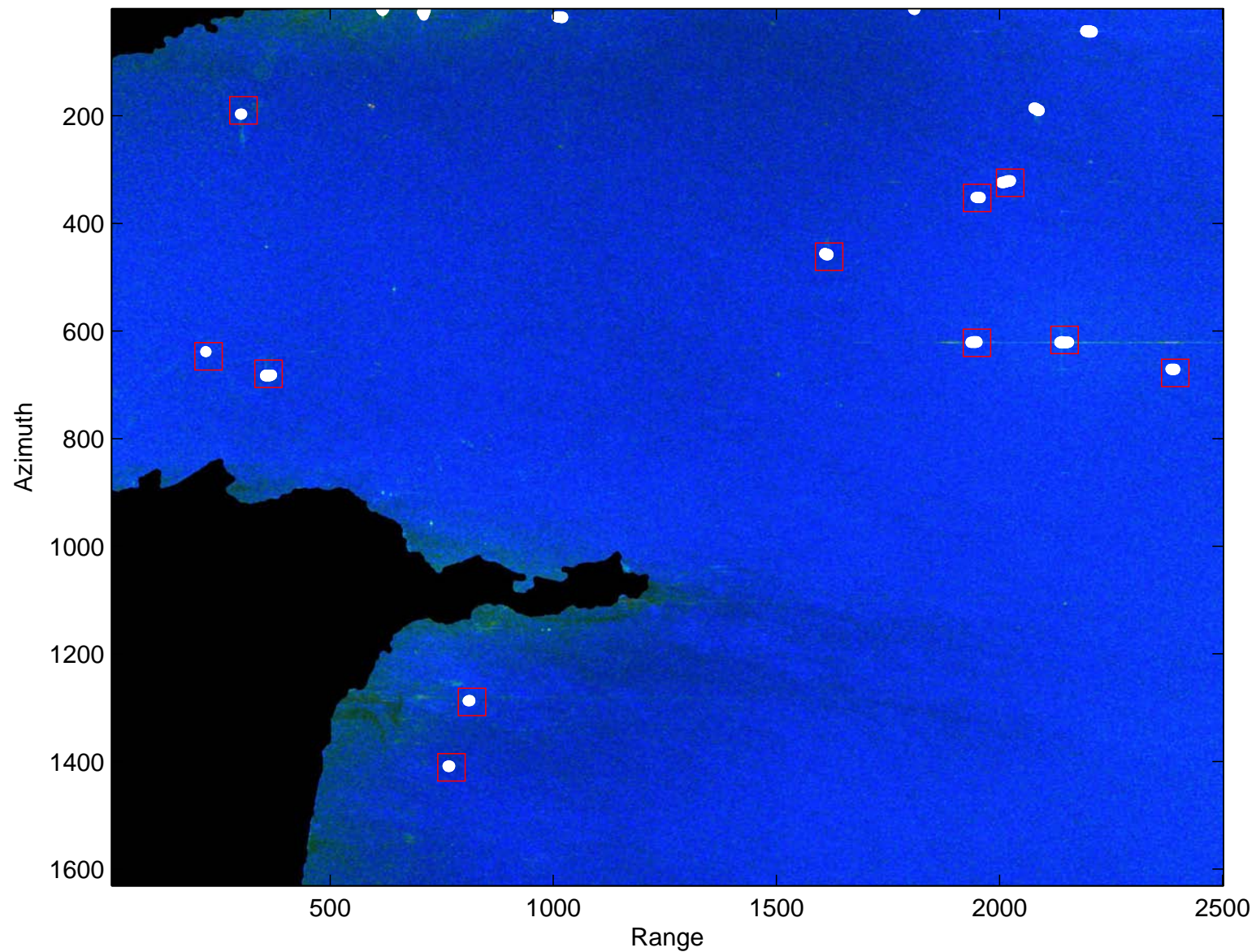
Figure 5.8: *Medium Resolution RCM mode* : Final detections of Scene 4 detected by the hybrid detection algorithm superimposed on the RGB images of the $m - \chi$ decomposition. Red squares represent the verified position of the ships and white dots represent the final detections.

Figure 5.9: *Medium Resolution RCM mode* : Final detections of Scene 5 detected by the hybrid detection algorithm superimposed on the RGB images of the $m - \chi$ decomposition. Red squares represent the verified position of the ships and white dots represent the final detections.
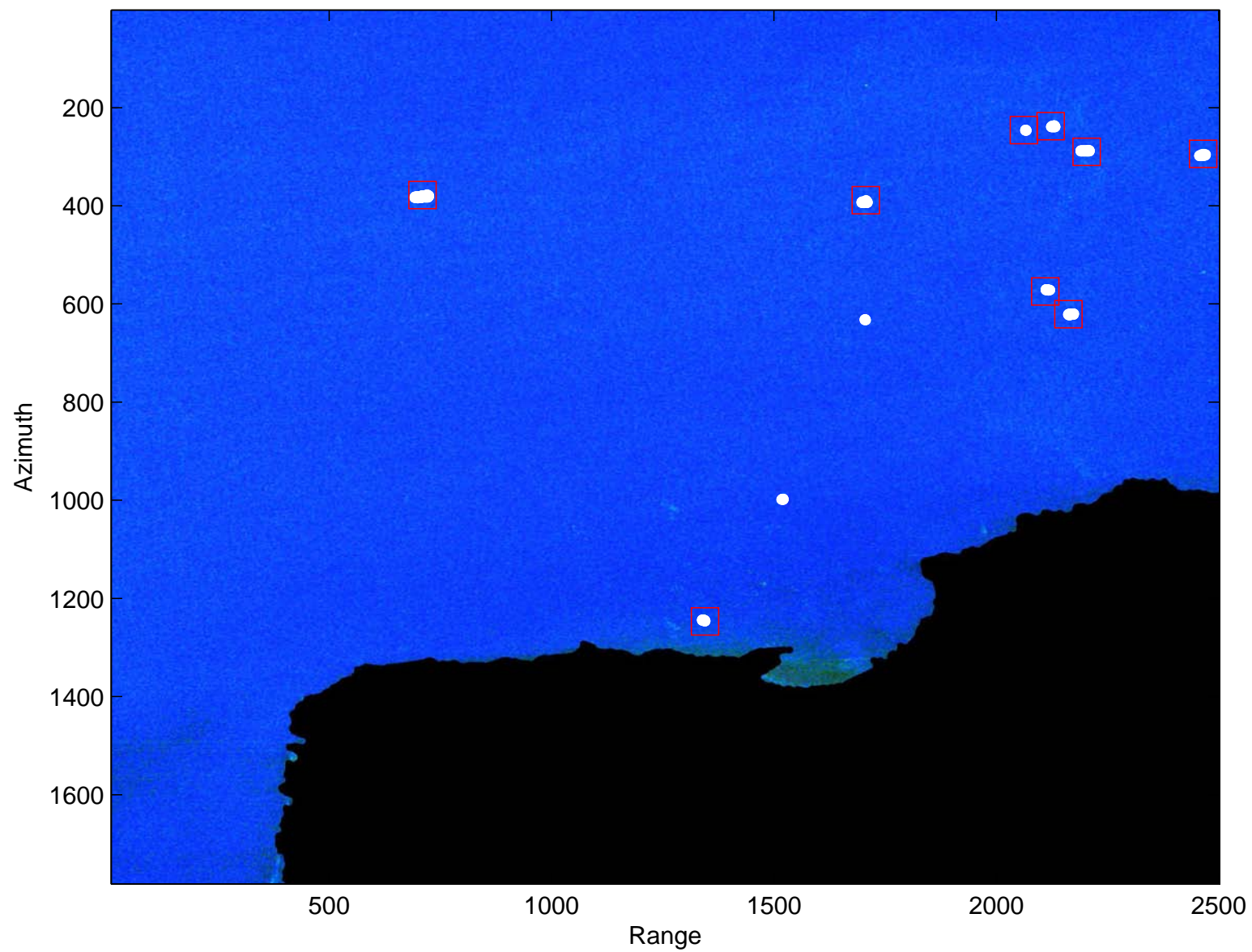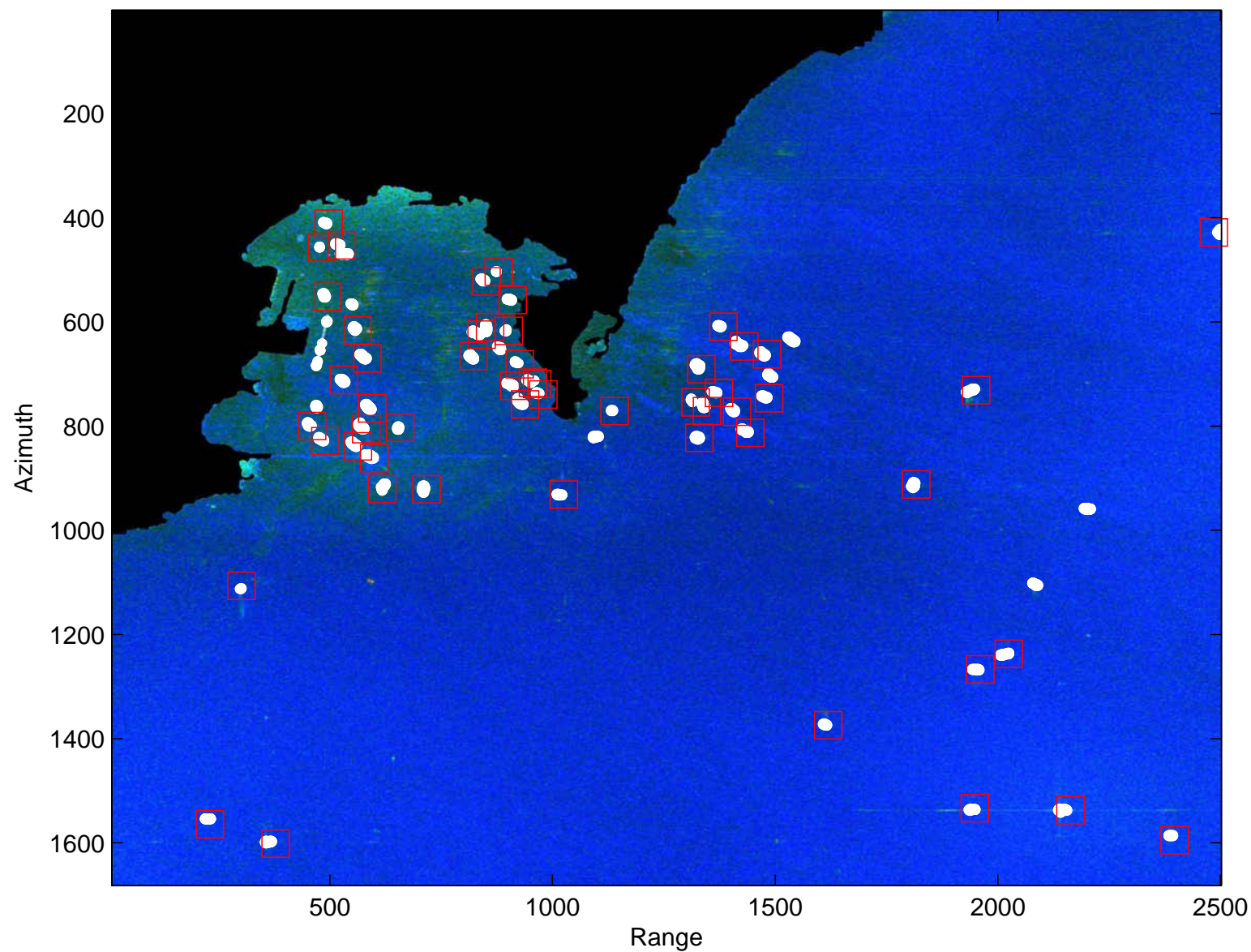
Figure 5.10: *Medium Resolution RCM mode* : Final detections of Scene 6 detected by the hybrid detection algorithm superimposed on the RGB images of the $m - \chi$ decomposition. Red squares represent the verified position of the ships and white dots represent the final detections.
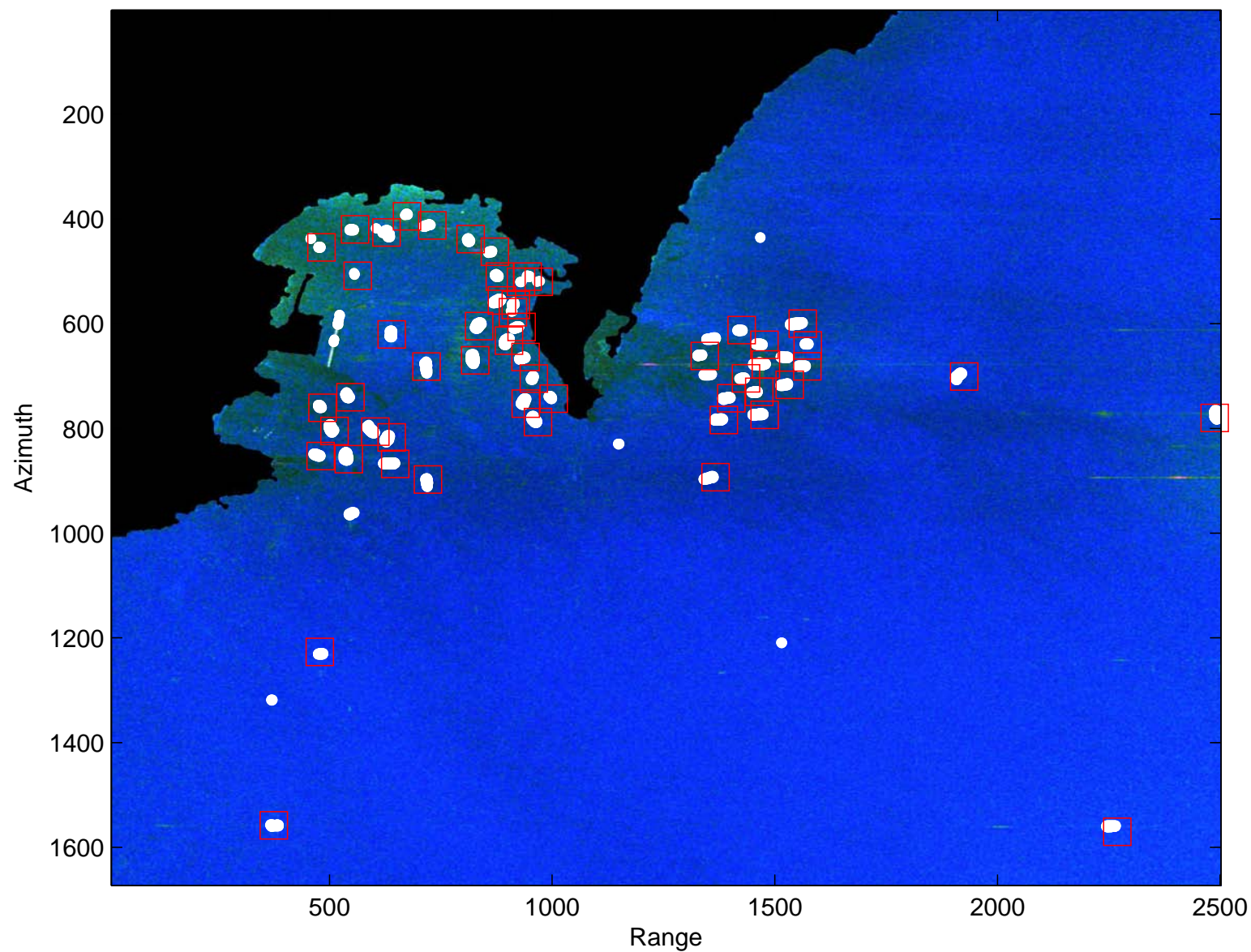
5.3 The Low Resolution RCM Mode Results

5.3.1 Setup of Detection Algorithm Parameters

First step Pre-screening stage

For the Low Resolution mode, the global threshold is determined using an ocean block of 400 pixels in range $\times$ 200 pixels in azimuth analogous to that of the Medium Resolution mode. The ocean block dimension in the azimuth direction, is reduced to half of that of the Medium Resolution mode in order to achieve a fair comparison between the detection results of these two imaging modes. This is done because the simulated Low Resolution data has double the azimuth sample spacing of the Medium Resolution mode while has the same range spacing. After that, the maximum S_0 value of the ocean pixels is taken to be the global threshold.

Target and Background Windows Setup

As in the Medium Resolution mode, the regular target window for the Low Resolution data has an offset from the maximum and minimum range and azimuth target boundary pixels of 1 pixel (C1 = 1). However, the background window offsets from the target window, C2 and C3, are equal and are set to 10 pixels. These values are selected to achieve both accurate ocean data pdf estimation for the smallest candidate target of one pixel and to facilitate fast run of the pre-screener algorithms. For near-land candidates, C1 remains the same as for far-from-land targets while C2 and C3 is enlarged to 30 pixels to ensure adequate non-zero data points for accurate ocean data pdf estimation.

5.3.2 Detection Results

Table 5.2 shows the number of detections after each stage of the developed algorithm for the six Low resolution RCM scenes. The number of detections after pre-screening is much larger than that after the discrimination stage by 1.4 to 2.5 times. It is also clear that there is a number of missed detections for this mode. The number of missed ships with verified

130

positions ranges from 1 to 2 ships in 2 of the scenes (Scene 2 and 3) which reduces the VDR percentage to 81.82% at the worst case (Scene 3). Table 5.3 shows the length, width, type and orientation relative to the range direction information related to these ships. In Scene 3, the upper ship is number 1 and the lower ship is number 2. By investigating the AIS data of these ships, we found that all 3 ships have dimensions that are smaller than the resolution cell of this RCM mode. This means that if the brightness of these ship pixels is not high enough with respect to their neighboring ocean pixels, they will most likely be missed. In fact all three ships were not detected by either pre-screening steps. This can be seen clearly from Figure 5.11 which shows the detection results after applying each stage of the detection algorithm to Scene 3. This scene is selected to manifest the worst missed detections case in this mode. The top left sub-figure shows the candidate targets from the global thresholding pre-screener in green stars with the verified ship positions as red squares superimposed on an RGB image of Scene 3. Detections from second pre-screeners are indicated in yellow crosses in the top right sub-figure and final detections are presented as white dots in the bottom sub-figure. The above observations about the missed ships may be interpreted as that these ships have a low backscattered power (low brightness) most probably due to their small sizes with respect to the resolution cell size. However, other factors like ship shape, orientation, construction and superstructure may affect the backscattered power.

The final detection results of all six scenes in the Low Resolution RCM mode are shown in Figure 5.12 to Figure 5.17 .

Table 5.2: *Low Resolution RCM mode* : Number of detections after applying all stages of the hybrid detection algorithm to all scenes. The table entries represent the number of detections after the first pre-screening step (1st Pre-scr.), the second pre-screening step (2nd Pre-scr.) and the final detections after the discrimination stage. The final detections are sorted to detections with AIS positions (AIS(D)), missed detections with AIS positions (AIS(M)) and extra detections (Ext.). The total number of detections and the verified detection rate (VDR) percentage are also shown for each scene. The last row presents the total number of detections over the six scenes after each detection stage.

Scene No.	1st Pre-scr.	2nd Pre-scr.	Final Detections			Total No. Det.	VDR %
			AIS(D)	AIS(M)	Ext		
1	22	16	9	0	2	11	100%
2	13	11	7	1	0	7	87.50%
3	29	27	9	2	2	11	81.82%
4	31	31	11	0	9	20	100%
5	84	82	54	0	6	60	100%
6	120	120	54	0	10	64	100%
Tot.	299	287	144	3	29	173	97.96%

Table 5.3: AIS information of the three missed ships of Scenes 2 and 3 in the Low Resolution RCM mode. In Scene 3, the upper ship is number 1 and the lower ship is number 2.

Ship No.	Length (m)	Width (m)	Orient. (°)	Type
Scene 2				
1	29	9	90	Tug
Scene 3				
1	81	14	30	Cargo
2	91	78	0	Cargo
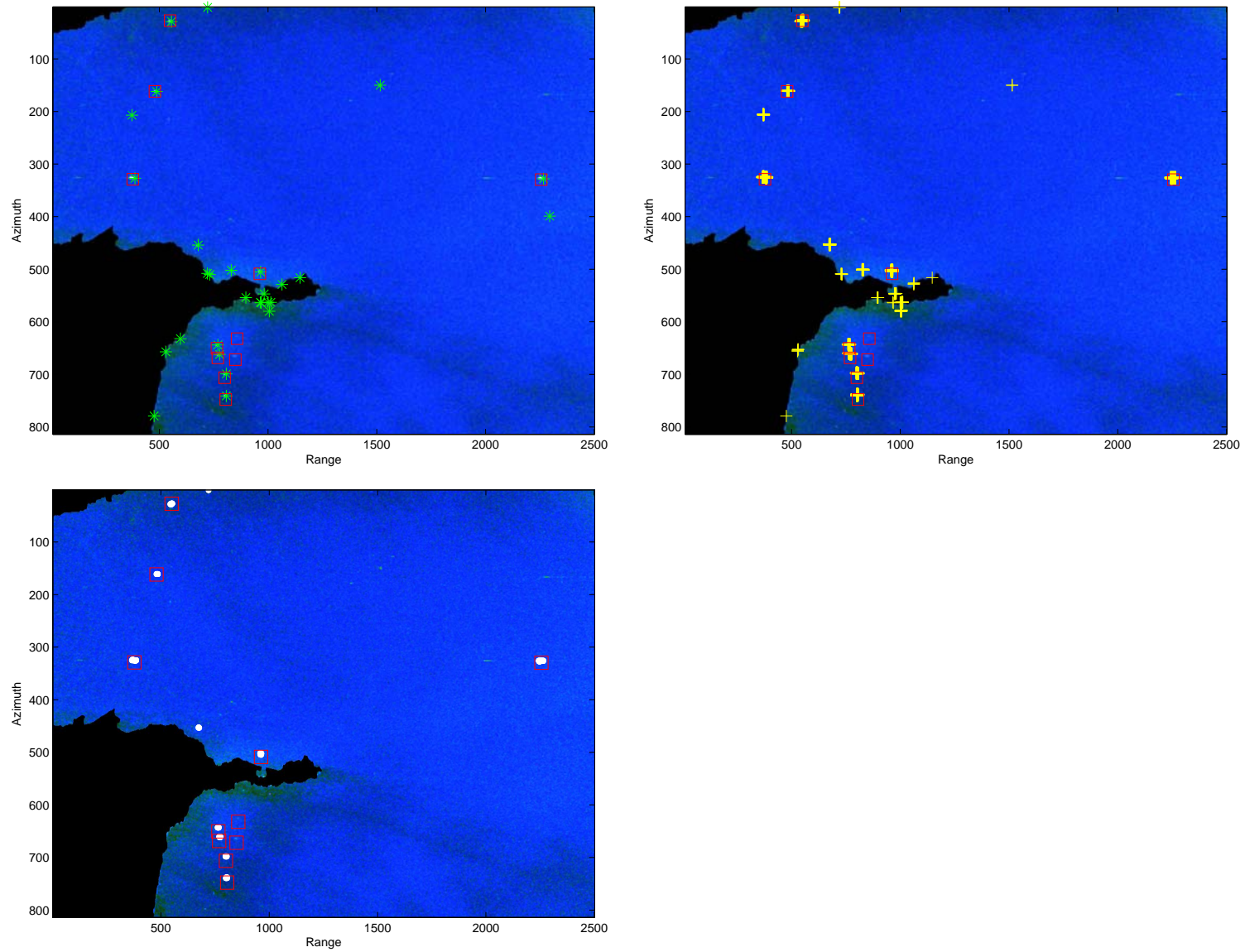
Figure 5.11: *Low Resolution RCM mode* : Detection results applying the hybrid detection algorithm stages to Scene 3. Red squares represent the verified position of the ships, green stars represent the candidate target detected by the global thresholding first pre-screening step, yellow crosses represent the detected clusters after of the ATD pre-screeners and the white dots represent the final detections after the discrimination stage. Top left: results of the first pre-screening step (global thresholding). Top right: results of the second pre-screening step (CFAR and Stokes LRT ATDs). Bottom: final detections after discrimination stage (child parameters analysis). Detections are superimposed on the RGB images of the $m - \chi$ decomposition.

Figure 5.12: *Low Resolution RCM mode* : Final detections of Scene 1 detected by the hybrid detection algorithm superimposed on the RGB images of the $m-\chi$ decomposition. Red squares represent the verified position of the ships and white dots represent the final detections.
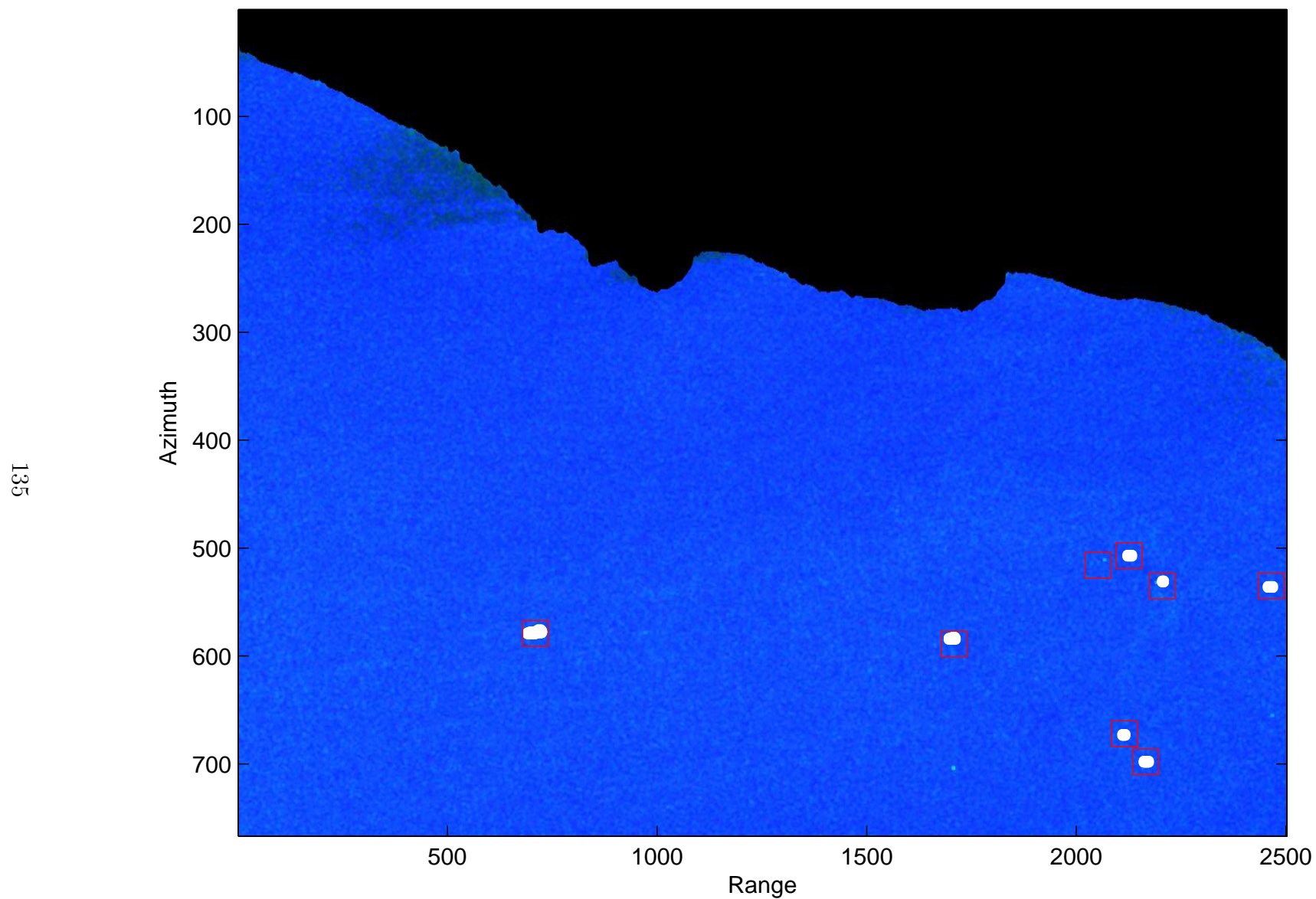
Figure 5.13: *Low Resolution RCM mode* : Final detections of Scene 2 detected by the hybrid detection algorithm superimposed on the RGB images of the $m-\chi$ decomposition. Red squares represent the verified position of the ships and white dots represent the final detections.
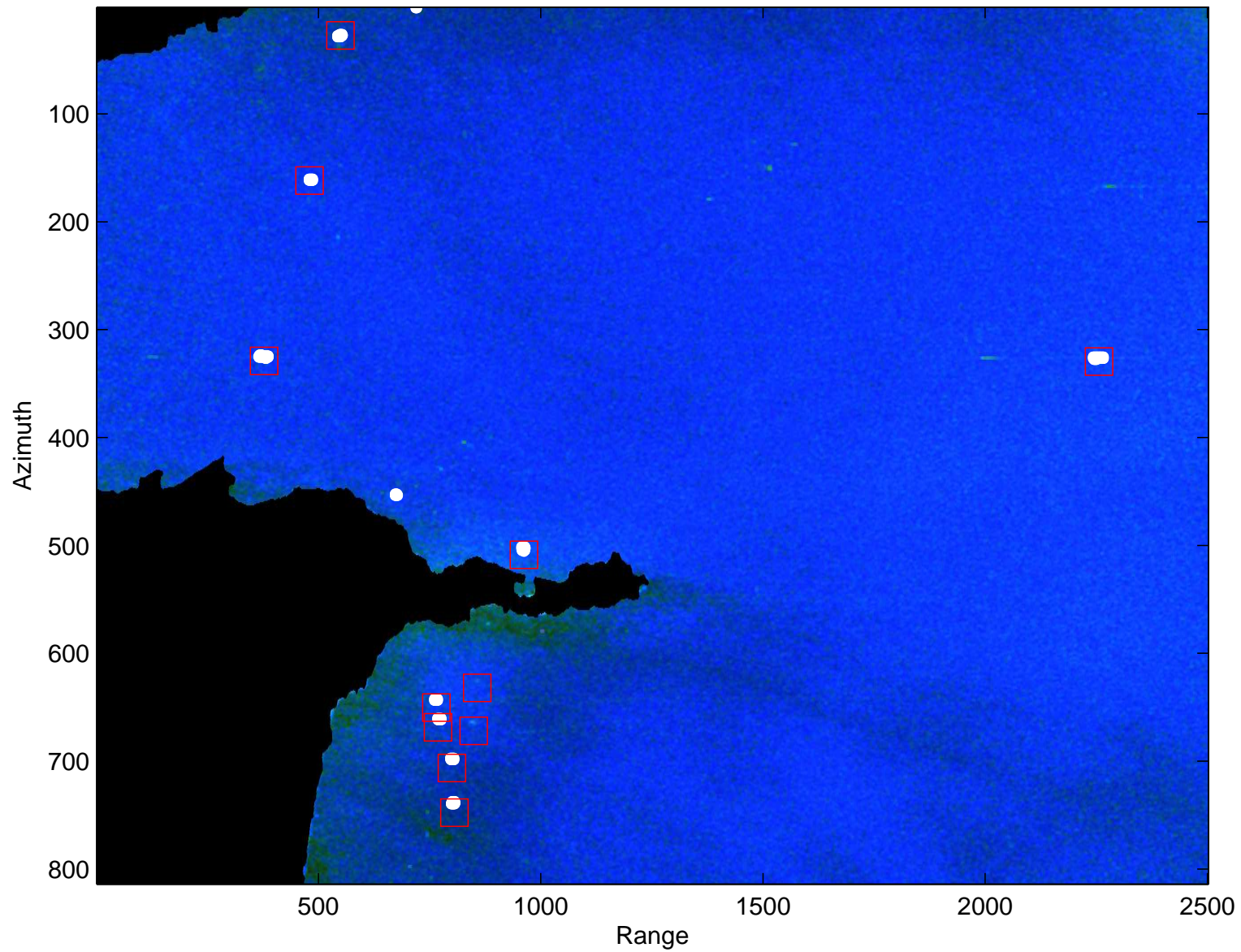
Figure 5.14: *Low Resolution RCM mode* : Final detections of Scene 3 detected by the hybrid detection algorithm superimposed on the RGB images of the $m - \chi$ decomposition. Red squares represent the verified position of the ships and white dots represent the final detections.
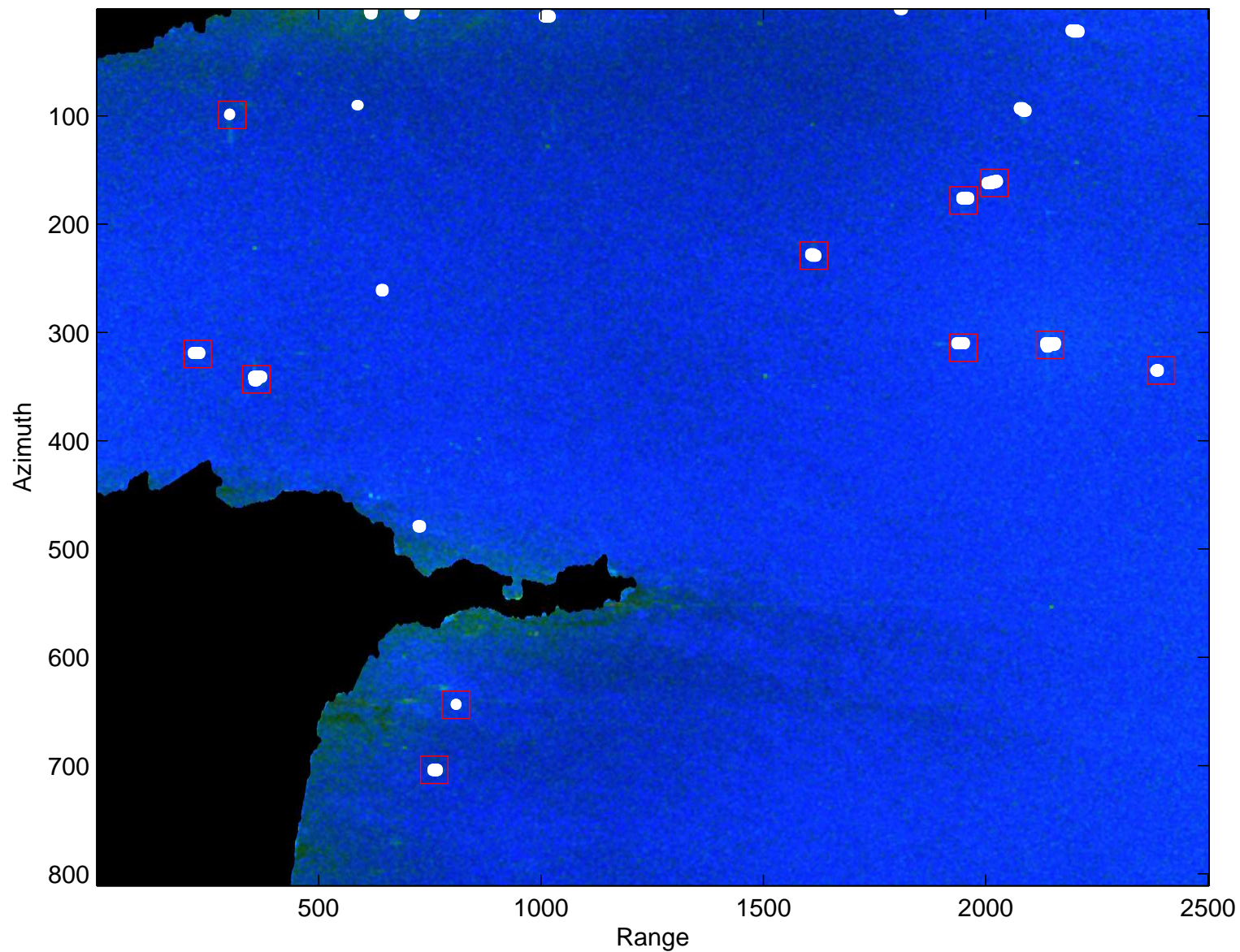
Figure 5.15: *Low Resolution RCM mode* : Final detections of Scene 4 detected by the hybrid detection algorithm superimposed on the RGB images of the $m-\chi$ decomposition. Red squares represent the verified position of the ships and white dots represent the final detections.
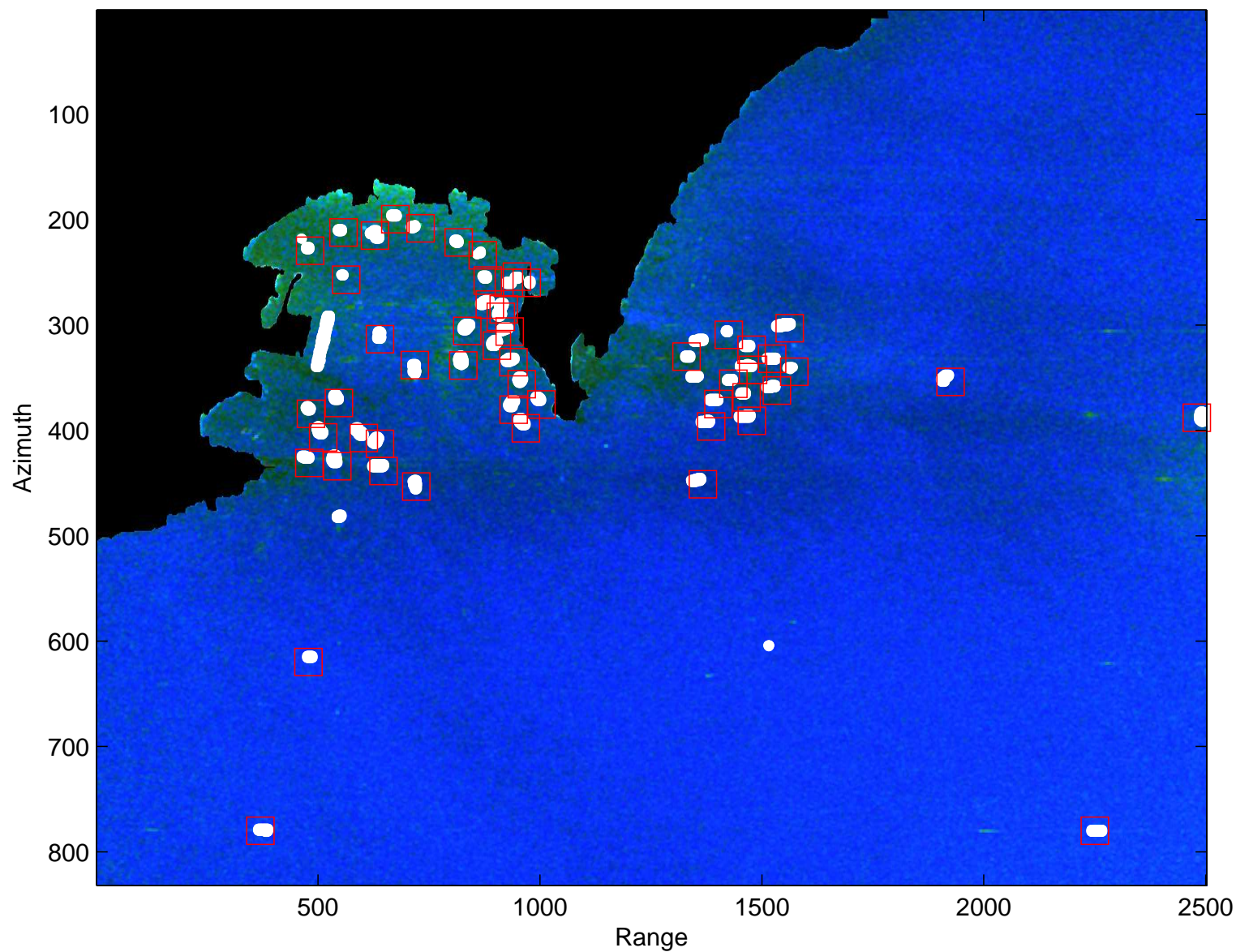
Figure 5.16: *Low Resolution RCM mode* : Final detections of Scene 5 detected by the hybrid detection algorithm superimposed on the RGB images of the $m-\chi$ decomposition. Red squares represent the verified position of the ships and white dots represent the final detections.
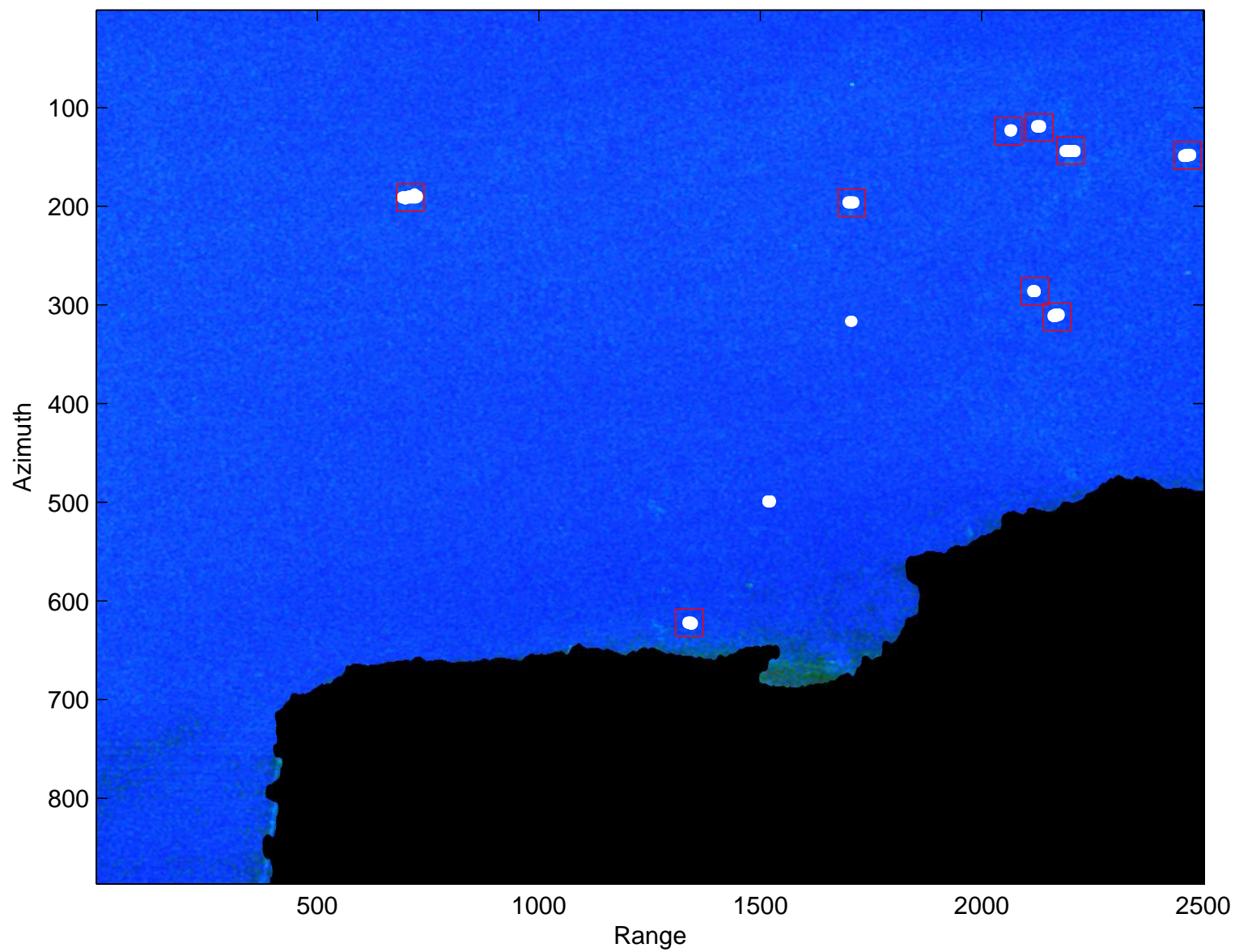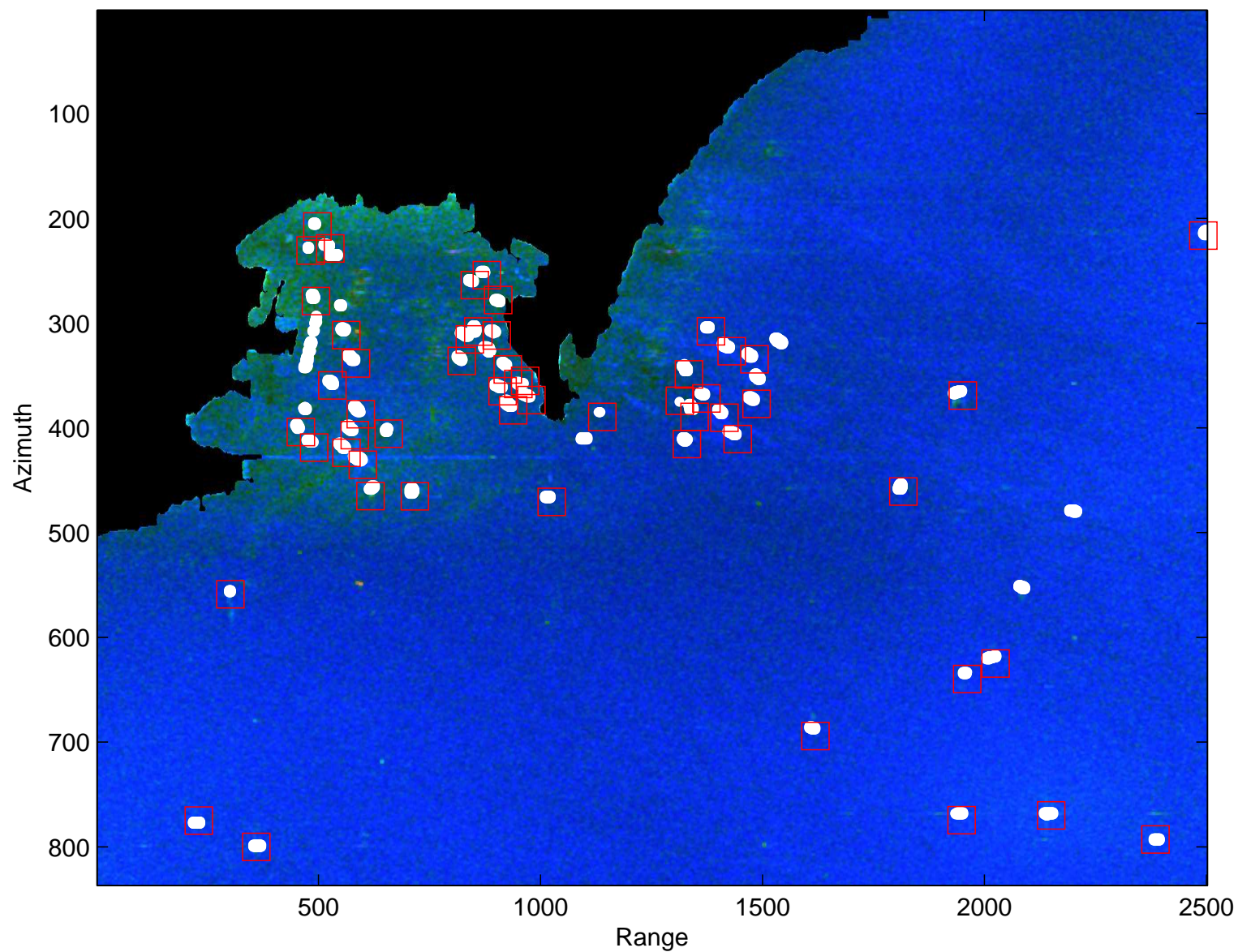
Figure 5.17: *Low Resolution RCM mode* : Final detections of Scene 6 detected by the hybrid detection algorithm superimposed on the RGB images of the $m-\chi$ decomposition. Red squares represent the verified position of the ships and white dots represent the final detections.

5.4　The Ship Detection RCM Mode Results

5.4.1　Setup of Detection Algorithm Parameters

First step Pre-screening stage

In this mode, the global threshold is determined using an ocean block of 1600 pixels in range × 400 pixels in azimuth, analogous to that of the Medium Resolution mode. The ocean block dimension in the range direction is increased by 4 times over that of the Medium Resolution mode in order to achieve a fair comparison between the detection results of these two imaging modes. This is done because the range pixel spacing simulated of the Ship Detection data has nearly one quarter that of the Medium Resolution mode, but has the same azimuth pixel spacing. After that, the maximum S_0 value of the ocean pixels is taken to be the global threshold.

Target and Background Windows Setup

As in the other two modes, the regular target window for the Ship Detection data has an offset from the maximum and minimum range and azimuth target boundary pixels of 1 pixel (C1 = 1). However, the background window offsets from the target window, C2 and C3, are set to be unequal to get the benefit from the large number of pixels in the range direction of this mode images. The offset in the azimuth direction C2 is set to 10 while the offset in the range direction C3 is set to 40.

For near-land candidates, C1 remains the same as for far-from-land targets while C2 enlarged to 30 pixels and C3 is set to 60 pixels to ensure adequate non-zero data points for accurate ocean data pdf estimation.

5.4.2　Detection Results

For the Ship detection mode, Table 5.4 shows the number of detections after each stage of the developed algorithm for all scenes. It is clear from Table 5.4 that all ships with verified positions are successfully detected in all scenes. One also can see that some extra

targets are found in all scenes. It is noticed that the number of candidate targets after the first pre-screening step is larger than that of the second step for all scenes as in the other two modes. The latter is more than the final detections by 1.6 to 4.4 times. Figure 5.18 shows the detection results of each stage of the algorithm of Scene 6. In Figure 5.18, red squares represent the verified position of ships, green stars represent candidate targets detected by the global thresholding first pre-screening step, yellow crosses represent detected targets after of the ATD pre-screeners and the white dots represent the final detections after the discrimination stage. Note from this figure that the number of candidate targets after both pre-screening steps is similar and larger than the final detections. However, after the discrimination stage nearly 54% of these detections is rejected.

Table 5.4: *Ship Detection RCM mode*: Number of detections after applying all stages of the hybrid detection algorithm to all scenes. Table entries represent the number of detections after the first pre-screening step (1st Pre-scr.), the second pre-screening step (2nd Pre-scr.) and the final detections after the discrimination stage. The final detections are sorted to detections with AIS positions (AIS(D)), missed detections with AIS positions (AIS(M)) and extra detections (Ext.). The total number of detections and the verified detection rate (VDR) percentage are also shown for each scene. The last row presents the total number of detections over the six scenes after each detection stage.

Scene No.	1st Pre-scr.	2nd Pre-scr.	AIS(D)	Final Detections AIS(M)	Ext	Total No. Det.	VDR %
1	21	18	9	0	2	11	100%
2	23	17	8	0	1	9	100%
3	35	33	11	0	3	14	100%
4	79	75	11	0	6	17	100%
5	120	102	54	0	8	62	100%
6	143	140	54	0	10	64	100%
Tot.	421	385	147	0	30	177	100%
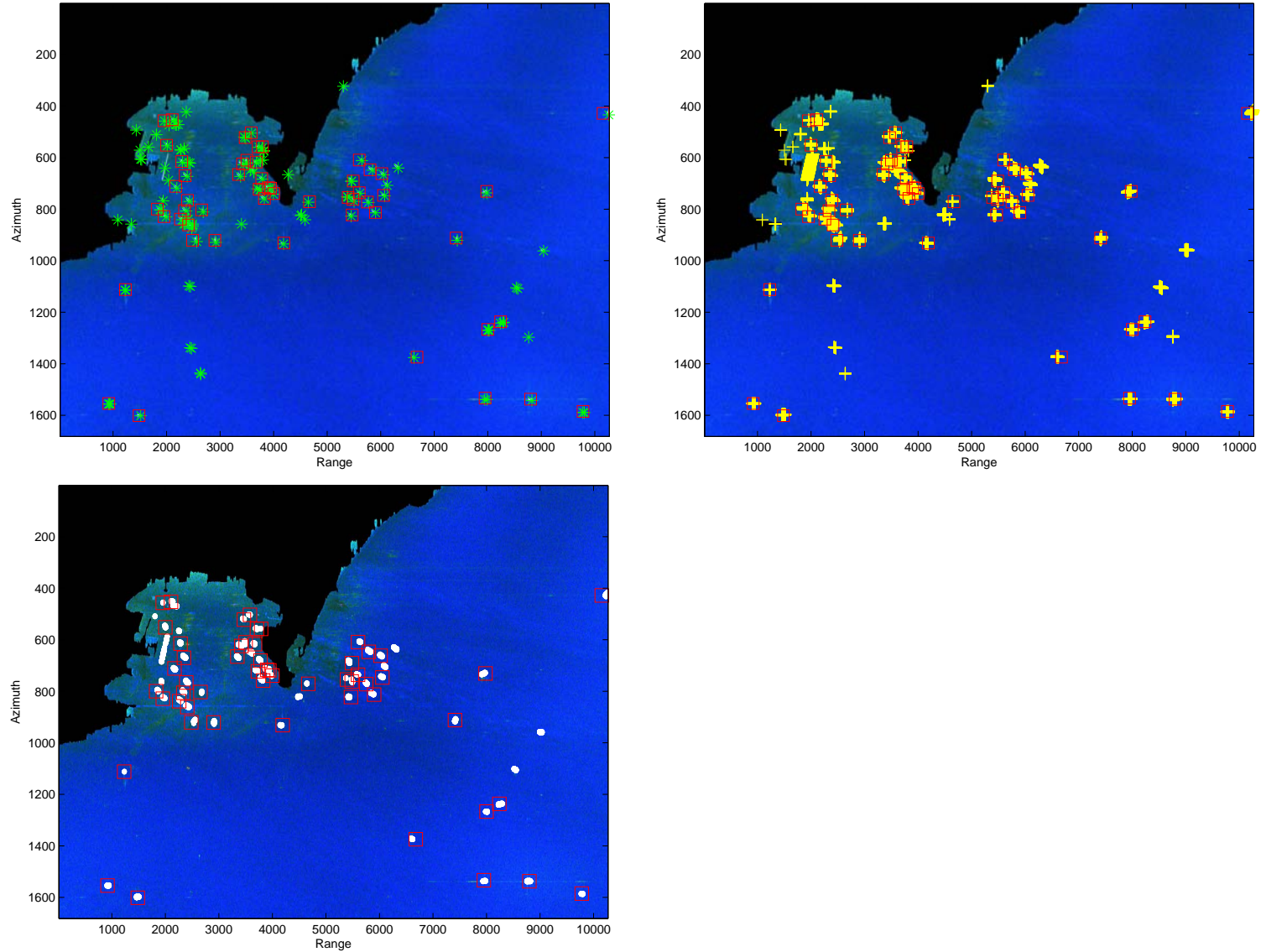
Figure 5.18: *Ship Detection RCM mode* : Detection results applying the hybrid detection algorithm stages to Scene 6. Red squares represent the verified position of the ships, green stars represent the candidate target detected by the global thresholding first pre-screening step, yellow crosses represent the detected targets after the ATD pre-screeners and the white dots represent the final detections after the discrimination stage. Top left: results of the first pre-screening step (global thresholding). Top right: results of the second pre-screening step (CFAR and Stokes LRT ATDs). Bottom: final detections after discrimination stage (child parameters analysis). Detections are superimposed on the RGB images of the $m - \chi$ decomposition.
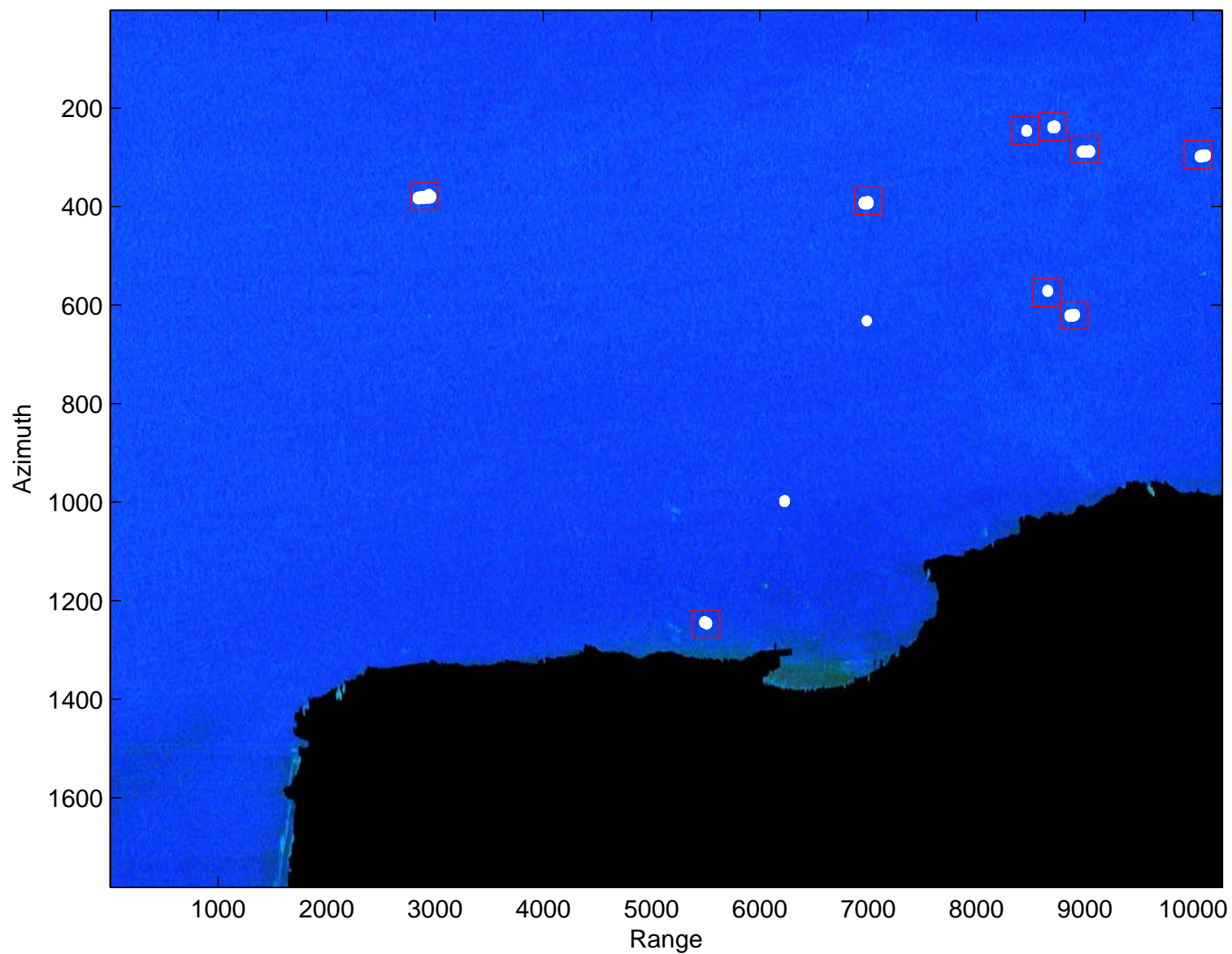
Figure 5.19: *Ship Detection RCM mode* : Final detections of Scene 1 detected by the hybrid detection algorithm superimposed on the RGB images of the $m-\chi$ decomposition. Red squares represent the verified position of the ships and white dots represent the final detections.
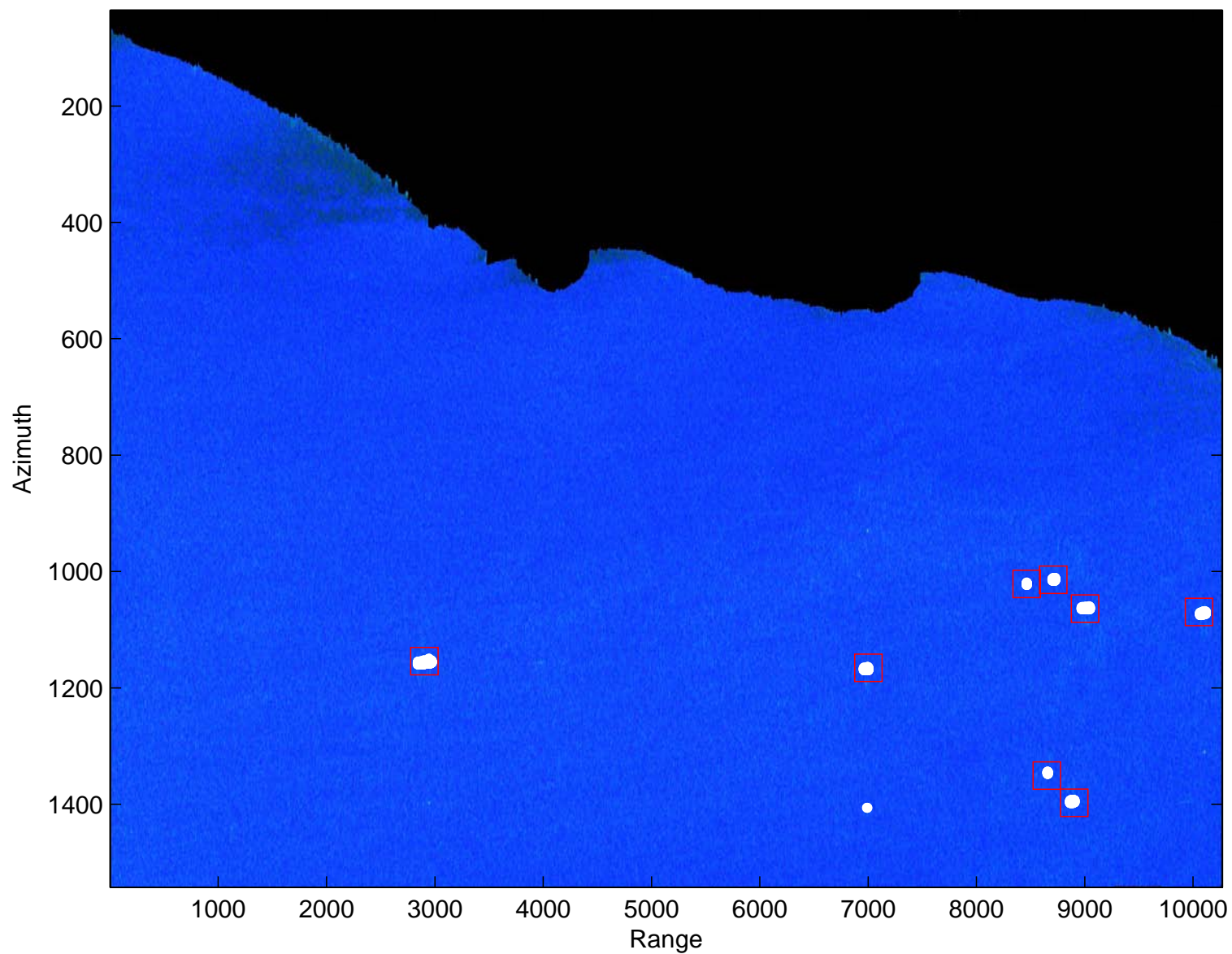
Figure 5.20: *Ship Detection RCM mode* : Final detections of Scene 2 detected by the hybrid detection algorithm superimposed on the RGB images of the $m-\chi$ decomposition. Red squares represent the verified position of the ships and white dots represent the final detections.
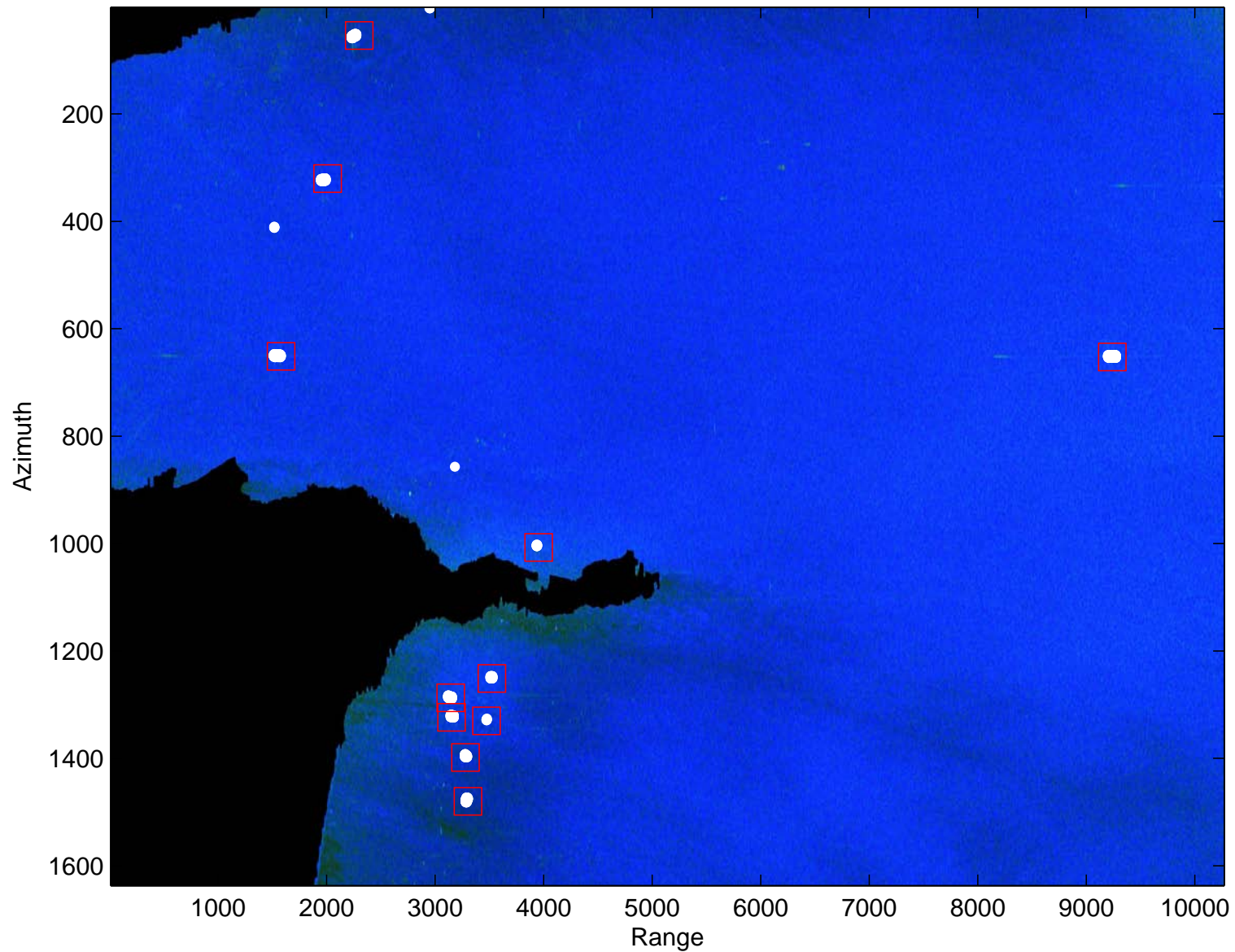
Figure 5.21: *Ship Detection RCM mode* : Final detections of Scene 3 detected by the hybrid detection algorithm superimposed on the RGB images of the $m-\chi$ decomposition. Red squares represent the verified position of the ships and white dots represent the final detections.
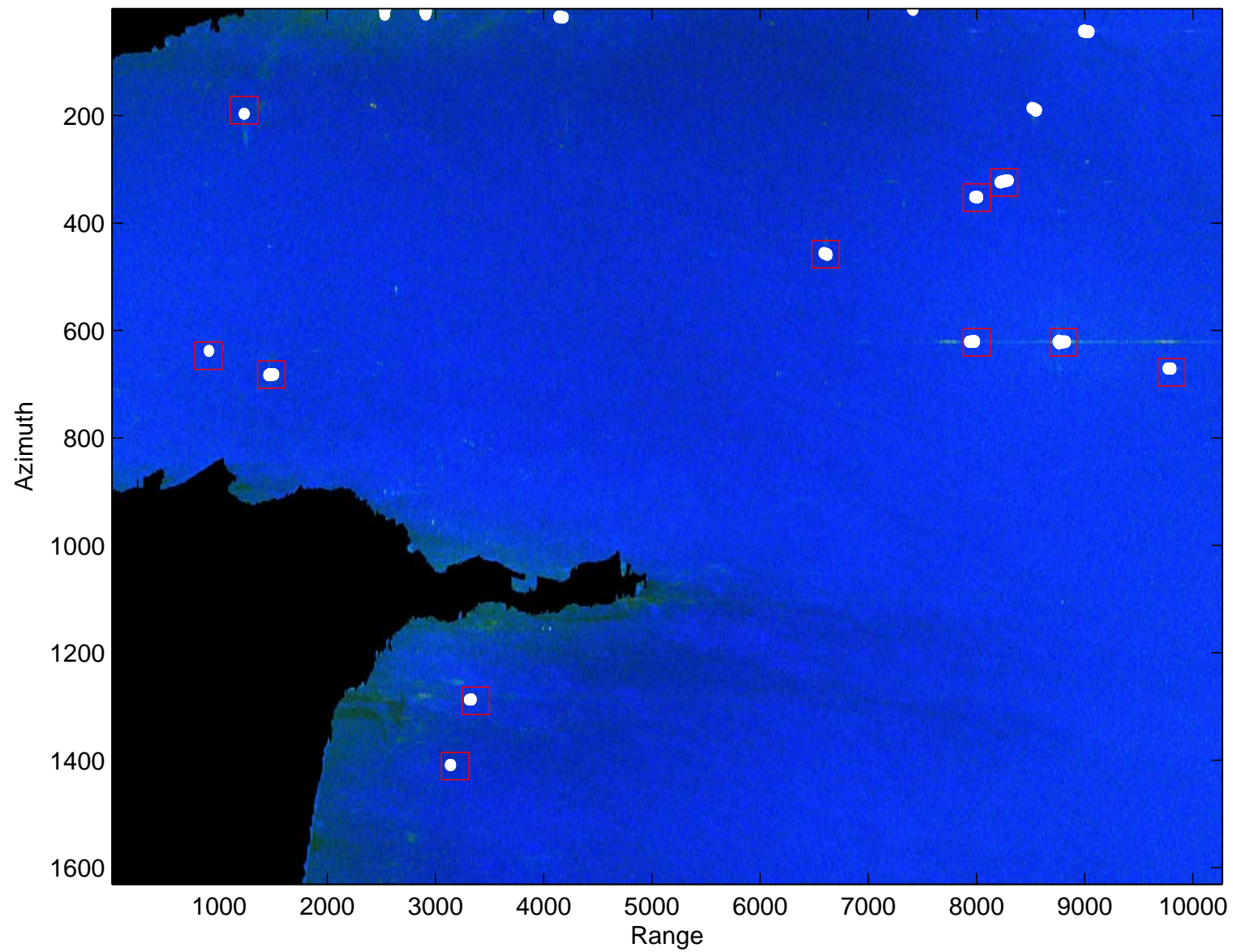
Figure 5.22: *Ship Detection RCM mode* : Final detections of Scene 4 detected by the hybrid detection algorithm superimposed on the RGB images of the $m-\chi$ decomposition. Red squares represent the verified position of the ships and white dots represent the final detections.
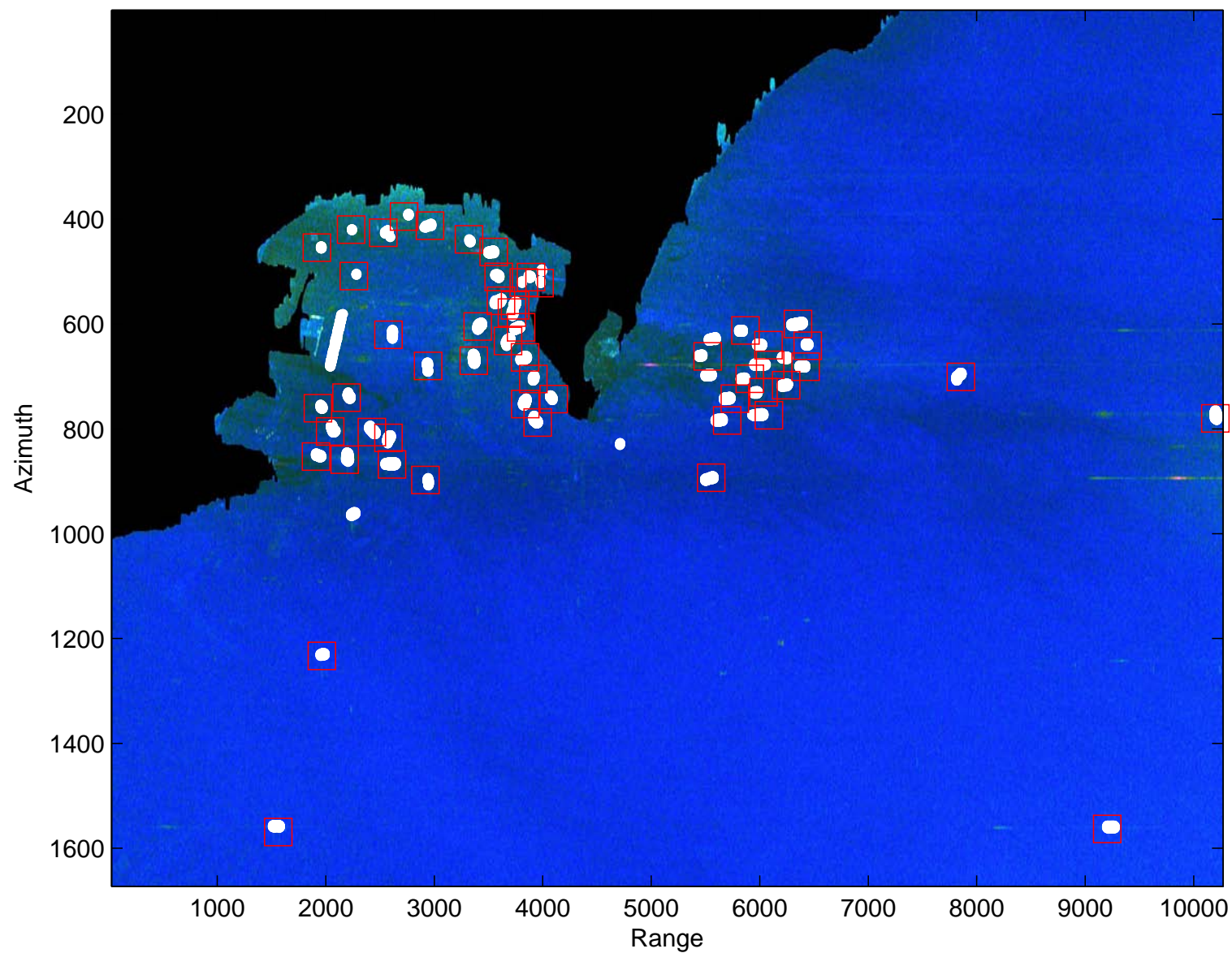
Figure 5.23: *Ship Detection RCM mode* : Final detections of Scene 5 detected by the hybrid detection algorithm superimposed on the RGB images of the $m - \chi$ decomposition. Red squares represent the verified position of the ships and white dots represent the final detections.
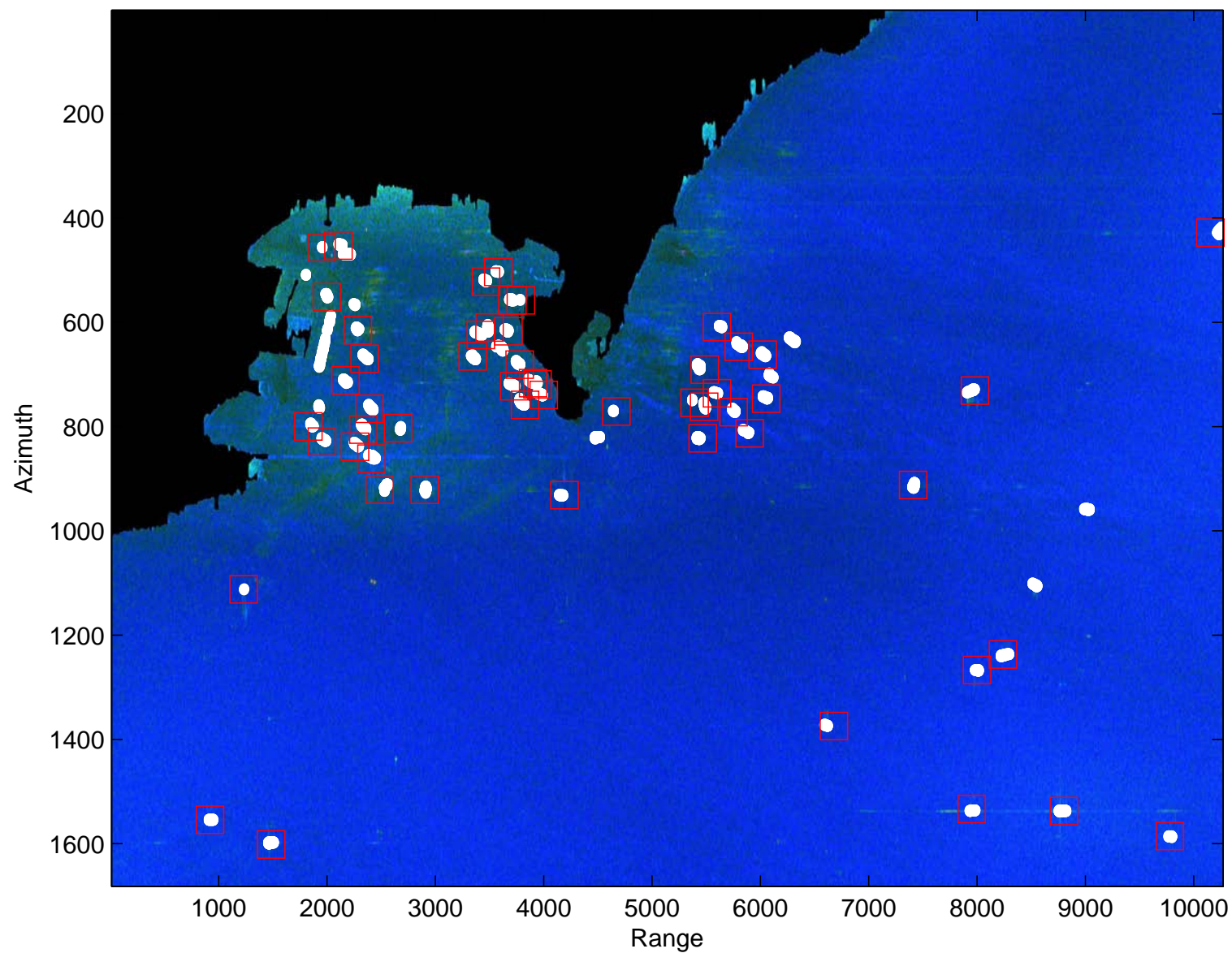
Figure 5.24: *Ship Detection RCM mode* : Final detections of Scene 6 detected by the hybrid detection algorithm superimposed on the RGB images of the $m - \chi$ decomposition. Red squares represent the verified position of the ships and white dots represent the final detections.

5.4.3 Comparison of RCM Modes Detection Results

To summarize the detection results of the three RCM modes, we include the total number of detections over all six scenes in each mode in Table 5.5. The columns of the table is divided into 4 sets separated by a vertical line. The first set contains the three RCM modes. The second set shows the total number of detections after the first and second pre-screening steps. The third set shows the total number of final detections after the discrimination stage; this set is composed of three columns: the total number of detected ship with verified positions, the total number of missed ships with AIS positions and total number of extra targets. The fourth set is for the total number of all detections, with and without verified positions, and the last set is for the total VDR percentage.

It is clear from the table that the largest number of pre-screening detections is for the Ship Detection mode followed by the Medium Resolution mode and then the Low Resolution one. This may be attributed to the fact that Ship Detection data has the highest resolution followed by the Medium Resolution mode and then the Low Resolution mode. Moreover, the Ship Detection data is used as the simulated SLC images without multilooking unlike the other two RCM modes data. Obviously, multilooking reduces speckle that may be detected as candidate targets by the pre-screener. The Low Resolution mode has the largest number of looks (8 looks in the range direction) and hence the best smoothing effect along with the low resolution and therefore, the lowest number of pre-screening detections. In the middle, comes the Medium Resolution mode with the 4 looks in the range direction and the medium number of pre-screening detections.

From the total number of final detections, we notice that the developed detection algorithm has successfully detected all ships with verified positions in the Ship detection and the Medium Resolution modes. On the other hand, three ships were missed at the Low Resolution mode. This may be attributed to their low backscattered power due to their small sizes with respect to the resolution cell (and other factors) and the low resolution of

this mode. Thus, the total percent Verified Detection Rate is reduced to nearly 98% for this low resolution mode.

Table 5.5: Total detection results of the Medium Resolution, Low Resolution and the Ship Detection RCM modes after each stage of the hybrid ship detection algorithm. The table entries represent the total number of detections after the first pre-screening step (1st Pre-scr.), the second pre-screening step (2nd Pre-scr.) and the final detections after the discrimination stage. The final detections are sorted to detections with AIS positions (AIS(D)), missed detections with AIS positions (AIS(M)) and extra detections (Ext.). The total number of detections and the total verified detection ratio (VDR) are presented as well for each mode. The total number of detections after each stage are taken over the six scenes at each mode.

RCM Mode	1st Pre-scr.	2nd Pre-scr.	Final Detections			Total No. Det.	VDR %
			AIS(D)	AIS(M)	Ext		
Medium Resolution	339	305	147	0	32	179	100%
Low Resolution	299	287	144	3	29	173	97.96%
Ship Detection	421	385	147	0	30	177	100%

It is obvious from Table 5.5 that the total number of extra detections in all three modes is close, and that the least number is for the Low Resolution mode. Finally, we can see that the total number of all detected ships for the Ship Detection and for the Medium Resolution modes are close, and that the Ship detection mode has the largest number, while the lowest number is for the Low Resolution mode which is to be expected.

5.4.4 Advantages of the Hybrid Ship Detection Algorithm

To sum up, the results manifest the following advantages of the developed algorithm:

1. The pre-screener's first step declares a large number of candidate targets. This is useful to avoid missing potential targets.

2. The composite structure of the pre-screener's second step (the CFAR and the LRT) benefits from each of the detector merits and discards its demerits. The sub-optimal CFAR detector is used when it is not possible to estimate target's pdf while the optimal LRT detector is employed adaptively for large candidates.

3. The application of the second pre-screening step only to candidate detections from

the first step reduces the computational burden and the run time needed to obtain final detections compared to algorithms that apply adaptive thresholding to the entire scene. This makes the algorithm suitable to offer near real time service.

4. The adaptive nature of the pre-screener's second step enables taking into consideration local sea state around candidates only in order to refine the detections without increasing the computational burden.

5. Taking local sea condition requires estimating accurate pdf of ocean data which is fulfilled by using the GMM method. The GMM method enables the estimation of the joint pdfs of ocean and ships Stokes parameters required by the LRT detector.

6. The $m - \chi$ decomposition analysis of the discrimination stage reduces false alarms from ocean and ship ghosts significantly and enhances the detection performance.

7. The special setup of the pre-screener and discriminator used for candidate targets near land reduces potential false alarms in these regions.

8. The detection algorithm can be used effectively to detect ships in low and medium resolution CP images.

5.5   Conclusion

In this chapter, the detection results of applying the proposed hybrid ship detection algorithm were presented. The algorithm was applied to a number of RS-2 scenes simulated in the Medium Resolution, Low Resolution and the Ship Detection RCM modes. The detection algorithm is composed of two stages: two-step pre-screening stage and a discrimination stage. In the pre-screening stage, a global thresholding of each pixel in the total received power (S_0) image is performed to declare preliminary candidate targets. This step is followed by an adaptive thresholding detection applied only for these preliminary candidates to take local sea state condition into consideration. The adaptive thresholding detectors used in this step are the S_0-CFAR and the Stokes Parameters LRT detectors. The selection between either

detectors is made based on the size of the candidate target. Small targets are tested by the CFAR detector while large targets are tested by the LRT one. Re-detected targets are then passed to the discrimination stage for (m-χ) decomposition analysis. In the discrimination stage, a final detection decision is made based on the type and strength of the scattering mechanisms of the detected targets and not on the target size.

Results show that the pre-screening stage, the first step in particular, declares a large number of candidate targets. Although some of these detections may be false alarms, this large number of preliminary detections is counted as an advantage to avoid missing potential targets. The composite structure of the pre-screener makes benefits from many detection strategies (global thresholding, sub-optimal detector like the CFAR and optimal detector as the LRT one). Moreover, this structure reduces the computational burden and the run time to obtain final detections compared to algorithms that apply adaptive thresholding to the entire scene. On the other hand, final detections, after the discrimination stage, are much less as the child parameters analysis of the discrimination algorithm enhances the detection performance by reducing false alarms.

The developed hybrid ship detection algorithm was able to detect most verified ships in addition to extra maritime objects in all scenes and RCM modes. In the Medium Resolution and the Ship Detection modes, the algorithm detected successfully all ships with verified positions. However, nearly 98% of the verified ships were detected in the Low Resolution mode. The missed ships have low backscatter power that do not enable the algorithm to detect them in the first detection stage. The detection results of the three RCM modes are comparable with the Medium Resolution and the Ship detection modes share the best detection performance followed by the Low Resolution mode. Therefore, it is apparent that all three RCM modes would benefit the ship detection application by providing high detection performance and large swath width.

Chapter 6

Conclusions and Future Study Recommendations

6.1 Conclusions

Ship detection is one of the important components of maritime surveillance. SAR systems provide tremendous amount of information about earth in the form of multi-polarization and multi-resolution images of areas allover our planet. Of particular importance and interest is the compact polarimetric SAR data which achieves a trade-off between multi-polarization system advantages and the wide coverage required for surveillance applications. In this thesis, the benefits of using hybrid CP data for ship detection in SAR images with various resolutions, acquired with different incidence angle beams and polarizations were explored. For this purpose, two novel contributions were introduced in this research; the first is the investigation of the possibility and benefits of using the pseudo-quad data generated from CP data for improved ship detection. The PQ data was generated by a reconstruction algorithm that was developed specifically for maritime applications. This is done by comparing the ship detection performance of PQ data to linear, circular and CP dual-pol SAR data. This study is performed on FQ RS-2 data and simulated RCM data in the Medium, Low Resolution and the Ship Detection modes. This CP ship detection investigation study for simulated Radarsat Constellation Mission data is the first in the literature. The other contribution is the development of a Stokes parameters hybrid ship detection algorithm to be used to detect vessels in CP data with medium and low resolutions.

6.1.1 Ship Detection Performance Analysis of Compact Polarimetric Data Conclusions

In this part of the thesis, the possibility and benefits of using compact polarimetry SAR generally and the pseudo-quad data specifically for ship detection are investigated. The pseudo-

quad data was generated using Collins reconstruction algorithm which was developed in a collaboration with a research team at the U of C specifically for maritime applications. This reconstruction algorithm has the highest reconstruction performance of C-band ocean data among other algorithms. The reconstruction algorithm uses the four elements of the CTLR CP covariance matrix to generate the amplitude of the two co-pol components ($|S_{HH}|, |S_{VV}|$), their relative phase and the cross-pol amplitude ($|S_{HV}|$). In order to do that, reflection symmetry was assumed for the ocean data. Another assumption that was incorporated is the polarization state interpolation originally developed by Souyris et. al [22] and then modified by Nord et. al [57]. The constant of proportionality required for this assumption was estimated using Collins experimentally-based model which takes the incidence angle of the imaging mode into consideration to improve the reconstruction performance of ocean data. This reconstruction algorithm was applied to a number of RS2 scenes with fine (FQ data), medium and low resolutions (simulated RCM data) and acquired by different beam modes. The ship detection performance of the reconstructed quad-pol (PQ) data was compared to that of a number of SAR detectors (quad-pol, linear, circular and compact dual-pol) data. The ship detection performance was investigated for a LRT ship detector taking into consideration the impact of resolution, ship orientation and beam incidence angle. The detection performance was assessed in terms of the median probability of missed detection (PMD) for each system calculated over a number of ships spread over the available scenes as a function of the probability of false alarm (PFA) and at specific PFA value. From this analysis, the following can be concluded:

1. The detection performance increases with spatial resolution: FQ data has the strongest performance over all RCM modes data while for RCM data, the Low Resolution data had the weakest performance and the Ship Detection mode had the strongest performance.

2. For incidence angles greater than 25°, compact polarimetry modes had superior ship detection performance to linear polarization data while at steeper incidence angles, linear

and compact polarization configurations had comparable performance.

3. For all polarizations and imaging modes, ship detection performance increased with incidence angle, with the highest performance at about 40°.

4. For all imaging modes, the PQHV and RH-RV, by themselves and in combination, had the highest performance over other CP, circular and linear-pol data. This suggests the usefulness of quad-pol reconstruction for improved ship detection.

5. Higher performance was observed for ships perpendicular and parallel to radar bore sight.

Thus, the results of this study suggest that quad-pol reconstruction, using Collins reconstruction algorithm, benefits ship detection by enhancing the detection performance. Moreover, the three RCM modes generally, and the Ship Detection mode in particular, are shown to be a promising compromise between the ship detection performance and the wide swath width desired for ship surveillance. Therefore, it may be recommended to use hybrid compact polarimetric SAR data (raw and reconstructed), acquired by RCM imaging modes that cover medium to high (shallow) incidence angles for improved ship detection.

6.1.2 The Hybrid Ship Detection Algorithm Conclusions

The hybrid ship detection algorithm utilizes the CP Stokes parameters and some of their child parameters for ship detection. The proposed algorithm combines four detection techniques together to improve the detection performance and discrimination between ships and false alarms. The algorithm is composed of two stages: a two-step pre-screening stage and a discrimination stage. The first step of the pre-screener exploits the difference in the received power between ocean and ship pixels to globally threshold the entire image to declare preliminary candidate targets. In the second pre-screening step, either one of two new Adaptive Thresholding Detectors (S_0-CFAR and Stokes LRT) are selected to test each preliminary candidate. These adaptive thresholding detectors take local sea state condition into consideration when determining its threshold value. The selection between either detector is

made based on the size of the candidate target. Small targets are tested by the CFAR detector while large targets are tested by the LRT one. This composite structure of the pre-screener benefits from each detector merits and discards its demerits. Moreover, it reduces the computational burden and the run time to obtain final detections. The probability density functions of ocean and ships data Stokes parameters required by the ATDs are estimated using the Gaussian Mixture Model method for each candidate target. Re-detected targets are then passed to the discrimination stage for (m-χ) decomposition analysis. In the discrimination stage, final detection decision is made based on the type and strength of the scattering mechanisms of the detected targets and not on target size. This discrimination rule reduces significantly false alarms. Furthermore, a special setup of the pre-screener and discriminator is used for candidate targets near land to reduce potential false alarms in these regions. This algorithm is applied to a number of RS-2 scenes simulated in the Medium Resolution, Low Resolution and the Ship Detection RCM modes. The detection performance of the developed algorithm is assessed using verification data. Obtained results can help conclude that:

1. In the Medium Resolution and the Ship Detection modes, the algorithm detected successfully all ships with verified positions. However, nearly 98% of the verified ships were detected in the Low Resolution mode. In addition, extra maritime objects in all scenes and RCM modes were detected.

2. All missed ships have low backscatter power that do not enable the algorithm to detect them in the pre-screening stage.

3. The detection results of the three RCM modes are comparable with the Medium Resolution and the Ship Detection modes shares the best detection performance followed by the Low Resolution mode.

Accordingly, it has been found that the proposed hybrid detection algorithm can be used effectively to detect ships in CP SAR images with medium and low resolution.

156

6.2   Recommended Future Studies

In the future work, it is recommended to follow up the performed research with the following:

1. Develop an adaptive reconstruction algorithm to account for sea state and ship data.

2. Investigate the effect of using other Stokes parameters in the pre-screening stage of the hybrid detection algorithm on the detection performance.

3. Use other child parameters and decomposition techniques in the discrimination stage of the algorithm and investigate the improvement in the detection performance.

4. Estimate of some ship-related measurements like length, width and speed.

Appendix A

Copyright Permission for the paper : G. E. Atteia and M. J. Collins, "Ship detection Performance assessment for simulated RCM SAR data," in *Proc. of the IEEE International Geoscience and Remote Sensing Symposium (IGARSS)*, July 2014.

IEEE COPYRIGHT AND CONSENT FORM

To ensure uniformity of treatment among all contributors, other forms may not be substituted for this form, nor may any wording of the form be changed. This form is intended for original material submitted to the IEEE and must accompany any such material in order to be published by the IEEE.Please read the form carefully and keep a copy for your files.

TITLE OF PAPER/ARTICLE/REPORT, INCLUDING ALL CONTENT IN ANY FORM, FORMAT, OR MEDIA (hereinafter, "The Work"):**Ship Detection Performance Assessment for Simulated RCM SAR Data**

COMPLETE LIST OF AUTHORS:**Ghada Atteia, Michael Collins**

IEEE PUBLICATION TITLE (Journal, Magazine, Conference, Book):**2014 IEEE International Geoscience and Remote Sensing Symposium**

COPYRIGHT TRANSFER

1. The undersigned hereby assigns to The Institute of Electrical and Electronics Engineers,Incorporated (the "IEEE") all rights under copyright that may exist in and to: (a) the above Work,including any revised or expanded derivative works submitted to the IEEE by the undersigned based on the Work; and (b) any associated written or multimedia components or other enhancements accompanying the Work.

CONSENT AND RELEASE

2. ln the event the undersigned makes a presentation based upon the Work at a conference hosted or sponsored in whole or in part by the IEEE, the undersigned, in consideration for his/her participation in the conference, hereby grants the IEEE the unlimited, worldwide, irrevocable permission to use, distribute, publish, license, exhibit, record, digitize, broadcast, reproduce and archive, in any format or medium, whether now known or hereafter developed: (a) his,&er presentation and comments at the conference; (b) any written materials or multimedia files used in connection with his/her presentation; and (c) any recorded interviews of him/her (collectively, the "Presentation"). The permission granted includes the transcription and reproduction ofthe Presentation for inclusion in products sold or distributed by IEEE and live or recorded broadcast ofthe Presentation during or after the conference.

3. In connection with the permission granted in Section 2, the undersigned hereby grants IEEE the unlimited, worldwide, irrevocable right to use his/her name, picture, likeness, voice and biographical information as part of the advertisement, distribution and sale of products incorporating the Work or Presentation, and releases IEEE from any claim based on right of privacy or publicity.

4. The undersigned hereby warrants that the Work and Presentation (collectively, the "Materials") are original and that he/she is the author of the Materials. To the extent the Materials incorporate text passages, figures, data or other material from the works of others, the undersigned has obtained any necessary permissions. Where necessary, the undersigned has obtained all third party permissions and consents to grant the license above and has provided copies of such permissions and consents to IEEE.

[ ] Please check this box if you do not wish to have video/audio recordings made of your conference presentation.

See below for Retained Rights/Terms and Conditions, and Author Responsibilities.

AUTHOR RESPONSIBILITIES

The IEEE distributes its technical publications throughout the world and wants to ensure that the material submitted to its publications is properly available to the readership of those publications. Authors must ensure that their Work meets the requirements as stated in section 8.2.1 of the IEEE

159

PSPB Operations Manual, including provisions covering originality, authorship, author responsibilities and author misconduct. More information on IEEEs publishing policies may be found at http://www.ieee.org/publications_standards/publications/rights/pub_tools_policies.html. Authors are advised especially of IEEE PSPB Operations Manual section 8.2.1.B12: "It is the responsibility of the authors, not the IEEE, to determine whether disclosure of their material requires the prior consent of other parties and, if so, to obtain it." Authors are also advised of IEEE PSPB Operations Manual section 8.1.1B: "Statements and opinions given in work published by the IEEE are the expression of the authors."

RETAINED RIGHTS/TERMS AND CONDITIONS

General

1. Authors/employers retain all proprietary rights in any process, procedure, or article of manufacture described in the Work.

2. Authors/employers may reproduce or authorize others to reproduce the Work, material extracted verbatim from the Work, or derivative works for the author's personal use or for company use, provided that the source and the IEEE copyright notice are indicated, the copies are not used in any way that implies IEEE endorsement of a product or service of any employer, and the copies themselves are not offered for sale.

3. In the case of a Work performed under a U.S. Government contract or grant, the IEEE recognizes that the U.S. Government has royalty-free permission to reproduce all or portions of the Work, and to authorize others to do so, for official U.S. Government purposes only, if the contract/grant so requires.

4. Although authors are permitted to re-use all or portions of the Work in other works, this does not include granting third-party requests for reprinting, republishing, or other types of re-use.The IEEE Intellectual Property Rights office must handle all such third-party requests.

5. Authors whose work was performed under a grant from a government funding agency are free to fulfill any deposit mandates from that funding agency.

Author Online Use

6. Personal Servers. Authors and/or their employers shall have the right to post the accepted version of IEEE-copyrighted articles on their own personal servers or the servers of their institutions or employers without permission from IEEE, provided that the posted version includes a prominently displayed IEEE copyright notice and, when published, a full citation to the original IEEE publication, including a link to the article abstract in IEEE Xplore.Authors shall not post the final, published versions of their papers.

7. Classroom or Internal Training Use. An author is expressly permitted to post any portion of the accepted version of his/her own IEEE-copyrighted articles on the authors personal web site or the servers of the authors institution or company in connection with the authors teaching, training, or work responsibilities, provided that the appropriate copyright, credit, and reuse notices appear prominently with the posted material. Examples of permitted uses are lecture materials, course packs, e-reserves, conference presentations, or in-house training courses.

8. Electronic Preprints. Before submitting an article to an IEEE publication, authors frequently post their manuscripts to their own web site, their employers site, or to another server that invites constructive comment from colleagues.Upon submission of an article to IEEE, an author is required to transfer copyright in the article to IEEE, and the author must update any previously posted version of the article with a prominently displayed IEEE copyright notice. Upon publication of an article by the IEEE, the author must replace any previously posted electronic versions of the article with either (1) the full citation to the IEEE work with a Digital Object Identifier (DOI) or link to the article abstract in IEEE Xplore, or (2) the accepted version only (not the IEEE-published version), including the IEEE copyright notice and full citation, with a link to the final, published article in IEEE Xplore.

INFORMATION FOR AUTHORS

IEEE Copyright Ownership

It is the formal policy of the IEEE to own the copyrights to all copyrightable material in its technical publications and to the individual contributions contained therein, in order to protect the interests of the IEEE, its authors and their employers, and, at the same time, to facilitate the appropriate re-use of this material by others.The IEEE distributes its technical publications throughout the world and does so by various means such as hard copy, microfiche, microfilm, and electronic media.It also abstracts and may translate its publications, and articles contained therein, for inclusion in various compendiums, collective works, databases and similar publications.

Author/Employer Rights

If you are employed and prepared the Work on a subject within the scope of your employment, the copyright in the Work belongs to your employer as a work-for-hire. In that case, the IEEE assumes that when you sign this Form, you are authorized to do so by your employer and that your employer has consented to the transfer of copyright, to the representation and warranty of publication rights, and to all other terms and conditions of this Form. If such authorization and consent has not been given to you, an authorized representative of your employer should sign this Form as the Author.

<center>**GENERAL TERMS**</center>

1. The undersigned represents that he/she has the power and authority to make and execute this form.
2. The undersigned agrees to identify and hold harmless the IEEE from any damage or expense that may arise in the event of a breach of any of the warranties set forth above.
3. In the event the above work is not accepted and published by the IEEE or is withdrawn by the author(s) before acceptance by the IEEE, the foregoing grant of rights shall become null and void and all materials embodying the Work submitted to the IEEE will be destroyed.
4. For jointly authored Works, all joint authors should sign, or one of the authors should sign as authorized agent for the others.

Ghada Atteia   **13-01-2014**
Author/Authorized Agent For Joint Authors   **Date(dd-mm-yy)**

THIS FORM MUST ACCOMPANY THE SUBMISSION OF THE AUTHOR'S MANUSCRIPT.
Questions about the submission of the form or manuscript must be sent to the publication's editor.Please direct all questions about IEEE copyright policy to:
IEEE Intellectual Property Rights Office, copyrights@ieee.org, +1-732-562-3966 (telephone)

Bibliography

[1] P. Avis, "Surveillance and Canadian maritime domestic security," *Canadian Military Journal*, 2003. Available online: http://www.journal.forces.gc.ca/vo4/no1/policy-police-eng.asp [October 20, 2014].

[2] "Maritime Affairs." Internet: http://www.navyleague.ca/en/maritime-affairs/ [October 20, 2014].

[3] "Maritime security in the 21st century." Internet: http://www.steamshipmutual.com/Downloads/Articles/HudsonTridentMS.pdf [October 20, 2014].

[4] N. Tayebi, "Identification and characterization of a cost-effective combination of a system for arctic surveillance: the Northern Watch Project," MSc. Thesis, University of Ottawa, 2009.

[5] "Fisheries and oceans Canada." Internet: http://www.glf.dfo-mpo.gc.ca/Gulf/FAM/CP/VMS [October 20, 2014].

[6] "Canadian coast guard." Internet: http://www.ccg-gcc.gc.ca/eng/CCG/Maritime-Security/AIS [October 20, 2014].

[7] G.G. Lemoine, H. Greidanus, I.M. Shepherd, N. Kourti, "Development in satellite fisheries monitoring and control," in *Proc. 8th International Conference on Remote Sensing for Marine and Coastal Environments*, Halifax, Canada, 2005.

[8] H. Greidanus, "Assessing the operationality of ship detection from space, in *Proc. EURISY Symposium New Space Services for Maritime Users*, Paris, 2005.

[9] H. Greidanus, N. Kourti, "A detailed comparison between radar and optical vessel signatures," in *Proc. IEEE International Geoscience and Remote Sensing Symposium (IGARSS)'*, 2006, pp. 3267– 3270.

[10] H. Greidanus et. al, "Benchmarking operational SAR ship detection," in *Proc. IEEE International Geoscience and Remote Sensing Symposium (IGARSS)'*, 2004, pp. 4215–4218.

[11] M.J. Caruso, M. Migliaccio, J.T. Hargrove, O. Garcia-Pineda, and H.C. Graber, "Oil spills and slicks imaged by synthetic aperture radar," Oceanography, vol. 26, no. 2, pp. 113 –123, 2013.

[12] D. Crisp. "The State-of-the-Art in ship detection in Synthetic Aperture Radar imagery," Technical Report DSTO-RR-0272, DSTO Information Sciences Laboratory, Edinburg, Australia, 2004.

[13] D. Power, J. Youden, K. Lane, C. Randell and D. Flett, "Iceberg detection capabilities of RADARSAT synthetic aperture radar," *Canadian Journal of Remote Sensing*, vol. 27, no. 5, pp. 476–486, 2001.

[14] J.C. Curlander, R.N. McDonough. *Synthetic aperture radar: systems and signal processing.* Wiley-Interscience, 1991.

[15] C. Oliver, S. Quegan, *Understanding synthetic aperture radar images*, Artech House, 1997.

[16] C. Liu, A. Meek, "Likelihood ratio test polarimetric SAR ship detection application," Defence Research and Development Canada, Technical Memorandum, TM 2005-243.

[17] C. Howell, D. Power, M. Lynch, K. Dodge, P. Bobby, C. Randell, P. Vachon, G. Staples, "Dual polarization detection of ships and icebergs – recent results with ENVISAT ASAR and data simulations of Radarsat-2," in *Proc. IEEE International Geoscience and Remote Sensing Symposium (IGARSS)*', 2008, pp. 206–209.

[18] R. Touzi, "On the use of polarimetric SAR data for ship detection," in *Proc. IEEE International Geoscience and Remote Sensing Symposium (IGARSS)*, 1999, pp. 812–814.

[19] C. Liu, P.W. Vachon and G.W. Geling, "Improved ship detection with airborne polarimetric SAR data," *Canadian Journal of Remote Sensing*, vol. 31, no. 1, pp. 122-131, May 2005.

[20] F. Charbonneau, B. Brisco, R. Raney, R. McNairn, C. Liu, P. Vachon, J. Shang, R. DeAbreu, C. Champagne, A. Merzouki and T. Geldsetzer, "Compact polarimetry overview and applications assessment," *Canadian Journal of Remote Sensing*, vol. 36, no. 2, pp. 298–315, 2009.

[21] S. Angelliaume, P. Durand, J.C. Souyris, "Ship detection using X-band dual-pol SAR data," in *Proc. IEEE International Geoscience and Remote Sensing Symposium (IGARSS)*, 2011, pp. 3827-3830 .

[22] J.C. Souyris, P. Imbo, R.F. Fjortoft, S. Mingot, J.S. Lee, "Compact polarimetry based on symmetry properties of geophysical media: The $\pi/4$ mode," *IEEE Transactions on Geoscience and Remote Sensing*, vol. 43, no. 3, pp. 634–646, 2005.

[23] R.K. Raney, "Hybrid-polarity SAR architecture," *IEEE Transactions on Geoscience and Remote Sensing*, vol. 45, no. 11, pp. 3397–3404, 2007.

[24] P. Dubois-Fernandez, J.C. Souyris, S. Angelliaume, and F. Garestier, "The compact polarimetry alternative for spaceborne SAR at low frequency," *IEEE Transactions on Geoscience and Remote Sensing*, vol. 46, pp. 3208–3222, 2008.

[25] R. K. Raney, "Comments on hybrid-polarity SAR architecture," in *Proc. IEEE International Geoscience and Remote Sensing Symposium (IGARSS)*, 2007, pp. 2229–2231.

[26] G. Chin, S. Brylow, M. Foote, J. Garvin, J.Kasper, J. Keller, M. Litvak, I. Mitrofanov, D.Paige, K. Raney, M. Robinson, A. Sanin, D. Smith, H. Spence, P. Spudis, S. A. Stern, and M.T. Zuber, "Lunar Reconnaissance Orbiter overview: The instrument suite and mission," *Space Science Review*, vol. 129, pp. 391–419, 2007.

[27] J. Goswami, M.Annadurai, "Chandrayaan-1: India's first planetary science mission to the moon," *Current Science*, vol. 96, no. 4, pp. 486–490, 2009.

[28] C.R. Jackson, J.R. Apel. "Synthetic Aperture Radar marine user's manual,", 2004, available online: http://www.sarusersmanual.com/

[29] P. Vachon, J. Campbell,C. Bjerkelund, C. Dobson, M. Rey, "Ship detection by the RADARSAT SAR: Validation of detection model predictions," *Canadian Journal of Remote Sensing*, vol. 23, no.1, pp. 48–59, 1997.

[30] M. Yeremy, J. Campbell, K. Mattar, T. Potter, "Ocean surveillance with polarimetric SAR," *Canadian Journal of Remote Sensing*, vol. 27, no.4, pp. 328–344.

[31] R.K. Hawkins, K.P. Murnaghan, T. Tennant, M. Yeremy, and M. Rey, "Ship detection using airborne polarimetric SAR," in CEOS SAR Workshop, 2001, Tokyo, Japan.

[32] R. Touzi, F. Charbonneau, R.K. Hawkins, K. Kevin Murnaghan, X. Kavoun, "Ship-sea contrast optimisation when using polarimetric SAR," in *Proc. IEEE International Geoscience and Remote Sensing Symposium (IGARSS)*, 2001, pp. 426–428.

[33] R. Touzi, F.J. Charbonneau, R.K. Hawkins, P.W. Vachon, "Ship detection and characterization using polarimetric SAR," *Canadian Journal of Remote Sensing*, vol. 30, no. 3, 2004, pp. 552–559.

[34] J. Shin,Y. Oh, K. Lee, "Polarimetric SAR image decomposition using the degree of polarization and the co-polarized phase difference," in *Proc. of 3rd International Asia-Pacific Conference on Synthetic Aperture Radar (APSAR)*, 2011.

[35] F. Askari, B. Zerr, "Automatic approach to ship detection in spaceborne synthetic aperture radar imagery: An assessment of ship detection capability using RADARSAT," Technical Report SACLANTCEN-SR-338, SACLANT Undersea Research Centre, La Spezia (Italy), 2000.

[36] J.S. Lee and I. Jurkevich, "Coastline detection and tracing in SAR images," *IEEE Transactions on Geoscience and Remote Sensing*, vol. 28, pp. 662-668, 1990.

[37] D.C. Mason, and I.J. Davenport, "Accurate and efficient determination of the shoreline in ERS-1 SAR Images," *IEEE Transactions on Geoscience and Remote Sensing*, vol.34, pp. 1243-1253, 1996.

[38] R. Touzi, A. Lopes,and P. Bousquet, "A statistical and geometrical edge detector for SAR images," *IEEE Transactions on Geoscience and Remote Sensing*, vol. 26, pp. 764-773, 1988.

[39] T.W. Ryan, P.J. Sementilli, P.J. Yuen, and B. R. Hunt, "Extraction of shoreline features by neural nets and image processing," *Photogrammetric Engineering and Remote Sensing*, vol. 57, pp. 947-955, 1991.

[40] H. Liu, K.C. Jezek, "Automated extraction of coastline from satellite imagery by integrating Canny edge detection and locally adaptive thresholding methods," *International Journal of remote sensing*, vol. 25, no. 5, pp. 937-958,Mar. 2004.

[41] I. Lin, L. Kwoh, Y. Lin, and V. Khoo, "Ship and ship wake detection in the ERS SAR imagery using computer-based algorithm,"in *Proc. IEEE International Geoscience and Remote Sensing Symposium (IGARSS)*, 1997, pp. 151–153.

[42] K. Lee, and T. Bretschneider, "Improved ship detection using dual-frequency polarimetric synthetic aperture radar data," in *Proc. International Geoscience and Remote Sensing Symposium (IGARSS)*, 2011, pp. 2274–2277.

[43] L. Xiaowei, C. Jinsong, Z. Minhui, "A ship detection method for dual polarization SAR data based on whitening filtering," in *Proc. IEEE International Geoscience and Remote Sensing Symposium (IGARSS)*, 2007, pp. 4171–4174.

[44] K. El-Darymli, P. McGuire, D. Power, C. Moloney, "Target detection in synthetic aperture radar imagery: a state-of-the-art survey," *Journal of Applied Remote Sensing*, vol. 7, no. 1, Mar. 2013.

[45] M. Sciotti, P. Lombardo, "Ship detection in SAR images: a segmentation-based approach," in *Proc. IEEE Radar Conference*, 2001, pp. 81–86.

[46] P. Lombardo, M. Sciotti, "Segmentation-based technique for ship detection in SAR images," in *Proc. IEE Radar, Sonar and Navigation*, 2001, pp. 147–159.

[47] L.M. Novak, S.D. Halversen, G. Owirka, M. Hiett, "Effects of polarization and resolution on SAR ATR," *IEEE Transactions on Aerospace and Electronic Systems*, vol. 33 , no. 1, pp. 102–116, 1997.

[48] M. Sciotti, D. Pastina, P. Lombardo, "Exploiting the polarimetric information for the detection of ship targets in non-homogeneous SAR images," in *Proc. IEEE International Geoscience and Remote Sensing Symposium (IGARSS)*, 2002, pp. 1911–1913.

[49] M. Sciotti, D. Pastina, and P. Lombardo, "Polarimetric detectors of extended targets for ship detection in SAR images," in *Proc. International Geoscience and Remote Sensing Symposium (IGARSS)*, 2001, pp. 3132–3134.

[50] R. Cook, I. McConnell, D. Stewart, C.J. Oliver, "Segmentation and simulated annealing," in *Proc. European Conference on SAR image analysis and modeling*, Taormina, Italy, 1996.

[51] L.M. Novak, and M.C. Burl, "Optimal speckle reduction in polarimetric SAR imagery," *IEEE Transactions on Aerospace and Electronic Systems*, vol. 26, No. 2, 293–305, 1990.

[52] M. Brizi, P. Lombardo, and D. Pastina, "Exploiting the shadow information to increase the target detection performance in SAR images," in *Proc. IEEE International Conference on Radar Systems, RADAR99*, 1999.

[53] N. Kourti, I. Shepherd, G. Schwartz, and P. Pavlakis, "Integrating spaceborne SAR imagery into operational systems for fisheries monitoring," *Canadian Journal of Remote Sensing*, vol. 27 no. 4, pp.291-305, 2001.

[54] P. Soille, *Morphological Image Analysis: Principles and Applications*, Springer Berlin Heidelberg, 2003.

[55] J. Qingshan, S. Wang, D. Ziou, A. El Zaart, M. Rey, G.B. Benie, M. Henschel, "Ship detection in RADARSAT SAR imagery," in *IEEE International Conference on Systems, Man, and Cybernetics*, 1998, 4562–4566.

[56] "Risat-1." Internet: http://www.isro.org/satellites/risat-1.aspx. [March 1, 2013].

[57] M. Nord, T. Ainsworth, J.-S. Lee, N. Stacy, "Comparison of compact polarimetric Synthetic Aperture Radar modes," *IEEE Transactions on Geoscience and Remote Sensing*, vol. 47, no. 1, pp. 174–188, 2009.

[58] K.R. Raney, "Dual-polarized SAR and stokes parameters," *IEEE Geoscience and Remote Sensing Letters*, vol. 3, no.3, pp. 317–319, 2006.

[59] T. Ainsworth, J. Kelly, J.S. Lee, "Classification comparisons between dual-pol, compact polarimetric and quad-pol SAR imagery," *ISPRS Journal of Phototgrammetry and Remote Sensing*, vol. 64, pp. 464–471, 2009.

[60] M.-L. Truong-Loi, A. Freeman, P. Dubois-Fernandez, E. Pottier, " Estimation of soil moisture and Faraday rotation from bare surfaces using compact polarimetry," *IEEE Transactions on Geoscience and Remote Sensing*, vol. 47, no. 11, pp. 3608–3615, 2009.

[61] S. Angelliaume, P. Dubois-Fernandez, J.C. Souyris, "Compact POLINSAR for vegetation characterisation," in *Proc. IEEE International Geoscience and Remote Sensing Symposium (IGARSS)*, 2007, pp. 1136–1138.

[62] C. Lardeux, P.-L. Frison, C. Tison, J.C. Souyris, B. Stoll, B. Fruneau, J.P. Rudant, "Classification of tropical vegetation using multifrequency partial SAR polarimetry," *IEEE Geoscience and Remote Sensing Letters*, vol. 8, no. 1, 133–137.

[63] S. V. Nghiem, S. H. Yueh, R. Kwok, and F. K. Li, "Symmetry properties in polarimetric remote sensing," *Radio Science*, vol. 27, no. 5, pp. 693–711, 1992.

[64] S. Yueh, S. Nghiem, and R. Kwok, "Comparison of a polarimetric scattering and emission model with ocean backscatter and brightness measurements," in *Proc. IEEE International Geoscience and Remote Sensing Symposium (IGARSS)*, 1994, vol. 1, pp. 258–260.

[65] M. J. Collins, M. Denbina, G. Atteia, "On the reconstruction of quad-Pol SAR data from compact polarimetry data for ocean target detection," *IEEE Transactions on Geoscience and Remote Sensing*, vol. 51, no. 1, pp. 591–600, 2013.

[66] J. Yin, J. Yang, X. Zhang, "On the ship detection performance with compact polarimetry," in *Proc. IEEE Radar Conference*, 2011, pp. 675–680.

[67] K. R Raney, P. Spudis, B. Bussey, J. Crusan, J. Jensen, W. Marinelli, P. McKerracher, C. Neish, M. Palsetia, R. Schulze, H. Sequeira, H. Winters, "The lunar mini-RF radars: Hybrid polarimetric architecture and initial results," in *Proc. IEEE International Geoscience and Remote Sensing Symposium (IGARSS)*, vol.99, no. 5, 2010, pp. 808–823.

[68] R. K. Raney, Joshua T. S. Cahill, G. W. Patterson, D. Benjamin and J. Bussey, " The m-chi decomposition of hybrid dual-polarimetric radar data with application to lunar craters," *Journal of Geophysical Research: Planets*, vol. 117, no. E12, Dec. 2012.

[69] H. Li, W. Perrie, Y. He, S. Lehner, and S. Brusch, "Target detection on the ocean with the relative phase of compact polarimetry SAR," *IEEE Transactions on Geoscience and Remote Sensing*, pp. 1–7, 2012.

[70] R. Shirvany, M. Chabert, J.Y. Tourneret, "Ship and oil-spill detection using the degree of polarization in linear and hybrid/compact dual-pol SAR," *IEEE Journal of Selected Topics in Applied Earth Observations and Remote Sensing*, vol. 5, no. 3, pp. 885 - 892, 2012.

[71] C. Liu, P.W. Vachon, R.A. English, N. Sandirasegaram, "Ship detection using RADARSAT-2 Fine Quad mode and simulated compact polarimetry data," Defence Research and Development Canada, Technical Memorandum, 2009.

[72] C. Zhuo, "A new type of automatic ship detection method,"in 5th *International Conference on Wireless Communications, Networking and Mobile Computing*, 2009 , pp. 1–4.

[73] X.W. Xing, Z.L. Chen, H.X. Zou, S.L. Zhou, "Fast algorithm based on two-stage CFAR for detecting ships in SAR images," in 2nd *Asian-Pacific Conference on Synthetic Aperture Radar*, 2009, pp. 506–509.

[74] L. Scharf, *Statistical Signal Processing: Detection, Estimation, and Time Series Analysis*, Prentice Hall, 1990.

[75] C. Wackerman, K. Friedman, W. Pichel, P. Clemente-Colon, X. Li, "Automatic detection of ships in RADARSAT-1 SAR imagery," *Canadian Journal of Remote Sensing*, vol. 27, no. 5, pp. 568-577, 2001.

[76] G.J. McLachlan and D. Peel, *Finite Mixture Models*, Wiley Series in Probability and Statistics, 2000.

[77] H. Zhaoying, C. Jinsong, "A review of ship detection algorithms in polarimetric SAR images," in *Proc. 7th International Conference on Signal Processing (ICSP)*, 2004, vol. 3, pp. 2155–2158.

[78] X. Su, G. Yang and H. Sang, "Ship Detection in Polarimetric SAR Based on Support Vector Machine," *Research Journal of Applied Sciences, Engineering and Technology*, vol. 4, no. 18, pp. 3448–3454, 2012.

[79] P. Vachon, J. Wolfe, "C-band cross-polarization wind speed retrieval," *IEEE Geoscience and Remote Sensing Letters*, vol. 8, no. 3, pp. 456–459, 2011.

[80] Y. Crevier and D. Flett, "The Radarsat Constellation Mission: overview and capabilities for marine monitoring," in 3rd *international workshop on advances in SAR oceanography from Envisat, ERS and ESA third party, SEASAR*, Italy, 2010.

[81] G. E. Atteia and M. J. Collins, "On the use of compact polarimetric SAR for ship detection," *ISPRS Journal of Photogrammetry and Remote Sensing*, vol. 80, pp. 1 - 9, June 2013.

[82] G. E. Atteia and M. J. Collins, "Ship detection performance using simulated dual-polarization Radarsat Constellation Mission data," *International Journal of Remote Sensing and Remote Sensing Letters*, submitted.

[83] G. E. Atteia and M. J. Collins, "Ship detection Performance assessment for simulated RCM SAR data," in *Proc. of the IEEE International Geoscience and Remote Sensing Symposium (IGARSS)*, July 2014.

[84] P. Vachon, J. Campbell, C. Bjerkelund, F. Dobson, M. Rey, "Ship detection by the RADARSAT SAR: validation of detection model predictions," *Canadian Journal of Remote Sensing*, vol. 23, no. 1, pp. 48-51, 1979.

[85] K. Friedman, C. Wackerman, F. Funk, W. Pichel, P. Clemente-Colon, X. Li, "Validation of a CFAR vessel detection algorithm using known vessel locations," in *Proc. IEEE the International Geoscience and Remote Sensing Symposium (IGARSS)*, pp. 1804–1806, 2001.

[86] G. Margarit, A. Tabasco, "Ship classification in single-pol SAR images based on fuzzy logic," *IEEE Transactions on Geoscience and Remote Sensing*, vol. 49, no. 8, pp. 3129–3138, 2011.

[87] G. Margarit, J. Mallorqui, J. Fortuny-Guasch, C. Lopez-Martinez, "Exploitation of ship scattering in polarimetric SAR for an improved classification under high clutter conditions," *IEEE Transactions on Geoscience and Remote Sensing*, vol. 47,no. 4, pp. 1224–1235, 2009.

[88] G. G. Stokes , "On the composition and resolution of streams of polarized light from different sources," in *Proc. Cambridge Philosophical Society : Mathematical and Physical Sciences*, vol. 9, pp.399 -416, 1852.

[89] K. Raney, "Hybrid-Polarity SAR Architecture," *IEEE Transactions on Geoscience and Remote Sensing*, vol. 45,no. 11, pp. 3397– 3404, 2007.

[90] R. Barakat, " Statistics of the Stokes parameters," *Journal of the Optical Society of America A: Optics and Image Science*, vol. 4, no. 7, pp. 256–1263, 1987.

[91] R. Touzi, A. and Lopes, " Statistics of the Stokes parameters and of the complex coherence parameters in one-look and multilook speckle fields," *IEEE Transactions on Geoscience and Remote Sensing*, vol. 34, no. 2, pp. 519–531, 1996.

[92] R. Touzi, W. M. Boerner, J. S.Lee, E. Lueneburg, " A review of polarimetry in the context of synthetic aperture radar: concepts and information extraction," *Canadian Journal of Remote Sensing*, vol. 30, no. 3, pp. 380–407, 2004.

[93] M. Born and E. Wolf, *Principles of Optics*, Cambridge University Press, 1999.

[94] E. Wolf, "Optics in terms of observable quantities," *II Nuovo Cimento Series 10*, vol. 12, no. 6, pp. 884-888, 1954.

[95] S.R. Cloude, E. Pottier, "A review of target decomposition theorems in radar polarimetry," *IEEE Transactions on Geoscience and Remote Sensing*, vol.34, no. 2, pp. 498–518, Mar. 1996.

[96] K. Raney, " M-chi Decomposition of Imperfect Hybrid Dual-Polarimetric Radar Data," Presented in *6th, Science and Applications of SAR Polarimetry and Polarimetric Interferometry (PollnSAR)* , 2013, Frascati, Italy. Available online: https://earth.esa.int/documents/10174/408563/2_Raney_Methods.pdf/a22c7b81-55f8-4de8-9dff-c9654e8ae0cb?version=1.0 [October 24, 2014].

[97] J. Cahill, B. Bussey, G. Patterson, "Global MINI-RF S-Band CPR and m-chi Decomposition Observations of the moon," in *43rd Lunar and Planetary Science Conference*, 2012.

[98] J. Cahill, B. Bussey, G. Patterson, "Global MINI-RF S-Band CPR and m-chi Decomposition Observations of the moon," in *43rd Lunar and Planetary Science Conference*, 2012.

[99] J. Lee, E. Pottier, *Polarimetric Radar Imaging: From Basics to Applications*, CRC Press, 2009.

[100] G. Gao, " Statistical Modeling of SAR Images: A Survey," *Sensors*, vol. 10, pp. 775–795, 2010.

[101] Y. Jin, N. Zhang, " Statistics of four Stokes parameters in multi-look polarimetric synthetic aperture radar(SAR) imagery," *Canadian Journal of Remote Sensing*, vol. 28, no. 4, pp. 610–619, 2002.

[102] J.S. Lee, K.W. Hoppel, S.A. Mango and A.R. Miller, " Intensity and phase statistics of multilook polarimetric and interferometric SAR imagery," *IEEE Transactions on Geoscience and Remote Sensing*, vol. 32, no. 5, pp. 1017–1027, 1994.

[103] D.R. Sheen and L.P. Johnston, " Statistical and spatial properties of forest clutter measured with polarimetric Synthetic Aperture Radar (SAR)," *IEEE Transactions on Geoscience and Remote Sensing*, vol. 30, no. 3, pp. 578–588, 1992.

[104] A.P. Dempster, N. M. Laird, and D. B. Rubin, "Maximum likelihood from incomplete data via the EM algorithm," *Journal of the Royal Statistical Society*, vol. 39n, pp. 1-38, 1977.

[105] G.J. McLachlan and T.Krishnan, *The EM Algorithm and Extensions*, Wiley Series in Probability and Statistics, 2008.

[106] H. Akaike, "A new look at the statistical model identification," *IEEE Transactions on Automatic Control*, vol. 19, no. 6, pp. 716–723, 1974.

[107] Gi. Schwarz, "Estimating the dimension of a model," *Annals of Statistics*, vol. 6, no. 2, pp. 461–464, 1978.

[108] K. Nylund, T. Asparouhov, B.Muthan, "Deciding on the number of classes in latent class analysis and growth mixture modeling," *Structural Equation Modelling*, vol. 14, no. 4, pp.535–569, 2007.

[109] J. Canny, " A Computational Approach To Edge Detection," *IEEE Transactions on Pattern Analysis and Machine Intelligence*, vol. 8, no. 6, pp. 679–698, 1986.

[110] J. S. Lee, "Digital image smoothing and the sigma filter," *Computer Vision, Graphics and Image Processing*, vol. 24, no. 2, pp. 255–269, 1983.

[111] A. Leon-Garcia, *Probability, Statistics, and Random Processes For Electrical Engineering*, Prentice Hall, 2007.

[112] I. Elizavetin, "Radiometric artifacts on SAR images," in *International Scientific and technical conference*, Italy, 2010.